Dissertation

submitted to the
Combined Faculties for the Natural Science and for Mathematics
of the Ruperto-Carola University of Heidelberg, Germany
for the degree of
Doctor of Natural Sciences

Put forward by
Vanessa Véronique Simon

B.Sc., Technische Universität Darmstadt, 2007
M.Sc., Technische Universität Darmstadt, 2009
Born in: Frankfurt a. M., Germany
Oral examination: 07. 11. 2012

Penning-trap mass spectrometry of radioactive, highly charged ions with TITAN:

Measurements of neutron-rich Rb and Sr nuclides for nuclear astrophysics and the development of a novel Penning trap for cooling highly charged ions

Referees: Prof. Dr. Klaus Blaum
P.D. Dr. José R. Crespo López-Urrutia

Abstract:
High-precision atomic mass measurements are vital for the description of nuclear structure, investigations of nuclear astrophysical processes, and tests of fundamental symmetries. The neutron-rich $A \approx 100$ region presents challenges for modeling the astrophysical r-process because of sudden nuclear shape transitions. This thesis reports on high-precision masses of short-lived neutron-rich ^{94,97,98}Rb and $^{94,97-99}$Sr isotopes using the TITAN Penning-trap mass spectrometer at TRIUMF. The isotopes were charge-bred to $q = 15+$; uncertainties of less than 4 keV were achieved. Results deviate by up to 11σ compared to earlier measurements and extend the region of nuclear deformation observed in the $A \approx 100$ region. A parameterized r-process model network calculation shows that mass uncertainties for the elemental abundances in this region are now negligible.
Although beneficial for the measurement precision, the charge breeding process leads to an increased energy spread of the ions on the order of tens of eV/q. To eliminate this drawback, a Cooler Penning Trap (CPET) has been developed as part of this thesis. The novel multi-electrode trap structure of CPET forms nested potentials to cool HCI sympathetically using either electrons or protons to increase the overall efficiency and precision of the mass measurement. The status of the off-line setup and initial commissioning experiments are presented.

Zusammenfassung:
Die Messung atomarer Massen mit hoher Genauigkeit spielt eine große Rolle bei der Beschreibung der Struktur von Kernen, Untersuchungen astrophysikalischer Prozesse und Tests fundamentaler Symmetrien. Die Modellierung astrophysikalischer Prozesse, die im r-Prozess berücksichtigt werden müssen, ist in der neutronen-reichen Massenregion um $A \approx 100$ aufgrund abrupt auftretender Änderungen der Kerndeformationen äußerst schwierig. Für diese Arbeit wurden hochpräzise Massenmessungen von kurzlebigen, neutronen-reichen ^{94,97,98}Rb- und $^{94,97-99}$Sr-Isotopen durchgeführt, die am TITAN Penningfallen-Massenspektrometer am TRIUMF stattfanden. Die Nuklide wurden zu einem Ladungszustand $q = 15+$ gebrütet; Messunsicherheiten von besser als 4 keV wurden erreicht. Die Resultate unterscheiden sich bis zu 11σ von Literaturwerten und der Bereich bekannter Kerndeformierungen in der $A \approx 100$ Massenregion wurde erweitert. Eine parametrisierte r-Prozess Modelrechnung wurde durchgeführt und zeigt, dass Unsicherheiten der Massenmessungen nun keinen Einfluss mehr auf die modellierten Elementhäufigkeiten dieser Region haben.
Obwohl das Ladungsbrüten die Präzision der Massenmessung erhöht, führt der Prozess auch zu einer größeren Energiebreite der Ionen, in der Größenordnung von Dutzenden von eV/q. Um diesen Nachteil zu beseitigen, wurde im Rahmen dieser Dissertation eine Kühler-Penningfalle (CPET) für TITAN entwickelt. Die neuartige multi-Elektroden Fallenstruktur der CPET ermöglicht sympathetisches Kühlen hochgeladener Ionen mittels Elektronen oder Protonen in eingebetteten Potentialen. Eine Verbesserung der Gesamteffizienz und Präzision der Massenmessung wird erwartet. Der Status des Offline-Experimentieraufbaus und erste Testexperimente werden gezeigt.

Contents

List of Figures

List of Tables

Chapter 1

Introduction and Motivation

A fundamental property of the atom is its mass, which provides insight into all inner workings of the complex fundamental interactions using a simple quantity. The atomic mass is not the evident sum of its constituent masses, but rather it represents the sum of all components and the forces acting between them. The difference between the simple sum and the real mass, known as the binding energy, yields important knowledge of the structure of the atom. Consequently, a broad variety of studies, including e.g. nuclear structure and astrophysical studies [1, 2], are impacted by providing reliable experimental atomic mass data.

Cartography of the mass surface, for example, allows many studies of nuclear structure. The Segré chart (as presented in a three-dimensional rendering in Figure 1.1) shows all known atoms (or isotopes) according to their proton and neutron number. Along the center line at about a 45°-angle lies the so-called valley of (β-) stability. The β-stability is a consequence of the well-established mass parabola, where all isobars (atoms with the same number of nucleons but different combination of neutrons and protons) are shown, and the ones with the lowest mass (hence highest binding) are at the vertex, the mountain summits in Figure 1.1. At the edge of the Segré chart, the shoreline, the limits of nuclear existence are defined where the binding energy equals zero, also called the proton and neutron drip-lines [3]. Their exact location is often not known empirically, and new nuclides are discovered every year [3]. Between the drip-lines, the mass surface generally varies smoothly; kinks and changes in slope may indicate various abnormal nuclear behaviors such as shell closures or deformation [4]. The neutron-rich region around $A \approx 100$ illustrates such an aberration. Not only are new shell closures expected, but also shape transitions have been observed [5–15]. In this thesis, these trends will be explored in the rubidium and strontium isotopes by investigating the two-neutron separation energies, the mass difference be-

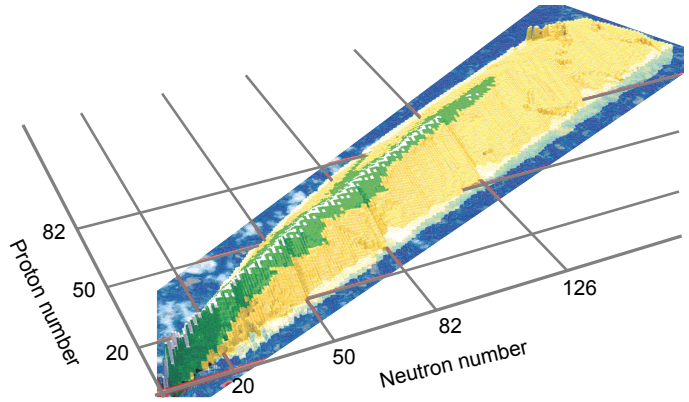

Figure 1.1: Three-dimensional rendering of the Segré chart illustrating the mass parabola as an island of nuclides. The island consists of mountain summits (the stable nuclides), green areas below the ridge (the measured radioactive nuclides), and the yellow regions (the predicted but unobserved radioactive nuclides) surrounded by the ocean of unstable combinations of protons and neutrons. Figure from [16].

tween neighbors separated by two neutrons.

Another discipline in which masses play a crucial role is nuclear astrophysics. Masses along with other nuclear properties such as half-lives and reaction rates are critical for calculations of solar elemental abundances, which are the result of several different production mechanisms including the slow neutron capture or s-process and the rapid neutron capture or r-process. These two processes are believed to be equally responsible for the nucleosynthesis of elements heavier than iron [17]. Unfortunately, despite its importance, the r-process is poorly understood because, in part, of a lack of relevant experimental data. Its calculations rely heavily on mass models, which are anchored on known masses but diverge significantly for unknown masses [2]. As a consequence, the predicted solar elemental abundance is heavily model-dependent with differences between mass models as shown in Figure 1.2. A high-entropy wind r-process calculation is used while varying the mass input using several mass models. The various mass models rely on different physics extrapolating to unknown masses leading to deviations in the calculated elemental abundance. Mass measurements along the predicted r-process path, such as those in this thesis near $A \approx 100$, provide invaluable input. Following a detailed discussion in Chapter 2 of the relevant nuclear structure and astrophysics, the measurement technique, the experimental design, and the results will be presented in Chapters 3, 4, and 5 respectively.

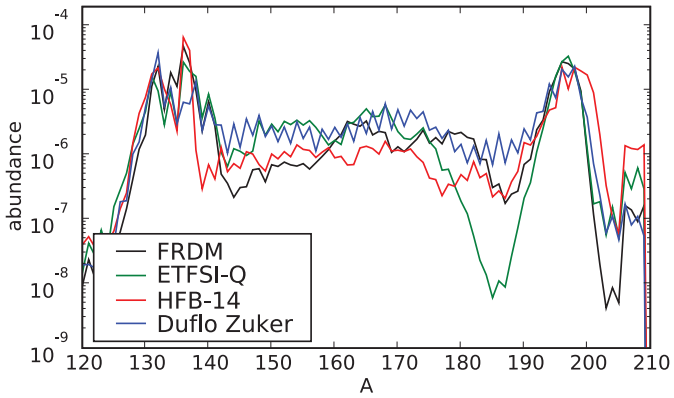

Figure 1.2: Final elemental abundances obtained from different mass models using a high-entropy wind r-process model [18, 19]. Figure from [18]. The sensitivity on the different mass models for a r-process model calculation is shown.

The mass measurements presented are unique from a technical aspect as well; they were performed in the highest charge state ($q = 15+$) ever reached thus far in Penning-trap mass spectrometry of rare isotope beams. The capability to charge breed rare isotope beams for such measurements is unique to TRIUMF's Ion Trap for Atomic and Nuclear science (TITAN) [20], in Canada, where it is performed with an electron beam ion trap (EBIT). The advantage of coupling the two techniques is a boost in precision since it scales linearly with the charge state of the ion, which is particularly beneficial for nuclides with short half-lives. The use of highly charged ions (HCI) also poses certain challenges. Transmission and decay losses can be incurred during the charge-breeding process. Moreover, charge breeding in the EBIT introduces an energy spread on the order of tens of eV/q, which negatively impacts the systematic uncertainty of the mass measurement.

The attainable precision of the mass measurement depends heavily on the possibility of ion cooling and a reduction of the large energy spread. Consequently, the Cooler Penning Trap (CPET) was proposed, and its design and realization are described in the second half of this thesis. Extensive simulations of and for CPET were completed, leading to its design, and its construction was carried out as part of this work. Of the several cooling techniques explored, sympathetic cooling with electrons and protons was chosen. Electron cooling is an established technique but to date has not been used to cool HCI in a Penning trap; it is advantageous in that the electrons self-cool in the presence of a magnetic field and facilitate a fast cooling process. On

the other hand, proton cooling has the advantage of avoiding recombinations with the positively charged radioactive beam, but it has never been tested as a coolant. The conceptual design as well as the technical implementation and environmental requirements in terms of vacuum and magnetic field of both cooling schemes are presented in Chapter 6.

In order to explore CPET, to establish a cooling technique, and to study cooling cycles, CPET has been initially mounted off-line with its own setup adjacent to the TITAN setup. The off-line setup that has been designed and constructed contains beamline sections for optics and diagnostics needed for studying electron and ion injection and extraction as well as the two cooling processes for HCI. Details of the overall off-line setup, commissioning experiments, and the plans for the transition to the on-line installation are discussed in Chapter 7, including first tests investigating electron injection and extraction.

CPET will strengthen the HCI mass-measurement program at TITAN and help to achieve the maximum gain in precision of up to a factor of the charge state of the radionuclide. This successful demonstration and on-line commissioning of CPET in 2013 will facilitates a larger mapping of nuclides for astrophysical processes and nuclear structure in shorter time.

Chapter 2

Theory – Nuclear Physics

The atomic mass of the nucleus, and from it derived its binding energy, is of great importance not only for various aspects in nuclear physics, but also for other branches of physics, notably weak interaction studies and astrophysics.

This chapter details the general motivation of this thesis, and it presents an overview of the topics in nuclear structure and nuclear astrophysics relevant to it.

2.1 Nuclear Structure

Atomic nuclei are quantum systems with a finite number of strongly interacting fermions of two kinds – protons and neutrons. Much of the present-day knowledge of the structure of the atomic nucleus is based on the properties of nuclei close to the line of β-stability where the proton-to-neutron ratio is close to that of stable nuclei. However, extrapolating these properties to the region far from stability is unsatisfactory, as basic knowledge attained for well-known nuclei does not transfer to so-called exotic or radioactive nuclei.

The existence of a nucleus is related to the nuclear binding energy B of the specific system of protons and neutrons. It is a measure of how much energy has been gained to form the nucleus from its bare constituents through all acting forces. The binding energy is defined as the difference in mass energy between a nucleus $\left({}^{A}_{Z}X_{N}\right)$ and its constituent particles, where A is the mass number, equal to the sum of the neutron number N and proton number Z:

$$B = \left[Z \cdot m_p + N \cdot m_n - m({}^{A}X)\right] \cdot c^2, \tag{2.1}$$

where m_p is the proton mass, m_n is the neutron mass, and c is the speed of light with $c^2 = 931.50$ MeV/u. The odd-even staggering of binding energies has been observed in several finite many-fermion systems such as nuclei [21].

It manifests itself in the fact that the binding energy of a system with an odd particle number is lower than the arithmetic mean of the energies of the two neighboring even-particle-number systems (pairing effect).

In addition to the nuclear binding energy, one can also consider particle and cluster binding energies, of which the neutron and proton binding energies are the most important for delineating the limits of nuclear existence [3]. The neutron (proton) binding energy S_n (S_p) (also called separation energy) is the amount of energy needed to remove the valence neutron (proton) from the nucleus:

$$S_n({}^{A}_{Z}X_N) = \left[-m\left({}^{A}_{Z}X_N\right) + m\left({}^{A-1}_{Z}X_{N-1}\right) + m_n\right] \cdot c^2, \tag{2.2}$$

$$S_p({}^{A}_{Z}X_N) = \left[-m\left({}^{A}_{Z}X_N\right) + m\left({}^{A-1}_{Z-1}X_N\right) + m({}^{1}H)\right] \cdot c^2. \tag{2.3}$$

The chart of nuclides (also called the Segré plot), in Figure 2.1, shows the distribution of the stable and known radioactive nuclides on a grid of proton number Z versus neutron number N. The different decay types are indicated in color: β^--decay (blue), β^+-decay (red), α-decay (yellow), and fission (green). A stable nucleus is one for which the time scale of the possible decay through the strong or weak interaction is of the order of the time scale of the universe ($13.7 \cdot 10^9$ years [22]). The area on the chart of nuclides where the stable nuclides accumulate is the so-called valley of stability. All radioactive nuclides decay back to the stable nuclides, thus establishing a region of accumulation. Nuclides of the same element, hence with the same proton number Z, are called isotopes. Nuclides of the same neutron number N are calles isotones, and nuclides of the same mass number A isobars.

Also used in the nuclear physics community is the mass excess ME, the difference between the nuclear mass and the mass number A and will be used in Chapter 5 to express the experimental mass values:

$$ME = \left[m\left({}^{A}X\right) - A\right] c^2. \tag{2.4}$$

Experimental data, such as masses, half-lives, and level densities, are not yet measured in all regions of the nuclide chart. Thus nuclear models are very important for providing input data, especially for nucleosynthesis scenarios which occur far from the valley of stability. Theoretical descriptions have seen a strong development in the last few decades driven by the increase in computational power and, of course, by both the increasing amount and precision of available experimental data.

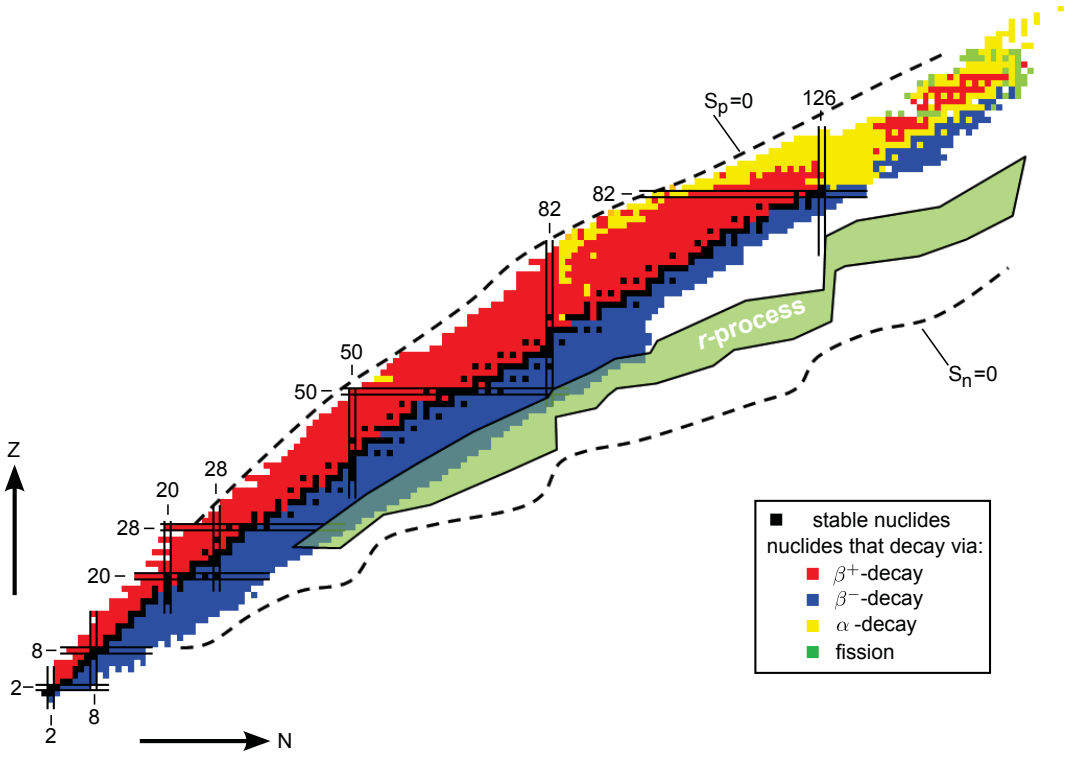

Figure 2.1: Chart of nuclides with stable (black) and radioactive nuclides (color). The proton and neutron shell gaps with their magic numbers are indicated by horizontal and vertical black lines. Dashed black lines represent the predicted proton and neutron drip-lines [23] where $S_p = 0$ and $S_n = 0$, respectively. The green shaded area highlights the region of possible r-process paths [17] (see Section 2.2).

2.1.1 Nuclear structure models

A simple macroscopic description of the nuclear binding energy, known as the Liquid Drop Model (LDM), was suggested in the 1930s by von Weizsäcker and Bethe [24, 25]. The Liquid Drop Model incorporates a volume term $\propto A$, a surface term $\propto -A^{2/3}$ and a Coulomb term $\propto -Z(Z-1)A^{-1/3}$. There are additional contributions from a symmetry term $\propto A/I^2$ and a surface symmetry term $\propto A^{2/3}I^2$, with the charge symmetry parameter $I = (N-Z)/A$. This leads to an improved Bethe-Weizsäcker mass formula [26]:

$$B = a_{\mathrm{vol}}A - a_{\mathrm{sf}}A^{2/3} + \frac{3e^2}{5r_0}Z^2A^{-1/3} + \left(a_{\mathrm{sym}}A + a_{\mathrm{ss}}A^{2/3}\right)I^2, \tag{2.5}$$

where the nuclear radius of each nuclide is given by $r \approx r_0A^{1/3}$. Derived empirically, typical values for the parameters are $a_{\mathrm{vol}} = 15.73$ MeV, $a_{\mathrm{sf}} = 26.46$ MeV, $r_o = 1.2185$ fm, $a_{\mathrm{sym}} = 17.77$ MeV, and $a_{\mathrm{ss}} = 17.70$ MeV [2, 27]. With these values the Weizsäcker-Bethe mass formula has a root mean square (rms) error

$$\sigma_{\mathrm{rms}} = \left[\frac{1}{i}\sum_{j=1}^{i}\left(m_j^{\mathrm{exp}} - m_j^{\mathrm{theo}}\right)^2\right]^{1/2} \tag{2.6}$$

of about 2.94 MeV for the $i = 2034$ existing experimental mass values (with $N, Z \geq 8$) as published in the Atomic-Mass Evaluation 2003 [28]. This is a remarkable result for a fit to more than 2000 data points using only five parameters. Nevertheless, the differences between the experimental and the theoretical predicted binding energies as a function of the neutron N and proton number Z reveal a striking pattern that can be seen in Figure 2.2. It shows the difference between the predicted mass values by the LDM and the experimental values as a function of the neutron number N. A similar effect is observed for the proton number Z. Some nuclides outside of the valley of stability are particularly stable for certain values of N and Z, which deviates significantly from the LDM. These so-called magic numbers (2, 8, 20, 28, 50, 82, 126, etc.) inspired the nuclear Shell Model [29], which is adopted from the atomic shell model. Nuclides with a magic number of either protons or neutrons are referred to as magic, and nuclides which are magic for both protons and neutrons are called doubly-magic. A Shell Model schematic is displayed in Figure 2.3. The represented shell closures correspond remarkably well to the observed magic numbers.

The effect of shells can also be seen in the elemental abundance as discussed in Section 2.2. Magic numbers also appear as a discontinuity in the two-nucleon separation energies, defined as the difference in energy for iso-

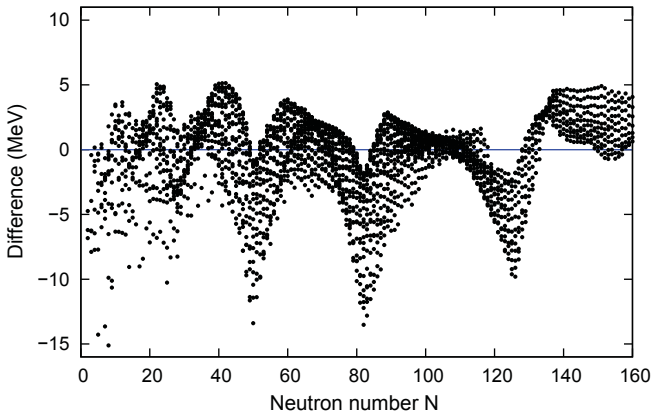

Figure 2.2: Difference between the predicted mass values by the Liquid Drop Model and the experimental mass values which is strongly dependent on the neutron number N. The largest deviations are present at the magic numbers 2, 8, 20, 28, 50, 82, 126.

topes separated by two neutrons or protons:

$$S_{2n}\left({}^{A}_{Z}X_{N}\right) = B\left({}^{A}_{Z}X_{N}\right) - B\left({}^{A-2}_{Z}X_{N-2}\right) \quad \text{for neutrons} \tag{2.7}$$

$$S_{2p}\left({}^{A}_{Z}X_{N}\right) = B\left({}^{A}_{Z}X_{N}\right) - B\left({}^{A-2}_{Z-2}X_{N}\right) \quad \text{for protons.} \tag{2.8}$$

The general trend for S_{2n} is to decrease smoothly while the neutron number N increases for a fixed Z. However, a sudden drop of the S_{2n} values indicates a shell closure since it requires less energy to remove a pair of neutrons outside of the closed shell. The behavior of the two-neutron separation energy is illustrated in Figure 2.4 with the S_{2n} values of all elements between selenium ($Z = 34$) and tin ($Z = 50$) with neutron number $N = 40 - 65$. The sudden drop at $N = 50$ is a signature of shell closure at this magic number.

In addition to shell closures, other nuclear structure features can also be seen in the S_{2n} from abrupt changes. For example, Figure 2.4 shows a region of sudden increase in S_{2n} in the $A \approx 100$ area, the region of interest for this thesis. It could be explained by a drastic change in the nuclear shape from spherical to deformed (see Section 2.1.2 and Chapter 5 for more detailed discussion).

As indicated in Chapter 1, mass models try to predict the mass surface and help in understanding nuclear structure far from the valley of stability. In particular, nuclear models and mass formulas help to predict the unknown binding energies. Many models have been developed since the 1930's as

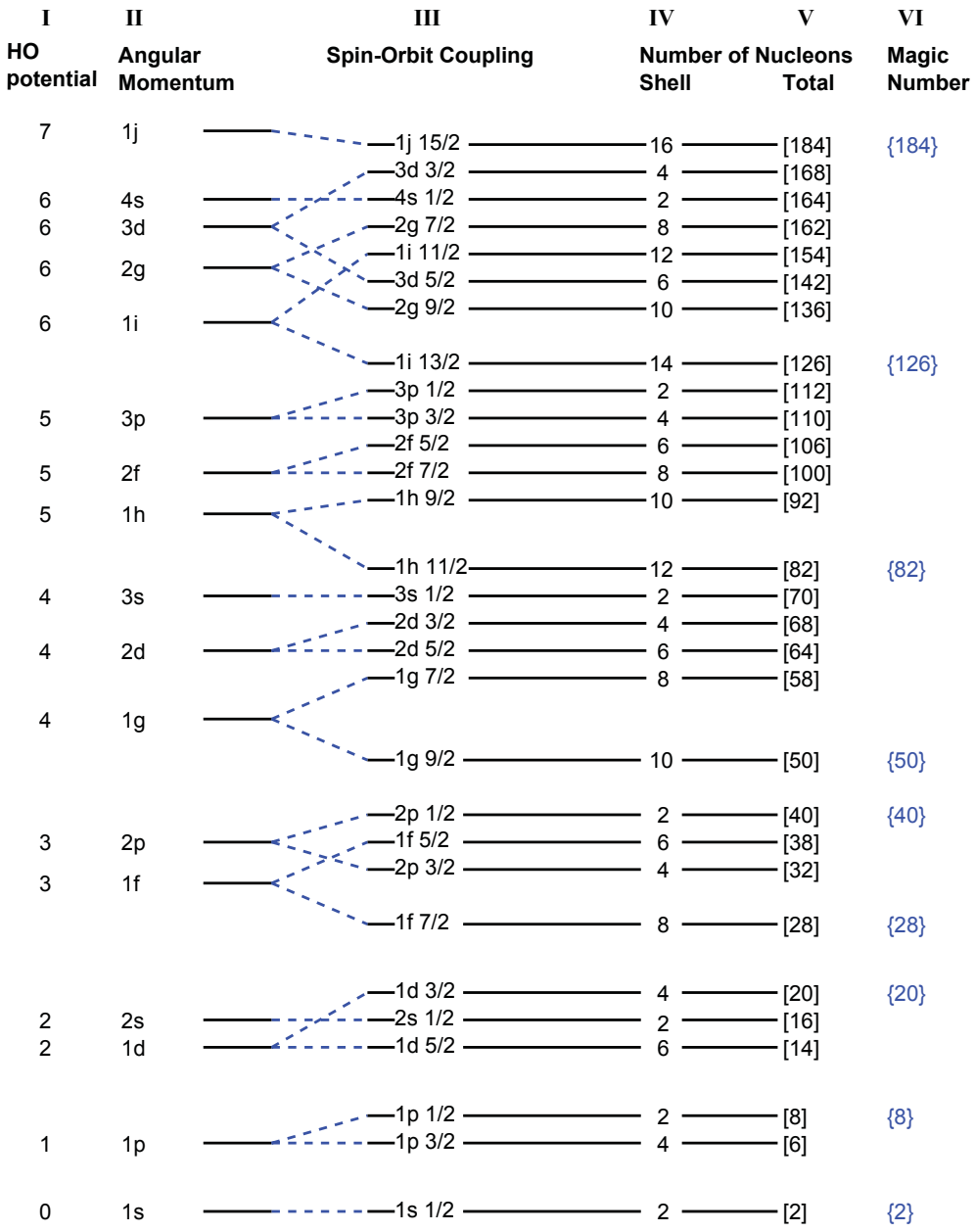

Figure 2.3: Nuclear Shell Model. A single-particle shell model with a harmonic oscillator (HO) potential (first column) including angular momentum (second column) and with spin-orbit (third column) interaction. The fourth column indicates the level degeneracy, the number of nucleons per shell. The resulting magic numbers are shown in the last column, representing shell closures. The figure is inspired by M. Goeppert Mayer and J. H. Jensen [29].

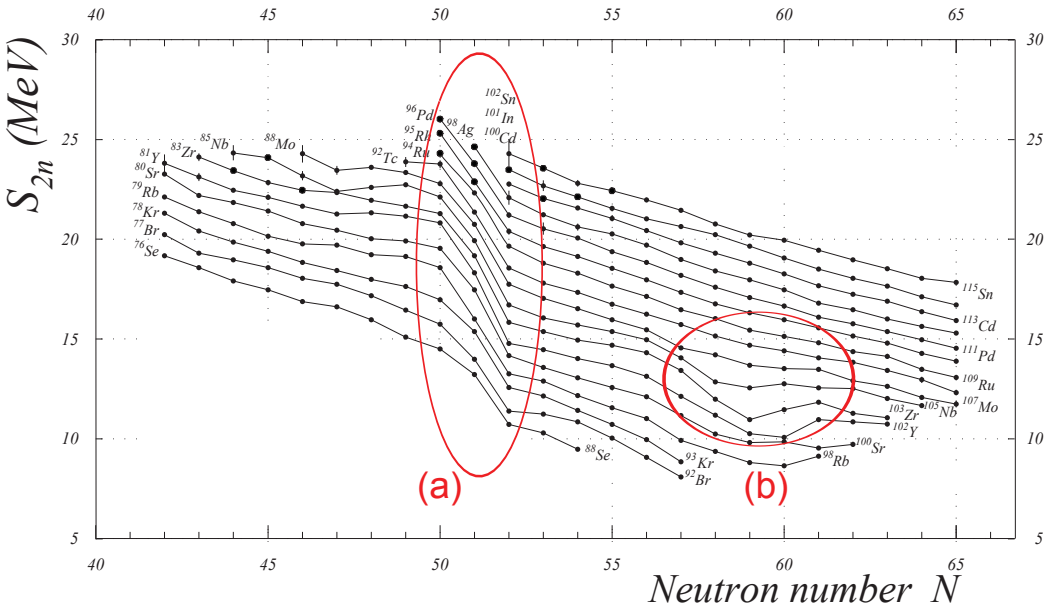

Figure 2.4: Experimental two-neutron separation energies S_{2n} plotted as a function of neutron number $N = 40 - 65$. Each line represents an isotopic chain. In red is marked the striking signatures of nuclear structure: (a) the shell closure at $N = 50$ and (b) deformation in the $A \approx 100$ region, which appears as a sudden increase in S_{2n} values. Figure from the Atomic-Mass Evaluation 2003 (AME2003) [28].

reviewed in [2]. In general, three approaches have been used: macroscopic, microscopic, and microscopic-macroscopic.

The Liquid Drop Model (LDM), as mentioned earlier, describes the nucleus as one body influenced by the collective behavior of its constituent nucleons. It completely ignores the quantification of the energy or the well-known shell behavior of the nucleus. This led to a second approach, the microscopic-macroscopic model, which is similar to the LDM but with additional quantum-mechanical terms added for shell effects, pairing features, represented by the Wigner term (a term which appears in the counting of identical pairs in a nucleus and is proportional to the charge symmetry parameter I [30]), etc. A more sophisticated version is known as the Finite-Range Droplet Model (FRDM) [31].

A microscopic approach to describe the complete nucleus is the variational Hartree-Fock-Bogolyubov method (HFB) [32], which unifies the self-consistent description of nuclear orbits as given in the Hartree-Fock method using an effective interaction, and a phenomenological Wigner term. Here the Wigner term describes a strong interaction in nuclides with $N = Z$, whereas the pairing force is needed to account for the odd-even staggering of the binding energy as a function of neutrons and protons. The variational wave function is a linear combination of independent particle states representing the various possibilities for nucleon occupation of single-particle states [33]. The goal is to find a description of nuclides for all areas of the nuclide chart, for example in the vicinity of the magic nuclides and for the regions of deformation (see Section 2.1.2), which are usually mid-shell. A density-dependent HFB-model where pairing correlations are included is the so-called Gogny Model [32]. Different parameter sets have been proposed [34], where a recent Gogny parameterization D1M [13, 35, 36] tries to fit the model to more regions of deformation, especially in the $A \approx 100$ region.

The Duflo-Zuker model [37] is derived from a shell-model Hamiltonian (e.g. [38, 39]). The Hamiltonian is separated into a monopole term, which describes the single particle energies, and a multipole term, which accounts for the residual interactions, allows configuration mixing, and includes pairing and the Wigner correlation. The monopole and multipole parts are parameterized by the application of symmetry and scaling. Thus, saturation and configuration mixing are achieved such that the magic numbers as well as the regions of strong deformation are described. For a detailed description and comparison of the models mentioned, see the review article [2].

Measuring masses further away from the valley of stability serves two main purposes. First, it enhances our knowledge about nuclear structure, and second, it helps to refine and to constrain mass models. The inclusion of empirical mass values in mass models strengthens and extends their

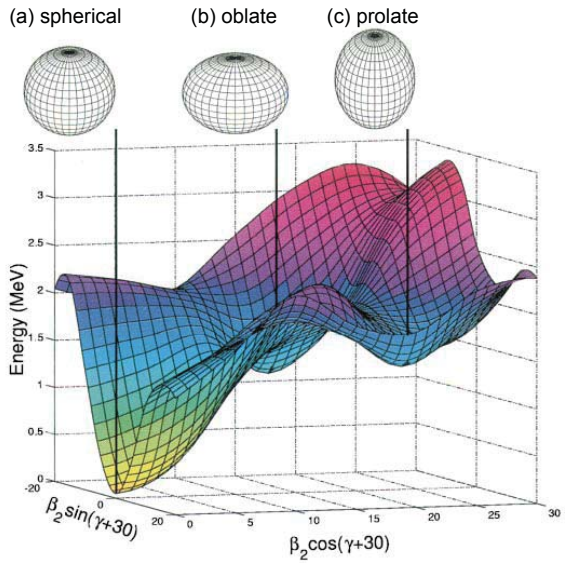

Figure 2.5: Calculation of the potential energy surface in ^{186}Pb with indication of three minima of different shape: (a) spherical, (b) oblate, and (c) prolate. The mass region around $A \approx 100$ will show nuclear shape transitions from spherical to oblate to prolate (see Chapter 5). Picture modified from [40].

predictive power, and gives anchor points for extrapolations.

2.1.2 Nuclear deformation and phase transition

Similar to magic numbers, sudden deformations appear as discontinuities in some observables like the two-neutron separation energy. The deformation in the $A \approx 100$ region shown in Figure 2.4(b) is such an example. Nuclei are considered to be deformed when they deviate from a spherical shape. For example, the nucleus may acquire an elongated shape that can be represented approximately as an ellipsoid where the ratio of the long to short axes is considerably large. Figure 2.5 shows three different nuclear shapes that are interesting for the $A \approx 100$ region and are discussed in Chapter 5. The deformation may appear in the ground state and also in excited states. Being deformed, the excited nucleus starts to rotate since it is not isotropic in shape.

The nuclear shape deformations are the result of the collective behavior of the nucleons. Hence, they are described by collective models or macroscopic and microscopic-macroscopic models. However, these models often ignore or neglect some important microscopic effects which are usually responsible for

the shape that the nucleus takes, and most often they cannot predict shape deformations.

The nuclear shape phase transitions, unlike the classical phase transitions, are caused neither by pressure or temperature changes nor by other external forces, but they are rather governed by the occupancy of single-particle orbitals by protons and neutrons. A quantum phase transition [41] can also be understood as a phenomenon called shape coexistence [40] (see Figure 2.5), which leads to a sudden change in the ground-state binding energy. This is due to the competition between deformed and non-deformed structures in this region resulting from a slight difference in their binding energies [42], as can be seen for ^{186}Pb in Figure 2.5.

In this thesis, the impact of mass measurements on the behavior of nuclear shape transitions in the region of interest ($A \approx 100$) are discussed in Chapter 5. The Rb and Sr isotopes transition from an oblate to a prolate shape which can be seen as a sudden jump in the two-neutron separation energies as well as in the charge radii.

2.2 Nuclear Astrophysics

2.2.1 Nucleosynthesis of the elements

On earth 272 stable and 55 natural radioactive nuclides have been found [43]. One of the most important questions to nuclear astrophysics is the explanation of the relative abundance of these different elements and their isotopes not only on earth but also in the solar system and in fact the entire universe in general.

Beyond nickel (^{62}Ni), the binding energy per nucleon decreases because of the increasing Coulomb barriers. Hence these nuclides cannot be produced by fusion reactions in stars. The origin of the elements beyond iron and nickel (and the region of interest for this thesis) is not fully understood. It is believed that the majority of these elements have been produced by neutron capture processes, where a seed nucleus, the nuclide that is the starting point of the reactions, captures a number of neutrons until a (n,γ) $\rightleftharpoons$ (γ,n) equilibrium is established at the so-called waiting point nuclides. When this radioactive nuclide undergoes β-decay a new, heavier element is created. A schematic plot of this process can be seen in Figure 2.6.

For the creation of elements beyond iron various nucleosynthesis scenarios and astrophysical sites have been proposed. The paths of some of the most important scenarios can be identified in that mass region. These include the slow neutron capture process (s-process), the rapid neutron capture process (r-process), the photo-disintegration process (p-process) [44], and the rapid proton capture process (rp-process). Figure 2.6 displays the proposed paths of some of these nucleosynthesis processes on the chart of nuclides. Whether the aforementioned processes are enough to build up the solar system element abundance as shown in Figure 2.7 is still under discussion. A comprehensive and quantitative description of these processes is required for the understanding of stellar evolution, of stellar explosion mechanisms, and of galactic chemical evolution processes [17].

Important information about stellar production mechanisms and even about physical conditions at the respective stellar sites can be deduced from isotopic abundance patterns of the elements between iron and the actinides found in the solar system as well as in meteorites in the form of presolar grains and from the spectrum of sunlight [45]. The reproduction of the observed abundance pattern provides a crucial test of the increasingly sophisticated stellar evolution models. Nuclear properties have an impact on those astrophysical models [17]. Since nucleosynthesis processes are the most promising to explain the solar abundance, nuclear properties that are involved in these processes have a direct effect. From the different processes mentioned above,

the r-process (see Section 2.2.3) will be of focus in this thesis. To determine, to understand better, and to characterize the location of the r-process path, mass measurements have been performed in the scope of this thesis. A focus is drawn to the $A \approx 100$ region for neutron-rich rubidium and strontium, the region of interest, which is directly located on possible r-process paths. The red ellipse in Figure 2.6 and the red stars in Figure 2.8 indicate the position of the measured nuclides.

In Figure 2.1, the location of possible r-process paths are highlighted in green. Nuclear structure, especially the magic numbers from the Shell Model, manifests itself directly in the s- and r-process abundance (see Figure 2.7). At neutron-shell closures (e.g. $N = 82$ and 126) the path of the r-process encounters waiting-point nuclides where it undergoes β-decay back into stable isotopes. The additional capture of a neutron on the nuclei with such magic neutron numbers is hindered by the reduced energy gain which slows down the the neutron capture process at this point. Hence, the result is an increase in the r-nuclide abundance as can be seen in Figure 2.7 (e.g. $A \approx$130 (xenon), 195 (platinum), etc.).

2.2.2 The s-process

Approximately half of the elemental abundances between Fe and Bi are produced by the well-characterized s-process, which is associated with stellar He burning scenarios in evolved Red Giant stars [46]. The s-process occurs at relatively low neutron densities ($N_n = 10^6$ cm^{-3}) and intermediate temperatures ($T \ll 1 - 3 \cdot 10^8$ K) [46]. Under these conditions, the rate of neutron capture is slow relative to the rate of β-decay, which corresponds to neutron capture times to be longer than typical β-decay half-lives. The synthesis takes place during the hydrogen-helium intershell burning phase of Asymptotic Giant Branch (AGB) stars at relatively low temperatures ($T = 1{\cdot}10^8$ K). Thus, the s-process follows along the valley of beta stability, as can be seen in Figure 2.6, starting at the abundant seed nuclei of the iron group elements and ending at the alpha-unstable trans-bismuth isotopes.

2.2.3 The r-process

Unlike the s-process, the r-process [17] is not well understood. In particular, the production site (or sites) has not been found that produce the solar r-process nuclei abundance shown in Figure 2.7. In general, the r-process has been suggested to explain the abundances of neutron-rich nuclei which cannot be produced by the s-process [43]. The r-process is characterized by high neutron densities of 10^{20} to 10^{24} cm^{-3} and time scales of a few

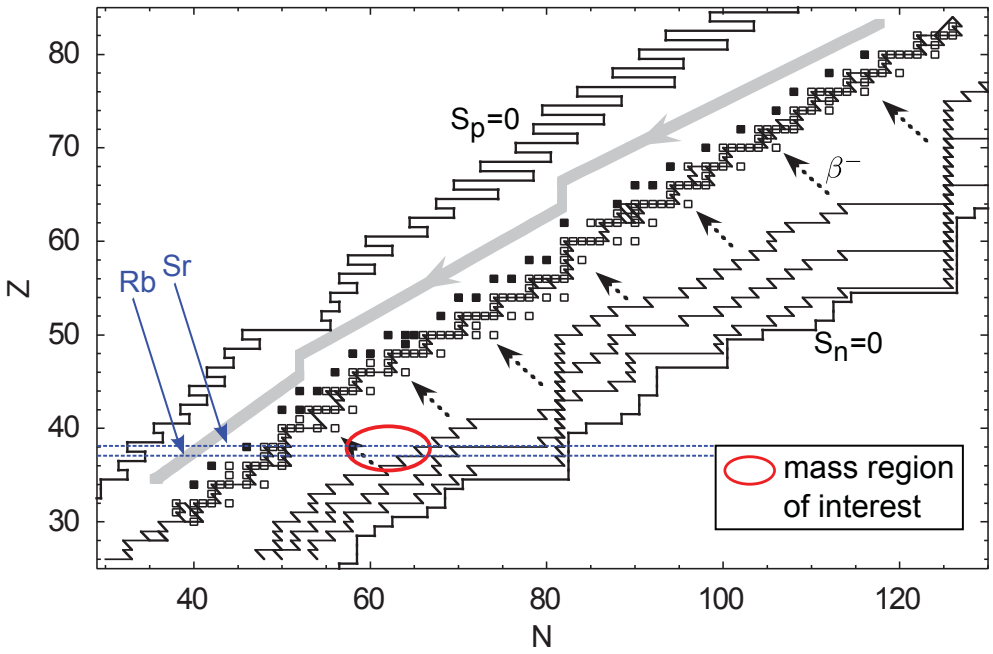

Figure 2.6: Location in the (N,Z)-plane of the stable isotopes of the elements between Fe and Bi. The *p*-nuclides are represented by black squares, while both the *s*- and *r*-isotopes are identified with open squares. The *p*-nuclides are the progeny of unstable neutron-deficient isobars located on the down-streaming *p*-process flow (thick gray line with arrows). The *r*-process contribution to the *r*-only, and *s*- and *r*-nuclides is provided by the decay (represented by arrows) of the neutron-rich nuclides located on the up-streaming *r*-process flow (three such flows are represented by black solid zigzag lines) associated with some *r*-process models. The up-streaming *s*-process flow (thin black line) is confined at the bottom of the valley of nuclear stability and brings the *s*-process contribution to the *s*-only, and *s*- and *r*-nuclides. The proton and neutron drip-lines represent the approximate locations of zero proton and neutron separation energies. Figure from [17].

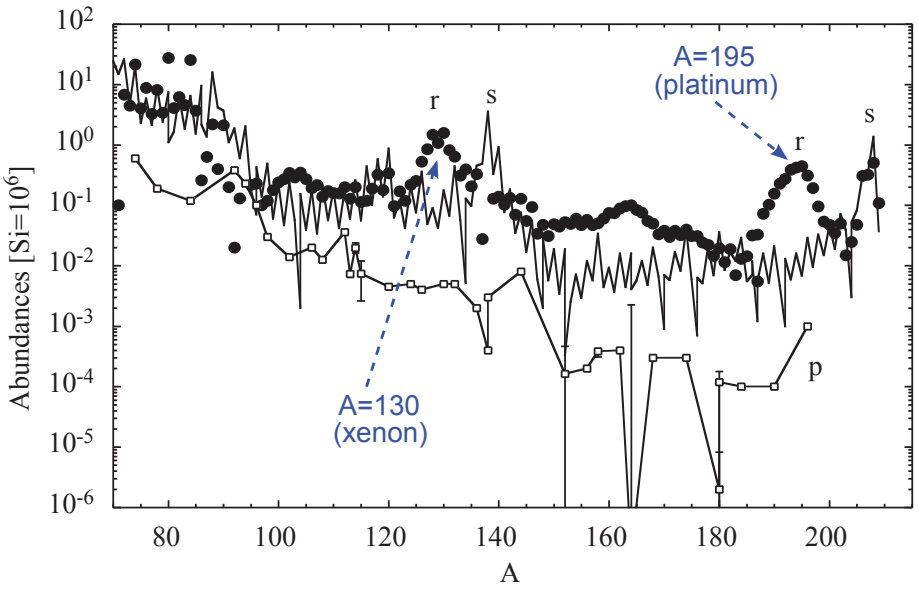

Figure 2.7: Decomposition of the solar abundances of heavy nuclides by *s*-process (solid line), *r*-process (dots), and *p*-process (squares) contributions. Figure from [17].

seconds [17]. These conditions clearly point to an explosive scenario, e.g. core collapse supernovae (i.e. Supernova Type II), for the astrophysical site. Other potential sites will be addressed in the next subsection.

Due to the high neutron densities, the seed nuclei capture many neutrons in a very short time interval, driving the *r*-process path along isotopic chains to very neutron-rich species until a (n,γ) $\rightleftharpoons$ (γ,n) equilibrium is established at the waiting point nuclides. At neutron-shell closures the *r*-process is slowed down by these waiting-point nuclei, which have comparatively long half-lives with regard to β-decay. Figure 2.8 shows two possible canonical *r*-process paths in a classical *r*-process waiting-point approximation [47, 48] indicating that components with low neutron density pass through the investigated mass region. Hence, it is important to determine masses relevant for this region. Even reaction paths (e.g. blue line in Figure 2.8) for higher neutron densities (10^{24} cm^{-3}) are only a few neutron numbers away, which substantially reduce the challenge for theoretical mass models.

During the peak neutron flux, the relevant nuclear physics information concerns the neutron separation energies (Equation (2.2)), which determine the (n,γ) $\rightleftharpoons$ (γ,n) equilibrium, and the β-decay rates of the waiting point nuclei, which are important for both the duration of the *r*-process and the

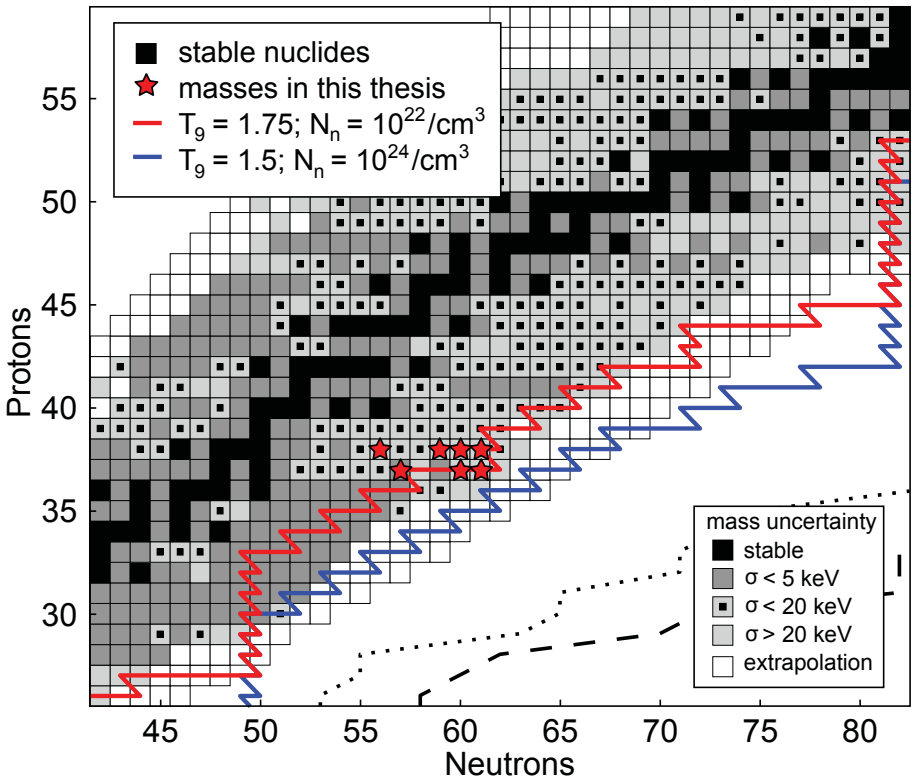

Figure 2.8: Section of the chart of nuclides. The neutron-rich nuclei studied in this thesis are indicated by red stars. Two r-process paths calculated by waiting-point approximations [47, 48] at two different temperatures and neutron densities are shown. The red (blue) lines indicate a high (low) temperature and low (high) neutron density scenario. Additionally, the mass uncertainty is displayed as well as two neutron drip-lines from different mass models: FRDM (dotted line), HFB-D1M (dashed line).

r-process abundance pattern.

r-process models

Testing r-process models against abundance observations requires knowledge of nuclear physics and astrophysics that translates a set of evolving astrophysical conditions into a characteristic nuclear abundance pattern. Nuclear input data of importance to r-process models are nuclear masses, β-decay half-lives, and branching ratios for neutron emission. Fission rates and fission fragment distributions, neutrino interaction rates, and charged-particle fusion rates play a minor role [49].

In r-process models characterized by an (n,γ) $\rightleftharpoons$ (γ,n) equilibrium, the reaction path for a given set of astrophysical conditions is governed by nuclear masses and the corresponding separation energies. However, many of the nuclei in the r-process are experimentally inaccessible. Hence, nuclear astrophysics calculations rely heavily on theoretical mass predictions, which are performed by models with parameters that are adjusted to known masses [2]. Experimental mass data on neutron-rich nuclei are therefore not only needed as direct input into r-process model calculations but also to test and to improve mass models and to reduce the uncertainty in the extrapolations. A detailed understanding of the r-process, which is possible with well-determined input data, will provide a more profound knowledge about isotope-production processes in our solar system, and the mass measurements of neutron-rich Rb and Sr isotopes presented in this thesis are a step towards reducing the uncertainties of nuclear physics input for r-process-model uncertainties.

Although the r-process sites remain unknown, many astrophysical models and sources for r-process elements have been proposed during the past 50 years, including, in particular, scenarios such as an explosion on a neutron-star surface [50], a collision of a neutron star with a black hole [51], an explosion of a low-mass neutron star [52], and the hypothetical escape of nucleon bubbles in the case of a soundless stellar collapse [53]. Presently, however, it seems most likely that rapid neutron-capture nucleosynthesis can take place during different stages of supernova explosions [54] or in neutron star mergers [55]. An overview of the discussed possible sites is given in the review paper by Arnould *et al.* [17].

High-entropy wind model

Supernova explosions still remain the preferable site for the distribution of r-process material all over the Galaxy [58]. The neutrino-driven wind from a hot neutron star produced in a supernova explosion has been considered as a

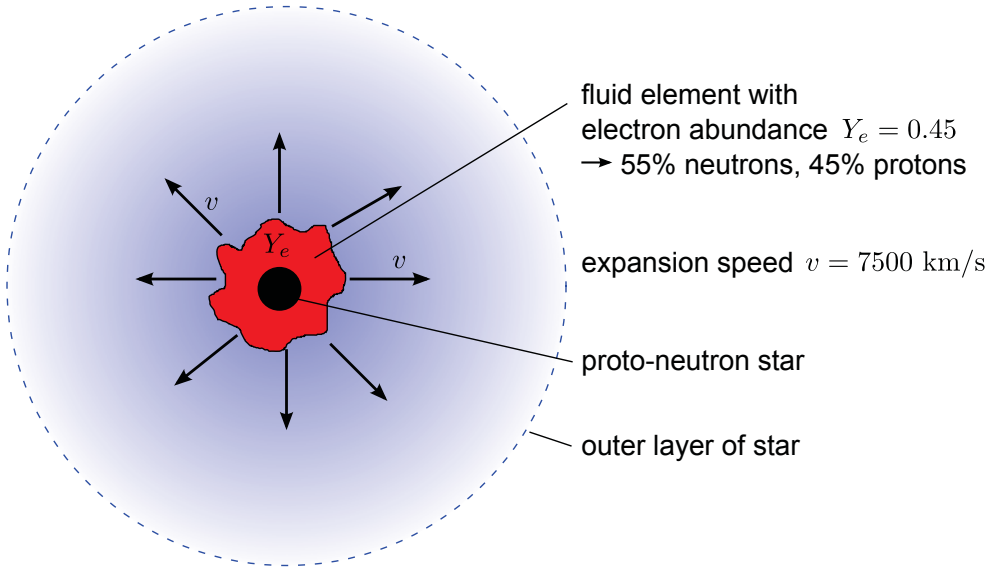

Figure 2.9: Schematic plot of the high-entropy wind model as used in this thesis. It is based on a neutrino-driven wind emerging from the nascent neutron star in a core collapse supernova explosion [56,57]. The fluid element of matter (red) (electron abundance Y_e) is shown behind the shock front of the supernova explosion and above the proto-neutron star (black), and is expanding with velocity v.

probable site for the r-process by many authors (e.g. [54, 59–63]). A part of the surface material of a neutron star is heated by the supernova neutrinos and gets ejected. This can be described as a hot outflow with a fairly high entropy and a moderate density. A schematic plot shown in Figure 2.9 illustrates this scenario. Winds are characterized by a monotonically increasing velocity and a continuously decreasing temperature when the radius of the supernova explosion is assumed to go to infinity.

A parameterized, fully dynamical r-process model [57] following Freiburghaus *et al.* [64] will be used in Chapter 5 to identify the astrophysical implications due to the mass measurements presented in this thesis. The model is inspired by the conditions assumed in high-entropy winds emerging from the nascent neutron star in a core collapse supernova explosion. It assumes a fluid element, as seen in Figure 2.9, that is heated to a very high temperature ($T \approx 9$ GK) and that is composed of protons and neutrons, with the electron abundance Y_e being set by weak interactions. The fluid element then undergoes a rapid expansion at constant velocity v, Y_e, and entropy S as illustrated in Figure 2.9.

The model is coupled to a full reaction network with 5410 nuclides that includes all relevant charged particles, β-decays, and neutron capture rates. Calculations are carried out for a full range of entropies with the resulting isotopic abundances being calculated equal weight. For unknown masses, mass extrapolations from [28] and calculated values from the FRDM model [31] were used. Masses enter exponentially in the calculation of (γ,n)-photodisintegration rates from the forward (n,γ)-rates via detailed balance. A detailed discussion can be found in Section 5.5.

Using this model an r-process abundance calculation was performed for neutron separation energies [28] known prior to the results of this thesis. To encounter differences in the abundance pattern between changes in the neutron separation energies, and thus probe the sensibility of the possible mass measurement towards the model, two different mass data sets were used. The neutron separation energies [28] for $^{96-99}$Rb and $^{96-100}$ were varied by their 3σ uncertainties either all up (AME03high) or all down (AME03low). Such a deviation, even though simplified by assuming that all changes occur in the same direction, is not uncommon for non-Penning-trap mass measurements and extends up to 6σ in neutron separation energies compared to previous measurements in this work. Figure 2.10 shows the resulting composition produced by the r-process model used in this thesis (in dashed red and solid black lines) (see Chapter 5). The difference in the abundance pattern shows the sensibility of the astrophysical nucleosynthesis process to the deviations in neutron separation energies of the nuclides in the neutron-rich Rb and Sr region. In addition, Figure 2.10 shows the resulting elemental abundance uti-

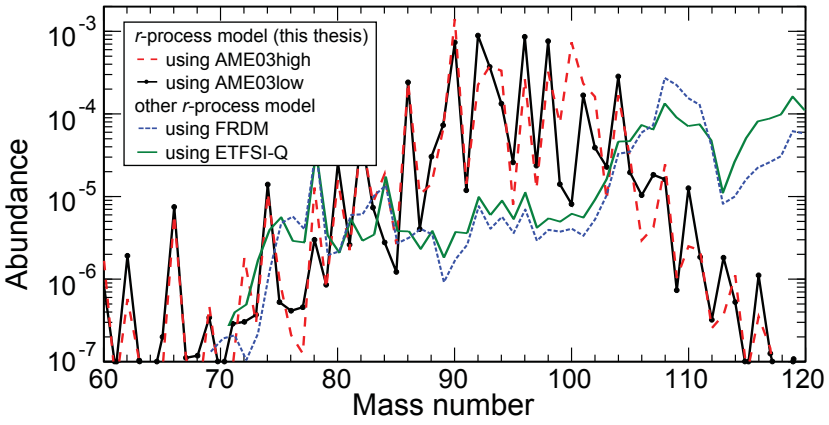

Figure 2.10: Calculated r-process abundance as a function of mass number for a single entropy component for different neutron separation energies. The r-process model used in this thesis is shown using two different sets of separation energies while varying the energies of $^{96-99}$Rb and $^{96-100}$Sr from AME03 [28] by their uncertainties with 3σ up (AME03high, dashed red) and down (AME03low, solid black). Another r-process model [65] is shown using two different mass models, FRDM [66] (dashed blue lines) and ETFSI-Q [67] (solid green lines).

lizing another r-process model approach by Arcones and Martínez-Pinedo *et al.* [65], where a high-entropy neutrino-driven wind in supernovae explosions is modeled using two different mass models, FRDM [66] (dashed blue lines) and ETFSI-Q [67] (solid green lines). The importance of the $A \approx 100$ region for Rb and Sr is evident in the larger deviation between the resulting abundance of using AME03high and AME03low than using the two different mass models. A smaller uncertainty in the mass values in the $A \approx 100$ region, as well as precise and accurate values themselves are required to reduce the nuclear physics uncertainties for the astrophysical r-process understanding.

Sensitivities of mass values and their uncertainties measured in this thesis are determined in Chapter 5 using such a high-entropy wind model. The uncertainties of nuclear physics input in the region of interest can be reduced helping nuclear astrophysics in refining of suitable models.

Chapter 3

Principles of Penning-Trap Mass Spectrometry

Nuclear masses can be determined using both indirect and direct methods. The so-called indirect techniques involve mass determination from nuclear reactions or radioactive decay. The mass of an unknown nuclide can be determined by measuring the Q-value, the difference in mass between the parent and the daughter nuclei, or by detecting the kinematics of the reaction products of a nuclear reaction [68]. Absolute atomic mass values can then be derived by linking this mass difference to a known mass [2]. Direct mass measurements can be performed with storage rings, with Penning traps, or other techniques. Charged-particle traps have gained popularity over the last four decades as a tool for ion beam preparation and for precision experiments (e.g. [69]). Their versatility led to the Nobel Prize for Wolfgang Paul and Hans Dehmelt, the inventors of the two most widely used traps, the Paul trap [70] and the Penning trap [71] respectively. Applications range from quantum computing (e.g. [72]) to Penning trap mass spectrometry (e.g. [1]). The latter can achieve the highest precision and accuracy of atomic mass measurements [1] at present and is the subject of this thesis.

A theoretical description of an ion in a Penning trap will be discussed in Section 3.1. Furthermore, ion excitation schemes and mass determination using a Penning-trap system will be reviewed in Section 3.2. A discussion of the achievable measurement precision closes this chapter and motivates the Cooler Penning trap described in Chapter 6 and 7.

3.1 Principles of ion trapping using Penning traps

In recent years Penning traps have been widely used in many different fields of physics. Examples include: measurement of the magnetic moment of the electron/ positron, determination of the fine structure constant [73], mass spectrometry [1], measurement of nuclear magnetic dipole moments, test of Bound-State Quantum Electrodynamics, test of the unitarity of the CKM matrix, production, trapping and spectroscopy of antihydrogen, quantum computation with ions, and many more. In mass spectrometry, Penning traps have evolved to become the tool of choice for high-precision mass measurements [1].

A Penning trap is a charged particle trap which allows one to confine particles in a well defined environment. Three-dimensional confinement of charged particles requires a potential minimum. Earnshaw's theorem [74] states that it is not possible to generate an electrostatic potential with a three-dimensional minimum in free space. However, it is possible to overcome this by superimposing a magnetic field $\vec{B}$ (Penning trap), by using a time-dependent electric field (Paul trap), or by not using free space (similar to an electron beam ion trap (EBIT)). A short introduction to the theory of Penning traps will be discussed below. More detailed descriptions can be found in [1, 75–79].

3.1.1 The ideal Penning trap

Charged particles are confined in a Penning trap by the combination of a homogeneous magnetic field $\vec{B}$ and a weak static electric field $V(z, r)$ with cylindrical symmetry. The latter is created by applying a voltage V_0 between the hyperbolic ring and the two hyperbolic end-cap electrodes. Schematics of a hyperbolic and a cylindrical, a common approximation, Penning trap are shown in Figure 3.1.

In the absence of an electric field present, an ion with charge-to-mass ratio q/m and velocity v perpendicular to a magnetic field $\vec{B} = \vec{B}(z)$ in the z-direction will experience the Lorentz force, $\vec{F}_L = q\vec{v} \times \vec{B}$. This force will radially confine the ion in the radial plane, perpendicular to $\vec{B}$, resulting in a circular motion with the cyclotron frequency

$$\omega_c = \frac{q}{m} \cdot B. \tag{3.1}$$

Along the direction of the magnetic field, the ion is not confined and will escape the trap if it has any velocity component in this direction. Axial

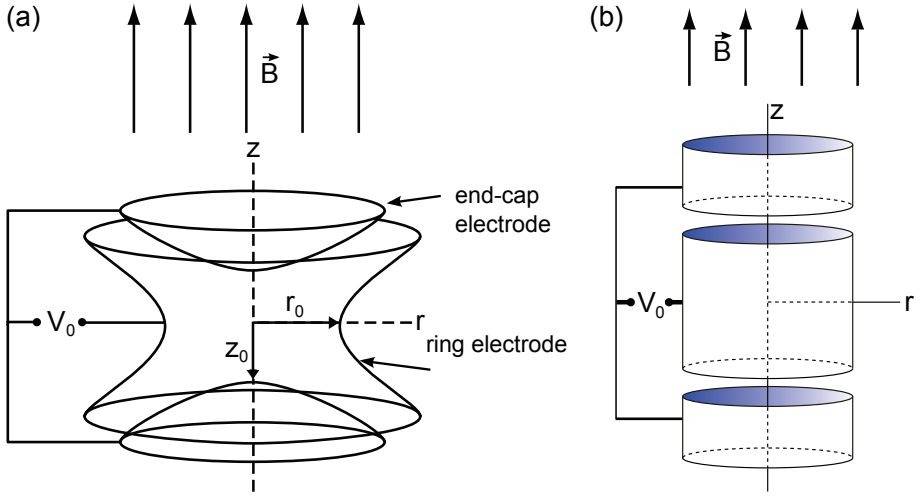

Figure 3.1: Schematic drawing of the electrode configuration of two types of Penning traps. (a) Hyperbolic and (b) cylindrical Penning trap. A voltage V_0 is applied between the ring and end-cap electrodes to trap charged particles.

confinement is achieved by superimposing a weak static electric quadrupole potential. It can be generated by applying a voltage difference V_0 between the end-cap electrodes and the ring electrode, as shown in Figure 3.1(a), which leads to

$$V(z,r) = \frac{V_0}{2d^2} \cdot \left(z^2 - \frac{1}{2} r^2 \right). \tag{3.2}$$

The parameter d is known as the characteristic trap dimension. It is given by

$$d^2 = \frac{1}{2} \left(z_0^2 + \frac{r_0^2}{2} \right), \tag{3.3}$$

where r_0 is the inner ring radius and $2z_0$ the closest distance between two end-cap electrodes. Figures 3.2 (a) and (b) show the electric-field lines generating a quadrupole potential for a hyperboloidal and cylindrical Penning trap representing the TITAN Measurement Penning trap (MPET) and the TITAN Cooler Penning trap (CPET), respectively. The z-direction is from top to bottom and corresponds to the path of ion injection as well as ejection.

The two electric-field components are given by

$$E_z = -\frac{V_0}{d^2} \cdot z \qquad \text{and} \qquad \vec{E}_r = \left(\frac{V_0}{2d^2} \right) \cdot \vec{r}. \tag{3.4}$$

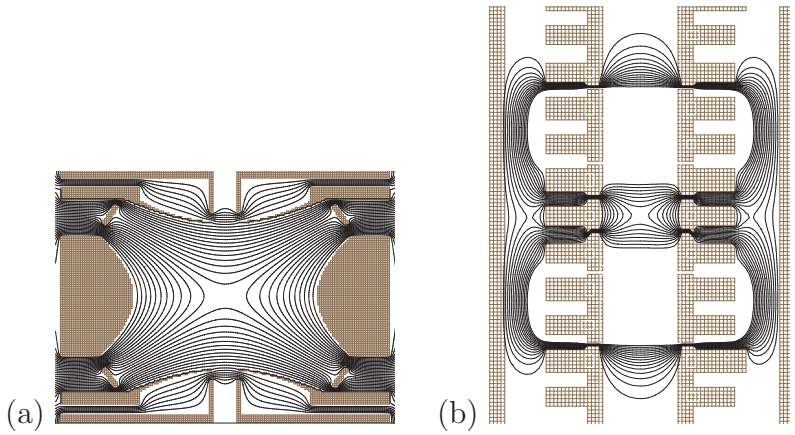

Figure 3.2: Two SIMION [80] simulations of two existing Penning-trap configurations at TITAN: (a) The measurement precision Penning trap (MPET) with its hyperboloidal electrode structure and (b) a section of the cooler Penning trap CPET with its cylindrical electrode structure. The orientation of the z-axis is from top to bottom. The characteristic trap dimensions are (a) $d_0 \approx 11.21$ mm [79] and (b) $d_0 \approx 141.98$ mm for the whole trap (see Chapter 6).

The equation of motions of an ion in such an electromagnetic field are

$$m\frac{dz}{dt} = qE_z \qquad \text{and} \qquad m\frac{d\vec{r}}{dt^2} = q\left(\vec{E}_r + \frac{d\vec{r}}{dt} \times \vec{B}\right). \tag{3.5}$$

for the axial and radial direction, respectively. Solving the equations of motion results in the three motional modes, as shown in Figure 3.3, with three associated eigenfrequencies: one axial ω_z, and the two radial, namely magnetron ω_-, and reduced cyclotron ω_+ frequencies.

$$\omega_z = \sqrt{\frac{qV_0}{md^2}} \qquad \text{and} \tag{3.6}$$

$$\omega_\pm = \frac{\omega_c}{2} \pm \sqrt{\frac{\omega_c^2}{4} - \frac{\omega_z^2}{2}}. \tag{3.7}$$

An example of the trajectory of a positively charged particle is displayed in Figure 3.3. The figure shows the superimposition of all three motions in red as well as projections of the individual motions on the walls of the cube.

The following relationships for the angular eigenfrequencies can be derived:

$$\omega_c = \omega_+ + \omega_- \tag{3.8}$$

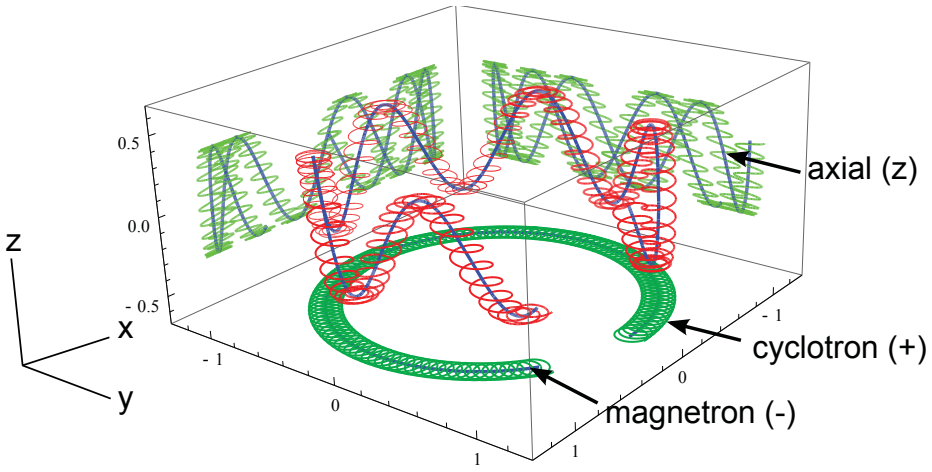

Figure 3.3: Schematic trajectory (red) corresponding to the sum of the three independent eigenmotions of an ion in a Penning trap. On the walls of the cube projections of the ion's motion (green, blue) can be found: The harmonic oscillation in the axial direction (ω_z) and a superposition of two radial motions, the reduced cyclotron (ω_+) and the magnetron motion (ω_-).

$$\omega_c^2 = \omega_+^2 + \omega_-^2 + \omega_z^2 \tag{3.9}$$

$$2 \cdot \omega_+ \omega_- = \omega_z^2 \tag{3.10}$$

Equation (3.8) plays a key role in high-precision mass measurements and will be discussed in Section 3.2. The relation in Equation (3.9) is relevant for 'real' (i.e. non-ideal) Penning traps and is the so-called Brown-Gabrielse Invariance Theorem [75].

Equations (3.6) and (3.7) can result is imaginary or complex values for the eigenfrequencies. In such a case the field combination will not lead to bound trajectories. Thus, trapping requires the conditions $qV_0 > 0$ and $\omega_c^2 - 2\omega_z^2 \geq 0$. With the help of Equations (3.1) and (3.6) this condition can be rewritten using the ratio m/q

$$\frac{m}{q} \leq \left(\frac{m}{q}\right)_{\text{critical}} = \frac{d^2}{2}\frac{B^2}{V_0}, \tag{3.11}$$

where $(m/q)_{\text{critical}}$ is the critical mass-over-charge ratio.

At the limit of the trapping condition, the two radial eigenfrequencies are identical, i.e. $\omega_+ = \omega_-$. However, Penning traps are usually operated

well below this limit ($\omega_c \gg \sqrt{2} \cdot \omega_z$) to establish a hierarchy in all three eigenfrequencies

$$\omega_+ \gg \omega_z \gg \omega_-. \tag{3.12}$$

Taking a Taylor expansion of Equation (3.7) and using Equation (3.12) allows the radial frequencies to be expressed as

$$\omega_+ \approx \omega_c - \frac{\omega_z^2}{2\omega_c} \tag{3.13}$$

$$\omega_- \approx \frac{\omega_z^2}{2\omega_c} \tag{3.14}$$

With Equation (3.6) these expressions can be written as

$$\omega_+ \approx \omega_c - \frac{\omega_z^2}{2\omega_c} = \frac{qB}{m} - \frac{V_0}{2d^2B} \tag{3.15}$$

$$\omega_- \approx \frac{\omega_z^2}{2\omega_c} = \frac{V_0}{2d^2B}, \tag{3.16}$$

which shows that the magnetron motion ω_- is approximately independent of the mass and charge of the ion. The reduced cyclotron frequency ω_+ is a consequence of the repulsive radial electric potential that reduces the cyclotron frequency by a small amount ω_-. The magnetron frequency is a slow precession at the drift velocity $\vec{v}_d$ caused by the cross product of the electric and magnetic field:

$$\vec{v}_d = \frac{\vec{E} \times \vec{B}}{B^2} = \frac{\omega_z^2}{2\omega_c}\vec{r} \times \vec{z} = \omega_- \vec{r} \times \vec{z} \tag{3.17}$$

The position of an ion in a Penning trap can be parameterized by

$$x = r_+ \cos(\omega_+ t + \phi_+) + r_- \cos(\omega_- t + \phi_-) \tag{3.18}$$

$$y = r_+ \sin(\omega_+ t + \phi_+) + r_- \sin(\omega_- t + \phi_-) \tag{3.19}$$

$$z = r_z \cos(\omega_z t + \phi_z) \tag{3.20}$$

where r_z, r_+, and r_- are the amplitudes of the axial and radial motions with the corresponding phases ϕ_z, ϕ_+, and ϕ_-.

The total energy of a charged particle in a trap is

$$E = E_{\text{kin}} + E_{\text{pot}} = \frac{1}{2} m z_{\text{max}}^2 + m(\omega_+ - \omega_-) \cdot (r_+^2 \omega_+ - r_-^2 \omega_-). \tag{3.21}$$

where $z_{\max}$ and $r_{\pm}$ are the amplitudes and radii of each eigenmotion. The radial contributions to the total energy are

$$E_{r,\mathrm{kin}} = \frac{1}{2}mv_r^2 = \frac{1}{2}m\left[r_+^2\omega_+^2 + r_-^2\omega_-^2 + 2r_+r_-\cos\left((\omega_+ - \omega_-)t + \phi_+ - \phi_-\right)\right] \tag{3.22}$$

$$E_{r,\mathrm{pot}} = q\Phi = -\frac{1}{4}m\omega_z^2\left[r_+^2 + r_-^2 + 2r_+r_-\cos\left((\omega_+ - \omega_-)t + \phi_+ - \phi_-\right)\right] \tag{3.23}$$

With the hierarchy of the eigenfrequencies (Equation (3.12)) the kinetic term associated with the reduced cyclotron motion dominates over the potential term. For the magnetron motion the relation is inverted.

In a quantum mechanical description the motion of the charged particle can be quantized (see [75,81] for a detailed description). The Hamiltonian is formulated in canonical coordinates and momenta, and the classical Poisson brackets are replaced by quantum-mechanical commutator relations.

A 'real' Penning trap deviates from the ideal trap in many ways. The two most obvious are, that the end-caps electrodes require holes for injection and extraction, and the ring electrodes are finite in extent. The resulting deviation from an ideal quadrupole field in addition to field inhomogeneities, trap imperfections, misalignment of the trap axis with the magnetic-field axis, and more, lead to a shift in the trap eigenfrequencies, and thus to systematic uncertainties in the mass determination. In Section 5.2 the influence of these effects on the mass measurement of neutron-rich Rb and Sr isotopes will be discussed. More details on this topic can be found in [1, 75, 76, 79, 82]. In particular, a discussion of systematic uncertainties for the TITAN system can be found in [79].

3.2 Ion excitation and mass determination

This section will discuss Penning-trap mass measurement techniques which rely on the trajectory of an ion by driving the ion motion with external RF fields with a focus on those used at TITAN (see Chapter 4). The effect on the ion motion depends on the multi-polarity and the frequency of the driving field, and TITAN uses quadrupole and dipole fields applied in the radial plane (see Figure 3.4).

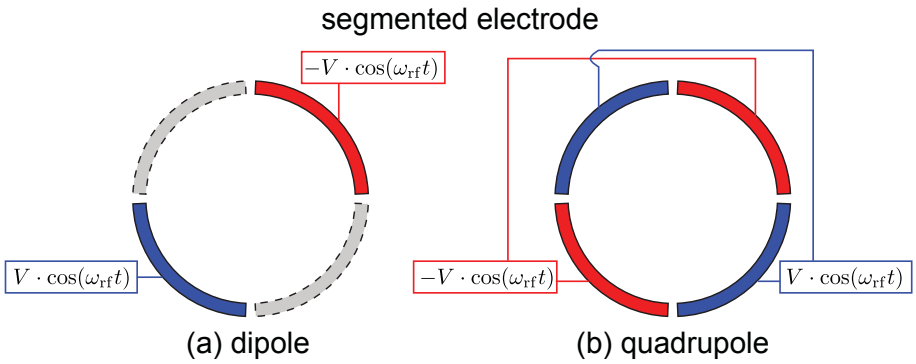

Figure 3.4: The guard electrodes are four-fold segmented to apply an RF field. The application of an RF on two opposite segments with a 180° phase shift results in a dipole field (a). While applying the same phase to opposite segments but with a 180° shifted RF to the second pair generates a quadrupole field (b).

3.2.1 Quadrupole excitation and the TOF-ICR method

The basic principle of Penning-trap mass spectrometry is measuring the cyclotron frequency ω_c. The mass is then determined using the time-of-flight ion-cyclotron-resonance method (TOF-ICR) [83, 84]. However, only the eigenfrequencies can be observed or excited directly, and the cyclotron frequency does not correspond to one of the ion's eigenmotions inside the Penning trap. Nevertheless, direct access to this frequency can be achieved by coupling the two radial eigenfrequencies through an external azimuthal quadrupole RF field,

$$V_{\mathrm{rf}} = -\frac{V_{0,q}}{2a^2} \cos(\omega_{\mathrm{rf}} t + \phi_{\mathrm{rf}}) xy, \tag{3.24}$$

with RF amplitude $V_{0,q}$ at a radius a. The angular frequency and phase of the RF field are ω_{rf} and ϕ_{rf} respectively. This RF is applied on a segmented guard electrode, as shown in Figure 3.4. Under the influence of such an RF field magnetron motion (ω_-) is converted into reduced cyclotron motion (ω_+), and vice versa, if ω_{rf} is equal to the sum of the two radial motions which in turn is equal to ω_c (see Equation (3.8)). For a given RF amplitude and excitation time, the ion's motion will be fully converted from one eigenmotion to another if $\omega_{\mathrm{rf}} = \omega_c$.

For injection into the MPET, the ions are prepared on a pure magnetron orbit (using a Lorentz steerer as discussed in Section 4.2.3), i.e. $r_-(t = 0) = r_-^i$ and $r_+(t = 0) = 0$. The axial motion is minimized. Under these initial

conditions, the amplitudes of the radial motions in the quadrupole RF field evolve as

$$r_+(t) = -\frac{1}{2}\frac{r_-^i k_0 e^{-i\Delta\phi}}{\omega_B}\sin(\omega_B t)\cdot e^{\frac{i}{2}(\omega_{\mathrm{rf}}-\omega_c)t} \tag{3.25}$$

$$r_-(t) = r_-^i\left(\cos(\omega_B t) + \frac{i}{2}\cdot\frac{\omega_{\mathrm{rf}}-\omega_c}{\omega_B}\sin(\omega_B t)\right)\cdot e^{\frac{i}{2}(\omega_{\mathrm{rf}}-\omega_c)t} \tag{3.26}$$

where

$$\omega_B = \frac{1}{2}\cdot\sqrt{(\omega_{\mathrm{rf}}-\omega_c)^2 + k_0^2} \tag{3.27}$$

$$k_0 = \frac{q}{m}\cdot\frac{V_{0,q}}{2a^2}\cdot\frac{1}{\omega_+ - \omega_-}. \tag{3.28}$$

Here, $\Delta\phi$ is the difference between the phases of the magnetron and reduced cyclotron motion of the RF. Phase-independent results [81] are only obtained for the initial conditions described above. As this is the case here, henceforth, all phases are set to zero. For $\omega_{\mathrm{rf}} = \omega_c$ the amplitudes reduce to

$$r_+(t) = r_-^i \sin\left(\frac{k_0 t}{2}\right) \quad \text{and} \quad r_-(t) = r_-^i \cos\left(\frac{k_0 t}{2}\right). \tag{3.29}$$

The period T for one full conversion from pure magnetron to pure cyclotron motion and back again is

$$T = \frac{2\pi}{k_0} = \frac{m}{q}\frac{\pi a^2}{V_{0,q}}(\omega_+ - \omega_-) = \frac{\pi a^2 B}{V_{0,q}}\cdot\left(1 - \frac{2\omega_z^2}{\omega_c^2}\right)^{1/2} \tag{3.30}$$

Following the hierarchy for the frequencies (Equation (3.12)), Equation (3.30) can be expressed as

$$T \approx \frac{\pi a^2 B}{V_{0,q}}\cdot\left(1 - \frac{\omega_z^2}{\omega_c^2}\right) = \frac{\pi a^2 B}{V_{0,q}}\cdot\left(1 - \frac{mU}{qB^2 d_0^2}\right) \tag{3.31}$$

with the trap dimension d_0 (see Equation (3.3)). In order to convert an initially pure magnetron motion into pure cyclotron motion, the product of the RF amplitude and the RF excitation time T_{rf} has to be a certain value:

$$k_0 = \frac{\pi}{T_{\mathrm{rf}}} \quad \text{therefore} \quad V_{0,q}\cdot T_{\mathrm{rf}} = \text{constant}. \tag{3.32}$$

Since $\omega_+ \gg \omega_-$, the radial (kinetic) energy is dominated by the reduced cyclotron motion, and a conversion between the two radial energies leads to a drastic change in kinetic energy. For the constant in Equation (3.32) (at which the initial magnetron motion is fully converted into reduced cyclotron

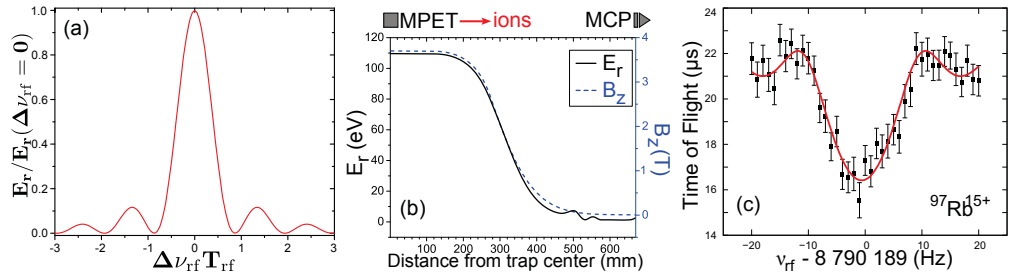

Figure 3.5: Principle of the time-of-flight ion-cyclotron-resonance detection technique. (a) Radial energy gain of the ion motion in the trap (MPET) in the case of a quadrupole excitation near ω_c. (b) During the extraction of the ions through the magnetic-field gradient, the ion's radial energy is converted into longitudinal energy. (c) Therefore, on the microchannel plate detector (MCP) the resonant ions have a shorter time-of-flight, and a resonance is visible at the true cyclotron frequency ω_c. Graphs (a) and (c) are both a function of the detuning frequency ν_{rf}.

motion), the radial energy is maximal. Hence, the radial energy is an indication for the degree of conversion between the two radial motions. Applying a combination of T_{rf} and RF amplitude that leads to a full conversion for $\omega_{\mathrm{rf}} = \omega_c$, and an energy gain of E_0 will lead to a smaller energy gain at a certain detuning $\nu_{\mathrm{rf}} = (\omega_{\mathrm{rf}} - \omega_c)/(2\pi)$ as follows from Equation (3.29):

$$E_r = E_0 \cdot \frac{\sin^2\left(\pi/2 \cdot \sqrt{1 + (2\Delta\nu_{\mathrm{rf}} T_{\mathrm{rf}})^2}\right)}{1 + (2\nu_{\mathrm{rf}} T_{\mathrm{rf}})^2}. \tag{3.33}$$

Figure 3.5(a) displays the radial energy after the RF field is applied as a function of the detuning and T_{rf}. A global maximum is found at $\Delta\nu_{\mathrm{rf}} = 0$ corresponding to $\omega_{\mathrm{rf}} = \omega_c$. At the end of the RF excitation for a given ω_{rf}, the ion is extracted from the Penning trap and passes through the magnetic-field gradient (shown in Figure 3.5(b)). The change in direction of the magnetic field applies a torque on the ion's initial magnetic moment:

$$\vec{\mu}(\omega_{\mathrm{rf}}) = \frac{E_r(\omega_{\mathrm{rf}})}{B_0}\vec{z}. \tag{3.34}$$

Thus, the work that is applied to the ion is expressed as

$$W = -\mu(\omega_{\mathrm{rf}}) \cdot B_z(z). \tag{3.35}$$

This results in a conversion of the kinetic energy gained from the radial motion into an axial kinetic energy.

After a RF-excitation time T_{rf} at ω_{rf} and the extraction from the Penning trap, the energy can be determined by measuring the TOF to the detector. Figure 3.5(b) shows the flightpath along with a simulation of the relationship between the radial kinetic energy and the axial magnetic-field strength. Equations 3.34 and 3.35 indicate that ions which are excited at the frequency $\omega_{\mathrm{rf}} = \omega_c$ have the largest kinetic energy gain, and thus the shortest time-of-flight. This measurement is then repeated for several frequency steps ω_{rf}, and a TOF resonance curve is obtained (see Figure 3.5(c)) from which ω_c of the ion (and thus the mass) can be calculated (with known B and q). The following analytical expression for the TOF [84] is then used to describe and fit the line shape:

$$T(\nu_{\mathrm{rf}}) = \int_{z_1}^{z_0} dz \left[\frac{m}{2|E_0 - qV(z) - \mu(\nu_{\mathrm{rf}} \cdot B(z)|}\right]^{1/2}. \tag{3.36}$$

Slight deviations from the ideal conditions for full conversion can cause a reduction in the measurement signal, but does not affect the position of the resonance at $\omega_{\mathrm{rf}} = \omega_c$.

An approximation of the line width of the resonance curve (see [84] for details) is found to be

$$\Delta\nu(\mathrm{FWHM}) \approx \frac{0.8}{T_{\mathrm{rf}}}. \tag{3.37}$$

Thus, the longer the excitation time, the more narrow the line profile and the more precise the measurement. Once the TOF spectrum is fit to extract the cyclotron frequency, the mass can be determined using the procedure discussed in Chapter 5.

3.2.2 Other excitation schemes

In high-precision mass spectrometry of short-lived nuclei using Penning traps the quadrupole excitation of the ion plays the most prominent role. Nevertheless, other excitation schemes are employed to manipulate the trapped ions. For example a dipole excitation can be used in a measurement cycle to reduce the number of contaminant ions in the trap, which in turn reduces ion-ion interaction which can shift the measured frequency. To accomplish this, a dipole RF field with frequency $\omega_{\mathrm{rf}} = \omega_+$ (corresponding to the reduced cyclotron frequency of the contaminant ion) and a phase difference of 180° is applied between two opposite segments of the guard electrode (see Figure 3.4(a)). The application of a dipole excitation at the reduced cyclotron frequency ω_+ of the contaminants in the radial plane results in the enlargement of their cyclotron radii. The contaminant ions are either moved

to a volume where they do not interact with the radioactive ions of interest, or driven to the electrode walls. In case the contaminant ions will not clear the trap aperture during extraction. Thus, the ions of interest remain and the sample is 'dipole cleaned' – prepared in an isobarically pure form.

Dipole excitation is a good approach when the contaminant frequencies are clearly identified. However, if there are too many and/ or unidentified contaminants present, other separation techniques such as mass-selective buffer-gas cooling [85,86] or the Stored Waveform Inverse Fourier Transform (SWIFT) [87] ion excitation method are more suitable. Development of the latter is currently underway at TITAN.

Other excitation techniques like Ramsey-excitation schemes have been implemented in the TITAN MPET. A theoretical description of the Ramsey method in TOF-ICR can be found in [81, 88]. The Ramsey method is a variation of the quadrupole excitation scheme discussed in Section 3.2.1. The RF field is typically applied in two well defined pulses which are separated by a waiting time of no excitation, instead of applying a field continuously for T_{rf}. For precision experiments the advantage is a reduction in the line width of the resonance which leads to a gain in experimental precision. A more detailed description of this scheme as used at TITAN can be found in [89, 90]. Strongly enhanced side lobes are also a feature of this technique, which makes them indistinguishable from the main maximum at $\nu_{\mathrm{rf}} - \nu_c = 0$. Therefore, in practice one has to first identify the main maxima using a 'normal' quadrupole excitation scheme.

Additional excitation schemes, such as octupole excitation, are developed and implemented at other Penning-trap mass-spectrometry facilities (e.g. [91–93]).

3.3 Achievable measurement precision

From Equation (3.37) it can be seen that the width of the TOF resonance is inversely proportional to the RF excitation time T_{rf}. The mass resolving power $\mathcal{R}$ can be formulated to be

$$\frac{1}{\mathcal{R}} = \frac{\Delta m}{m} = \frac{\Delta \nu_c}{\nu_c} \propto \frac{1}{\nu_c T_{\mathrm{rf}}}. \tag{3.38}$$

With the expression for the cyclotron frequency $\nu_c = qB/(2\pi \cdot m)$, one attains the following expression for the resolving power:

$$\frac{1}{\mathcal{R}} \propto \frac{m}{qBT_{\mathrm{rf}}}. \tag{3.39}$$

By increasing the number of ions N_{ions} recorded in a single resonance, the statistical precision $\delta m/m$ can be improved, thus

$$\frac{\delta m}{m} \propto \frac{1}{\mathcal{R} \cdot \sqrt{N_{\text{ions}}}} \propto \frac{m}{q \cdot B \cdot T_{\text{rf}} \cdot \sqrt{N_{\text{ions}}}}. \tag{3.40}$$

The proportionality constant for this expression can be seen as a quality factor of the resonance, and is a trap- and tune-dependent parameter.

From Equation (3.40) it follows that the precision of a mass measurement can be improved by an increase of the variables in the denominator. The magnetic field B could be increased, but the magnetic-field strength is limited by available technology and the achievable homogeneity. LEBIT at NSCL/MSU [94] has currently the strongest magnet of all on-line high-precision Penning-trap mass spectrometers with 9.4 Tesla. The excitation time T_{rf} is limited by the typically short half-lives of the measured ions, and N_{ion} cannot be greatly increased due to the limited availability of radioactive beamtime. Since N_{ion} enters in the equation as $\sqrt{N_{\text{ion}}}$, a gain of a factor of 10 would mean a factor of 100 more beamtime which is unrealistic.

TITAN takes advantage of the last parameter, q, to boost the precision of the mass measurement, which scales linearly with the charge state. Additional benefits of charge breeding include the resolution of low-lying nuclear isomers in Penning traps [95] and of mass doublets due to the increase in resolving power, and the integrated measurement time can also be reduced due to the use of HCI as shown in Chapter 5. For radioactive ions with low yields, the use of high charge states allow for a decrease in the total number of measured ions while still maintaining high precision.

In order to assess the benefits of charge breeding, additional aspects have to be considered. For example, the charge breeding process is accompanied by loss mechanisms resulting from ion transport, capture, storage, and extraction. Furthermore, the ions are distributed over several charge states, and the additional time delay increases losses due to decay. Additionally, the probability of charge exchange with residual gas during the excitation in the Penning trap becomes higher for HCI. Ultimately, the usage of the charge breeder lowers the overall system efficiency significantly.

Another disadvantage of charge breeding is the large energy spread in the ions extracted from the EBIT. As only a single ion is trapped in the MPET, the mass measurement is highly sensitive to variations in the initial ion energy. In addition, the large trapping region of the EBIT allows only the extraction of short ion pulses ($\approx$ 800 ns) to be transfered to MPET. To minimize the ions' energy range (as well as to boost efficiency) cooling is required. Unfortunately, buffer-gas cooling is not an option (see Section 6.2) due to charge exchange between the HCI and the neutral buffer gas. One

requires a different technique to prepare the ions for a mass measurement of HCI in the MPET. The CPET, which has been designed as part of this thesis, will be the tool of choice. This preparation trap will increase the precision of mass measurements of HCI by cooling the ions with low-energy electrons or protons and confining a full EBIT pulse in a smaller volume prior to injection into the MPET. CPET will solve the problem of the large energy spread of ions coming out of the EBIT and thus increase the efficiency of the mass measurements.

Chapter 4

Experimental Setup

TRIUMF's Ion Trap for Atomic and Nuclear science (TITAN) [20, 96] is a multi ion-trap system coupled to the radioactive beam facility Isotope Separator and ACcelerator (ISAC) [97] at TRIUMF. TITAN is dedicated to high-precision experiments on short-lived radioactive isotopes and is situated in the low-energy section of ISAC (see Figure 4.1). To perform high-precision mass measurements a preparation of the ions through several processes is required. This chapter first covers the ion beam production and delivery by ISAC, especially of the neutron-rich Rb and Sr isotopes relevant for this thesis. The beam preparation devices at TITAN are described and the mass determination using the precision Penning trap is explained.

4.1 Radioactive isotope production

Radioactive Ion Beam (RIB) facilities [98] play an important role in pushing the frontiers of knowledge in nuclear physics and many other fields. Various techniques are established to produce beams of short-lived radioactive nuclei. Most RIB facilities can be classified into two popular families depending on the production techniques: 'in-flight' facilities and Isotope Separator On-Line (ISOL) facilities [98].

The 'in-flight' technique uses fragmentation of fast, intense, heavy-ion beams on a target of light nuclides. Here the forward momentum of the primary beam fragments is exploited for mass separation or further reactions. Some facilities associated with this technique are GANIL (Cean, France), GSI (Darmstadt, Germany), NSCL (East Lansing, USA), and RIKEN (Tokyo, Japan). The spallation, fission, and fragmentation of light ion beams on a target of heavy nuclides, or the fusion process to produce superheavy elements are a different form of the 'In-flight' technique.

Figure 4.1: ISAC experimental halls at TRIUMF. The experimental areas are distinguished by their respective beam energy. TITAN is situated on a platform in the low-energy area of ISAC I.

The second technique is known as Isotope Separator On-Line (ISOL) and is implemented at TRIUMF. The ISOL-method requires a high-intensity primary beam of light particles from an accelerator and a thick target, from which the formed exotic nuclei have to diffuse out and into an ion source for ionization and extraction. Besides ISAC at TRIUMF (Vancouver, Canada) other facilities using this production technique include ISOLDE at CERN (Geneva, Switzerland) and HRIBF (Oak Ridge, USA).

4.1.1 Neutron-rich Rb- and Sr-beams at ISAC

TRIUMF employs the ISOL techniques for radioactive isotope production. The driver beam is provided by TRIUMF's cyclotron which accelerates H^- to 500 MeV. When passing through stripper foils a fraction of the H^- bunch gets converted into H^+ and can be extracted. A H^+/ proton beam of up to 100 μA is produced and delivered to ISAC (see Figure 4.1), which currently represents the highest proton beam intensity for an on-line ISOL facility. Next the beam impinges on a production target. The products from this bombardment diffuse out of the target and are ionized. The target gets heated both by the proton beam itself and by resistive heating for faster diffusion of the products. At ISAC several ion sources are available including a surface ion source, a laser ion source, and a Forced Electron Beam Induced Arc Discharge (FEBIAD) ion source. Described by the Langmuir-Saha surface ionization theory (its application can be seen in e.g. [99, 100]), elements with an ionization potential I_p lower than the work function Φ of the surface, e.g. tungsten with $\Phi = 4.6$ eV, can be efficiently ionized. Hence, a surface ion source is well suited for alkali elements such as the Rb isotopes ($I_p = 4.2$ eV) studied here, but noble gases are not accessible as they have higher ionization potentials. The alkaline Sr isotopes with $I_p = 5.7$ eV are ionized as well, although at a lower ionization efficiency. Apart from the dependency on the ionization potential, the process is not selective in the ionization of elements [101].

A schematic of the beam production, ionization, and separation of radioactive beams at ISAC can be seen in Figure 4.2. The newly formed ions are electrostaticly accelerated up to 60 keV of beam energy. They pass through a two-stage dipole magnet mass separator unit (pre- and main separator) which selects ions based on their mass-to-charge ratio. Nuclides with different mass numbers are easily separated due to the large mass differences. However, different elements with the same mass number (i.e. isobars) are often too similar in mass to be resolved by the mass separator, which has an achievable resolving power $\mathcal{R}$ on the order of $\mathcal{R} = m/\Delta m \approx 3000$. Isobaric contamination in the beam delivered to the experiment has to be expected

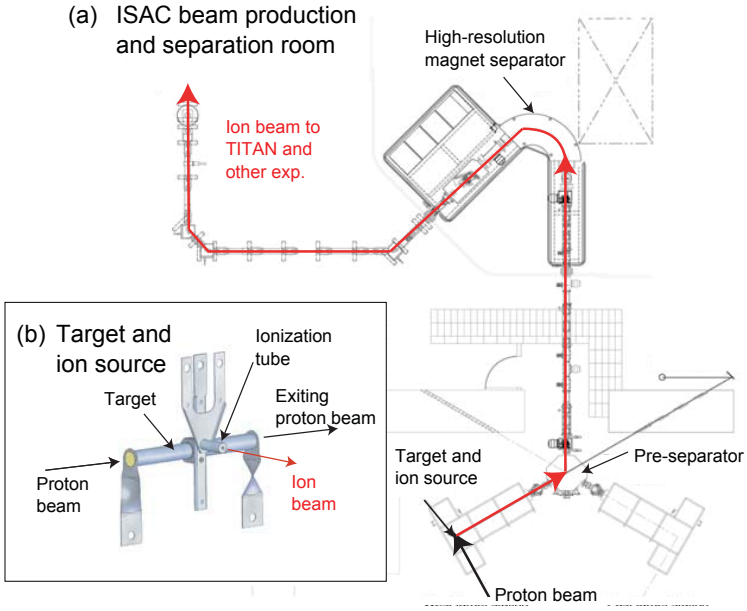

Figure 4.2: (a) Schematics of beam production, ionization, and separation of radioactive beams at ISAC with (b) target and ion source setup. Figures from [102].

for close lying isobars. For experiments such as the mass measurements at TITAN a contaminant-free beam of the nuclide of interest is required, as contamination will affect the measurement result. Therefore, different 'cleaning' techniques need to be employed (see Section 3.2.2).

Different targets produce different radioactive nuclides. Figures 4.3 (a) and 4.3 (b) compare the yields for various targets for Rb and Sr isotopes, including those studied in this thesis. Since none of the commonly-used targets (e.g. Nb, Ta, and ZrC) allow yields of very neutron-rich Rb and Sr isotopes TRIUMF used a UC_x target for the very first time in December 2010. For many years UC_x targets have been used at ISOLDE [104]. Owing to the large excess of neutrons, uranium targets are particularly well suited for producing beams of neutron-rich nuclides. Due to restrictions on TRIUMF's nuclear operations license, the ISAC UC_x target was only irradiated with a 2 μA proton beam, which is a factor of 10-50 less than for all other targets. The measurements performed for this thesis were taken during the first operation of the UC_x target. Since then, the license was extended to 10 μA (see ISAC yield database [103]). A graph combining the relevant measured Rb and Sr yields is shown in Figure 4.4.

The resolving power $\mathcal{R}$ needed to separate isobaric Sr from Rb and vice

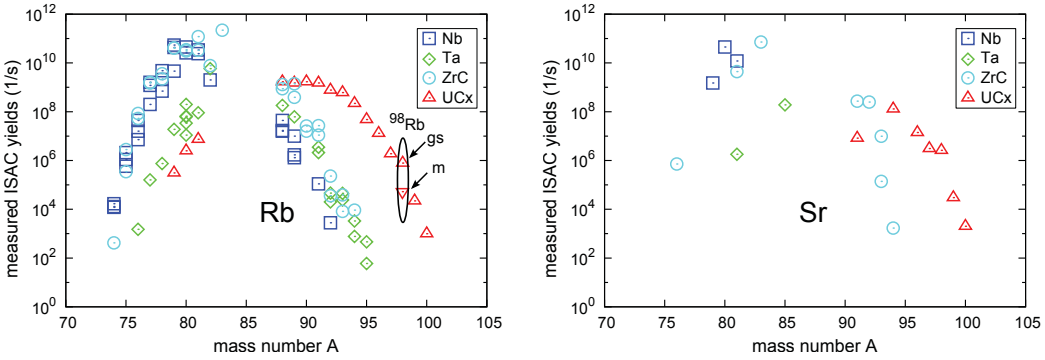

Figure 4.3: Measured yields of Rb and Sr isotopes at ISAC for various targets. Plotted are absolute numbers which are not normalized to the respective beam currents for different targets. Data is taken from ISAC yield database [103].

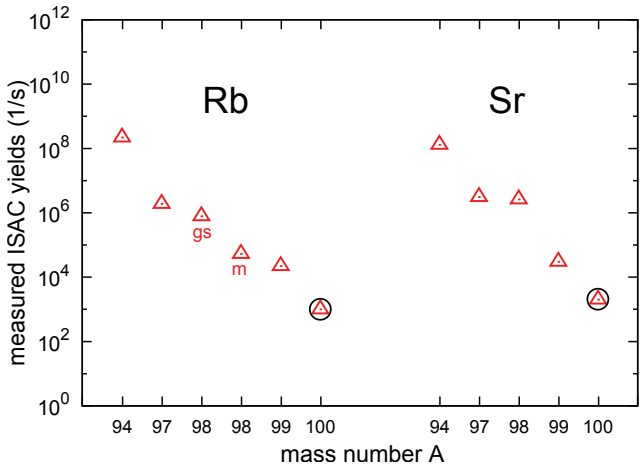

Figure 4.4: Measured yields of Rb and Sr isotopes relevant for this thesis. A UC_x target was used which was irradiated with a 2 μA proton beam. The data points enclosed by a circle indicate isotopes where no mass measurement has been performed. Data is taken from ISAC yield database [103].

Table 4.1: The resolving power $\mathcal{R} = m/\Delta m$ that is needed to separate isobaric Sr from Rb and vice versa for the isotopes measured.

mass number A	$\mathcal{R}$
94	8,518
97	8,974
98	7,474
99	7,919
$^{98}\mathrm{Rb}^{gs}$ vs. $^{98}\mathrm{Rb}^{m}$	322,197

versa, as can be seen in Table 4.1, is beyond the capabilities of the ISAC mass separator. However, it is possible to fine tune the magnets of the mass separator to a more favorable ratio between contaminant and beam of interest. Contamination was an important factor to consider for the mass measurements of ^{94,97,98}Rb and ^{94,97,98,99}Sr. In addition to fine tuning of the mass separator, isobaric cleaning with ion-trap techniques at TITAN was required (see Sections 3.2.2 and 5.2).

4.2 The TITAN facility

For the measurements described in this thesis, the ion beam was generated at ISAC using a surface-ionization source and extracted at 20 keV, transported through the ISAC mass separator and delivered to the TITAN facility. TITAN, shown schematically in Figure 4.5 presently consists of three traps: a buffer-gas-filled radio-frequency quadrupole (RFQ) trap [105] for cooling and bunching, an electron-beam ion trap (EBIT) [106] for charge breeding, and a hyperbolic Penning trap (MPET) for mass measurements on short-lived nuclei with a precision of up to $\delta m/m \approx 10^{-8}$ [107].

4.2.1 The radio-frequency quadrupole trap

RFQs are used in several RIB facilities [1, 108, 109], primarily for applications related to mass measurements but also for collinear laser spectroscopy [110–112]. At TRIUMF, ion beams generated in ISAC are delivered to TITAN at energies up to 60 keV with an energy spread of tens of eV [105]. However, Penning-trap mass measurements require an ion beam with specific properties. First, the typical ion kinetic energy can only be a few eV [79].

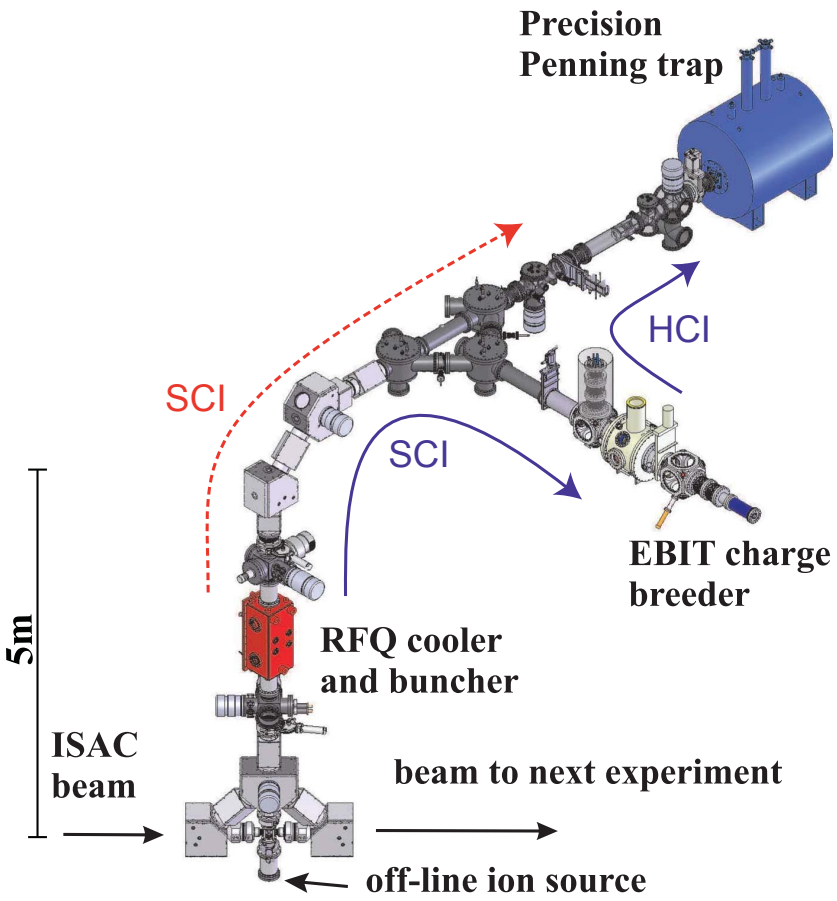

Figure 4.5: The TITAN facility for high-precision atomic mass measurements is presently composed of three ion traps. The singly charged ion (SCI) beam from ISAC passes through a radio-frequency quadrupole (RFQ) where the ions are thermalized in a helium buffer gas, bunched, and then sent straight to the precision Penning trap for mass measurements (MPET), indicated by the dashed red arrow. With solid blue arrows the pathway for a mass measurement of highly charged ions (HCI) is shown. The SCI from ISAC are sent through the RFQ to the electron-beam ion trap (EBIT), charge-bred, and transported to MPET.

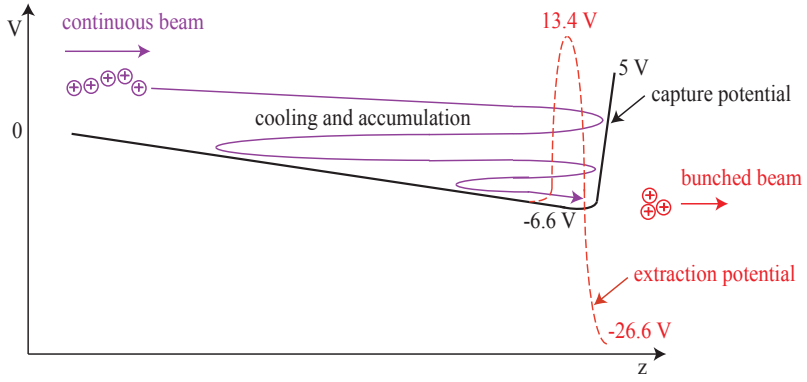

Figure 4.6: Schematic of a typical applied electrostatic potential of the RFQ. The DC field moves the cooled ions to the potential minimum. During the extraction process the potential switches from the solid black to the dashed red line. Figure from [102].

Second, the energy spread must be small, on the order of 1 eV or less, and the phase space and emittance need to be reduced. Finally, the continuous ISAC beam needs to be bunched for injection into the MPET. The TITAN RFQ is used to cool and bunch the beam of SCI to match these criteria [105, 113].

In order to accumulate and bunch the radioactive beam the RFQ is biased a few eV below the beam energy. Deceleration optics forming an electrostatic azimuthal quadrupole potential [105] are used to inject the beam into the RFQ. The RFQ is designed for beam energies between $12 - 60$ keV, with a transverse acceptance of 50 πmm mrad or less. The ions are cooled through collisions with a room-temperature buffer gas. A linear Paul trap is used to confine the ions radially during the collisional cooling process. The ions are trapped longitudinally by an electrostatic potential that can be seen in Figure 4.6.

4.2.2 The electron beam ion trap

The TITAN EBIT [106, 114] was designed and built in collaboration with the Max-Planck-Institute for Nuclear Physics (MPIK) in Heidelberg and brought to TRIUMF in 2006. The main purpose of the TITAN EBIT is fast charge breeding of the singly charged rare isotopes using electron impact ionization in order to boost the precision of the subsequent mass measurement. The charge-breeding process needs to be fast and efficient to match the short half-lives and limited yields typical for radioactive ion beams. The EBIT was designed to attain high charge states on time scales comparable to the

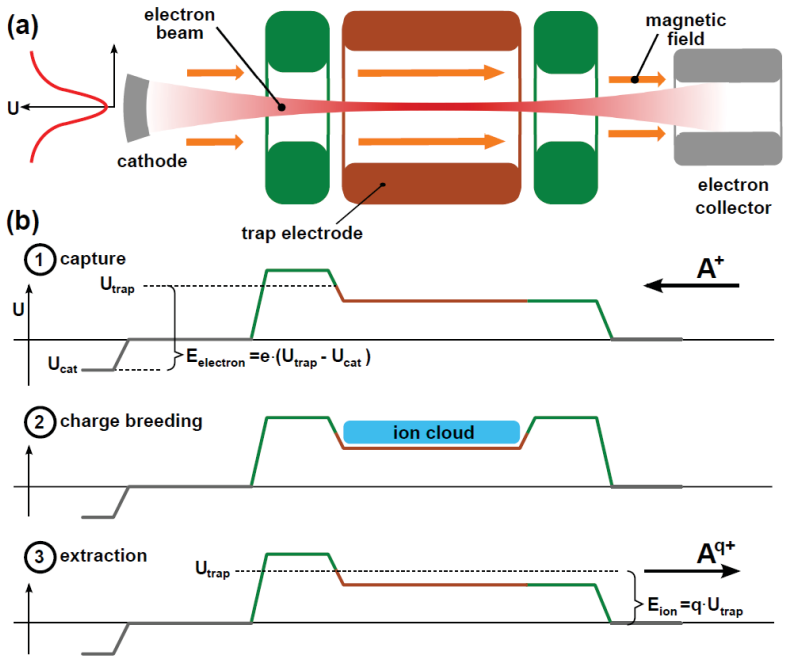

Figure 4.7: (a) Schematic of the EBIT and (b) the injection, charge breeding, and extraction potentials. Figure from [90].

nuclide's half-life while maintaining an efficiency of extracted charge-bred ions in one certain charge state of a few percent. In the TITAN EBIT (Figure 4.7(a)) the ions are confined axially by an electrostatic potential applied to the EBIT trap electrodes and radially by the combination of an intense, high-current electron beam (space charge) and a strong magnetic field of up to 6 T. Figure 4.7(b) displays the injection, charge breeding, and extraction scheme of the EBIT as it was used for the measurements in this thesis (see Chapter 5). The singly charged ions from the RFQ are injected into the EBIT, which is floating to a potential U_{trap} slightly below the incoming beam energy. The beam is captured by switching the neighboring drift tubes to a higher voltage to establish an axial trapping potential. The electron beam is continuously on, and its energy is defined by the difference between U_{trap} and the bias voltage of the electron cathode U_{cat}, that is $E = e(U_{\mathrm{trap}} - U_{\mathrm{cat}})$. Typical breeding times range from 20 ms to 200 ms and are adjusted depending on the half-life of the nuclide and the desired charge state. Once this charge state is maximized relative to the charge breeding distribution (for example see Figure 4.9), the beam is extracted from the injection side of the trap. Due to the higher charge state q the total kinetic

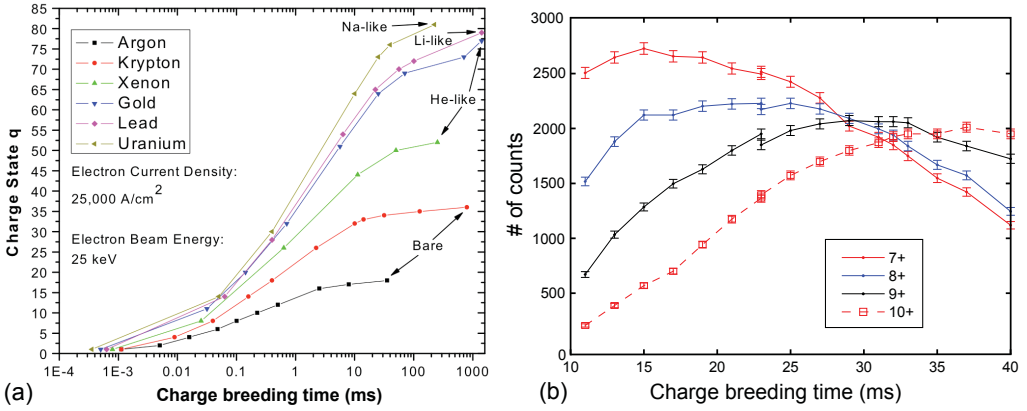

Figure 4.8: (a) Simulation of breeding times in the EBIT to reach a certain charge state for various elements. Figure from [115]. (b) Measured number of ^{85}Rb-ions in various charge states for different charge breeding times in the EBIT with a 2.5 keV and 10 mA electron beam. The number of counts corresponds to the sum of 200 extractions from the EBIT.

energy of the HCI is increased to $E_{\text{ion}} = qU_{\text{trap}}$ after extraction.

The EBIT is designed to operate with electron beam energies and currents of up to $\approx$ 70 keV and 500 mA (upgradeable to 5 A), respectively. Experimentally, currents and energies of 400 mA at 7 keV and 200 mA at 25 keV have been demonstrated [106].

Simulations of the charge breeding in the EBIT [115] show how rapidly the charge-breeding process (see Figure 4.8(a)) occurs. In particular, high charge states of $q = 20+$ can be reached within tens of milliseconds, which is suitable for short-lived nuclides such as ^{98}Rb, $T_{1/2} = 114$ ms.

The relative abundances of the charge states for stable Rb were measured via their time of flight to a microchannel plate (MCP) detector, and the results are displayed in Figure 4.8(b). In general, for longer breeding time higher charge states are favored over lower ones. These data were used to determine appropriate EBIT settings and charge breeding times used for this experiment, and will be discussed in Chapter 5.

Figure 4.9 displays the charg-state distribution for ^{85}Rb with a charge breeding time of 197 ms, and a 10 mA, 2.5 keV electron beam. Due to the presence of residual charge-bred gas in the charge states $q = 16 - 19+$, a contaminant-free charge state was selected, i.e. ^{85}Rb^{13+}. Neutron-rich Rb isotopes with a similar mass-number-to-charge-state ratio $A/q \approx 6.5$ (i.e. ^{98}Rb^{15+}) were selected for the mass measurement. Charge breeding times were reduced to 80 ms due to the short half-lives of the nuclides involved in

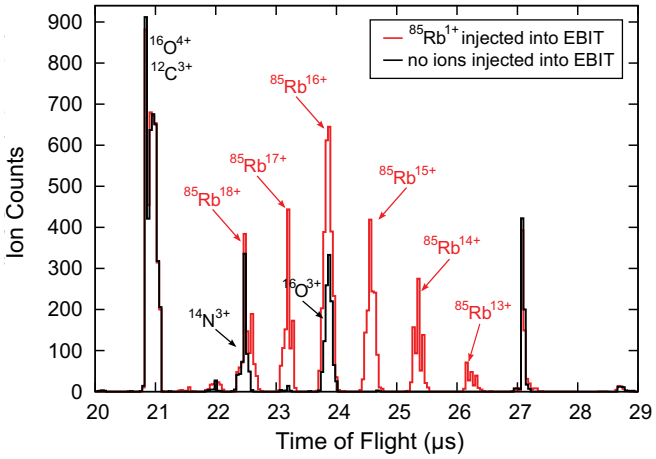

Figure 4.9: Time-of-flight spectrum of 500 ion bunches of ^{85}Rb extracted from the EBIT. Ions were extracted for 800 ns after 197 ms of charge breeding with a 10 mA/ 2.5 keV electron beam. Peaks due to the ionization of residual gas (black) can be seen as well.

the on-line mass measurements.

4.2.3 Beam transport and charge-state selection

The beamline connecting the RFQ with the EBIT and the MPET is designed to allow for efficient transmission of ions. The kinetic energy of bunched beams in the TITAN beamline typically ranges between $1-2$ keV (designed for up to 5 keV). In this section a few of the key beamline elements essential for a high-precision mass measurement are discussed. The beam transport includes many electrostatic optical elements, including steering in x- and y-directions, quadrupole multiplets, and Einzel lenses for focusing, and diagnostic tools.

RFQ to EBIT: Upon extraction of the ion bunch from the RFQ, the beam is accelerated into a Pulsed Drift Tube (PDT) [105]. It works as an 'elevator', which transfers the beam from the high voltage RFQ (U_{RFQ}) section to the beamline at ground potential. The PDT is initially biased to $\Delta V = 1-2$ kV below the RFQ potential, that is $U_{\mathrm{pot}} = U_{\mathrm{RFQ}} - \Delta V$. The ion bunch is accelerated into the tube which is switched quickly to ground potential when the ions are inside. The ion bunch is unaffected by the fast switching and is transported with kinetic energy $e\Delta V$ to the EBIT. For the measurement in Chapter 5 the kinetic energy (i.e. the beamline transport energy) was set

to ≈ 2 keV. The ion bunch is transferred through a series of optics to the EBIT which is floating at a ≈ 2 kV potential. The singly charged ions from the RFQ decelerate when injected into the EBIT and are electrostatically retarded by the potential applied to the center electrode.

EBIT to MPET: After charge breeding in the EBIT, highly charged ions are extracted towards the MPET by applying a fast switching potential, and are accelerated to a kinetic energy of 2 keV·q. They pass through a series of optics including benders, lenses, steerers and a time-of-flight gate. When extracting a short pulse of charge-bred ions from the EBIT onto a microchannel plate detector (MCP) as seen in Figure 4.9, one sees many different charge states separated by their time of flight. As discussed in Section 4.2.2, the charge-breeding process distributes the injected ions over a range of charge states, the center of which depends on the charge-breeding time and the electron current density in the EBIT. However, a Penning-trap mass measurement is ideally performed with only a single ion species in the trap at a time, because the presence of contaminant ions can reduce the measurement signal and lead to shifts in the measured frequencies.

In order to obtain a good TOF resolving power, short pulses of ions have to be extracted out of the EBIT, and allow for the (A/q)-selection that is essential for precision mass measurements. This results in a loss of efficiency as only a fraction of the total ions in the EBIT can be extracted from the comparatively long trapping region. This will be resolved with the implementation of the new Cooler Penning trap (CPET) system, which will be discussed in detail in Chapters 6 and 7.

Until recently, fast-switching steerer plates were used as a time-of-flight gate to steer ions with unwanted A/q. The minimum achievable gate width of this setup was ≈ 1.2 μs. For HCI the spacing of different A/q in TOF over a similar range is much smaller, and the time window mentioned does not discriminate against the background any more.

For faster TOF selection a Bradbury Nielsen ion gate (BNG) was developed and tested at TITAN [116]. A BNG consists of two sets of small, interleaved parallel wires arranged in a plane perpendicular to the propagation of the ions. Two operational modes are employed. First, when the two sets of wires are biased to a different voltage, the ions are steered off axis. Second, when there is no (or the same) voltage applied, the ion bunch can pass through the gate. The gate has a smaller capacitance than kicker plates, and the spatial dimensions of the gate along the beam axis and thus the disturbance of the ions flight path is greatly reduced for BNG compared to kicker plates [116]. The geometry allows for fast switching times of ≈ 50 ns. The

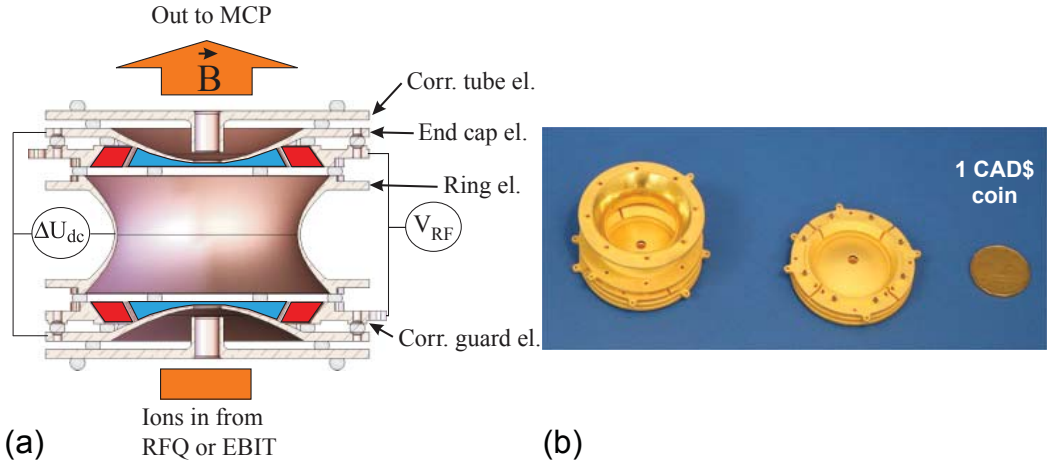

Figure 4.10: (a) Schematics and (b) picture of the MPET electrodes with a Canadian dollar coin (diameter of 26.5 mm) for scale. Figures from [102].

typical width of the TOF peaks is longer, making the BNG well suited for the time-of-flight selection of a certain charge state for Penning-trap mass measurements and used in this thesis.

Prior to the capturing of the ions in the MPET, there are two additional units of ion optic elements, both located in the fringe field of the magnet: a Lorentz steerer [117] and a pulsed drift tube (PDT). The Lorentz steerer is a four-fold segmented cylindrical electrode used for steering, located in the fringe magnetic field of $\approx$ 2.7 T at a distance of 26.3 cm off the trap. The $\vec{E} \times \vec{B}$ drift motion leads to a radial displacement of the ion bunch, thus preparing them on an initial magnetron radius before injection into the MPET. The ions then enter the PDT, which is initially biased to a voltage close to the transport energy of the ions. The ions lose most of their kinetic energy as they enter the PDT, which is then pulsed down to a negative voltage, and the ions lose their remaining kinetic energy towards the trap center, which is on ground potential.

4.2.4 The measurement Penning trap

The measurement Penning trap (MPET) is used for the mass measurement (see Chapter 5). The hyperbolical Penning trap, shown in Figure 4.10, is mounted in a vacuum tube inside the bore of a 3.7 T magnet. Its characteristic trap dimension is $d_0 \approx 11.21$ mm [79].

Deviations from the harmonic potential of an ideal Penning trap, as well as higher order anharmonicities, arise due to the presence of holes for in-

Table 4.2: Frequencies of an ion of mass $A = 98$ and charge $q = 15+$ in TITAN's MPET with $B = 3.7$ T and a trapping potential of $U = 35.75$ V.

Motion	Frequency
ν_c	8.700 MHz
ν_+	8.694 MHz
ν_-	6.110 kHz
ν_z	325.9 kHz

jection and extraction in each end-cap electrode as well as the finite size of the electrodes. To correct for these imperfections correction-tube electrodes are placed next to the entrance and exit holes in the end-caps (see Figure 4.10(a)). Additionally, correction guard electrodes are inserted into the gap between the ring and end-cap electrodes. Using these correction electrodes, a trap compensation procedure as described in [79, 102] is performed to obtain the potential closest to the ideal case.

For the present measurements, a trapping potential between the end-cap and ring electrodes of $U = 35.75$ V was used. Nominal frequencies for an ion with $A^{q+} = 98^{15+}$ are listed in Table 4.2. The azimuthal (i.e. dipole and quadrupole) RF fields (see Figure 3.4) are most commonly applied to segments of the ring electrode. However, in the TITAN setup the guard electrodes are segmented while the ring electrode is left as one piece, in order to avoid distortions in the harmonic field due to the splitting of the ring electrode. This improvement requires larger RF amplitudes to reach equal field strengths at the position of the ions, which faciliates the need for RF amplifiers. In comparison to the conventional method (segmented ring electrode) larger RF amplitudes are required to reach the same field strength in the trap center. As a consequence, RF amplifiers are employed at MPET.

Chapter 5

Mass Measurements in the Vicinity of A≈100

This chapter presents mass measurements performed on Rb and Sr isotopes in the vicinity of A≈100 using the TITAN facility (see Chapter 4). Isotopes in this region have an impact on the mass surface. In addition a reduced uncertainty on the mass values helps to increase knowledge of the r-process. This work contains accurate and precise mass measurements of highly charged ions in the charge state $q = 15+$. This represents the first time that on-line produced isotopes were measured in a Penning trap reaching such a high charge state.

The synthesis of about half of the heavy elements beyond germanium, $Z = 32$, proceeds in nature via the r-process [17]. A more detailed description is given in Section 2.2. In the most common r-process models the neutron capture reactions proceed until an equilibrium between neutron capture and photo disintegration, (n,γ) $\rightleftharpoons$ (γ,n), is established, driving the r-process path to nuclei with neutron separation energies of approximately 2 to 3 MeV [118]. The r-process of heavy elements plays an important role in our understanding of stellar processes.

Testing predictions of r-process models against abundance observations requires an understanding of nuclear physics properties with respect to the evolution of astrophysical conditions to produce a characteristic abundance pattern. Nuclear input data of importance to r-process models are nuclear masses, β-decay half-lives, and neutron capture cross sections [49]. Fission rates and fission fragment distributions, neutrino interaction rates, and charged-particle fusion rates also play a role, however a relatively minor one [49].

In models characterized by an (n,γ) $\rightleftharpoons$ (γ,n) equilibrium, the reaction path for a given set of astrophysical conditions is governed by nuclear masses.

However, many of the nuclei in the r-process, as detailed in Chapter 2, are experimentally inaccessible because of their location far away from the valley of stability. Hence, nuclear astrophysics modeling relies heavily on theoretical mass predictions, which are performed by models with parameters adjusted to known masses [2]. Experimental mass data on neutron-rich nuclei are therefore needed not only as direct input into r-process model calculations, and also to improve mass models and to reduce the uncertainty in extrapolations. Fig. 5.1 shows the reaction flows of the parameterized, fully dynamical r-process model that is used in this work. The model follows Freiburghaus *et al.* [64] and Hosmer *et al.* [119] and is based on an adiabatic expansion assumed to be encountered in high-entropy neutrino-driven winds in core collapse supernovae. The path is characterized by a complex network of charged-particle- and neutron-induced reactions and their inverse reactions. More details can be found later in Section 5.5. The model passes through the mass region covered by the experiments in this thesis ($A \approx 100$), which help to reduce the challenge for theoretical mass models.

Additional motivation for this work stems from the desire to understand better the nuclear structure, in particular shell closure effects at $N = 50$, the subshell closure at $N = 54$, and a possible onset of large deformation for nuclei with $N \geq 60$ [40]. These in turn will also help to provide better predictions for unknown nuclear masses, as described in Section 2.1.1. Several theoretical investigations of the nuclear structure in the $N \approx 60$ region have been carried out ([13–15] and references therein). Within a self-consistent Hartree-Fock-Bogoliubov (HFB) formalism [14], the nearly-spherical shape for $N < 59$ in Sr, Zr, and Mo isotopes is predicted to develop into a strongly deformed prolate shape above $N > 60$. In the so-called D1S-Gogny energy-density-functional framework ([15] and references therein), in which one-quasiparticle configurations are employed, a self-consistent mean-field approximation indicates nuclear deformation and shape co-existence. These calculations predict a sharp oblate-to-prolate transition in the Rb, Sr, and Zr isotopes and triaxiality in the Mo isotopes.

Empirical evidence supports rapidly changing behavior in $N \approx 60$ nuclei [5–11]. An onset of deformation, seen as a change in the slope of the two-neutron separation energy, S_{2n}, has already been observed in the Rb isotopes [12] and in the Sr and Zr isotopic chains around $N \approx 60$ [5]; however, neutron-rich Kr isotopes do not present any nuclear quantum phase transition [10]. In this work, the investigation of nuclear deformation around $N \approx 60$ to neutron-rich Rb and Sr isotopes is extended via Penning-trap mass spectrometry.

Previous Penning-trap mass measurements in this region [5,6] differ from the Atomic-Mass Evaluation (AME03) [28] by up to 300 keV and up to 11σ.

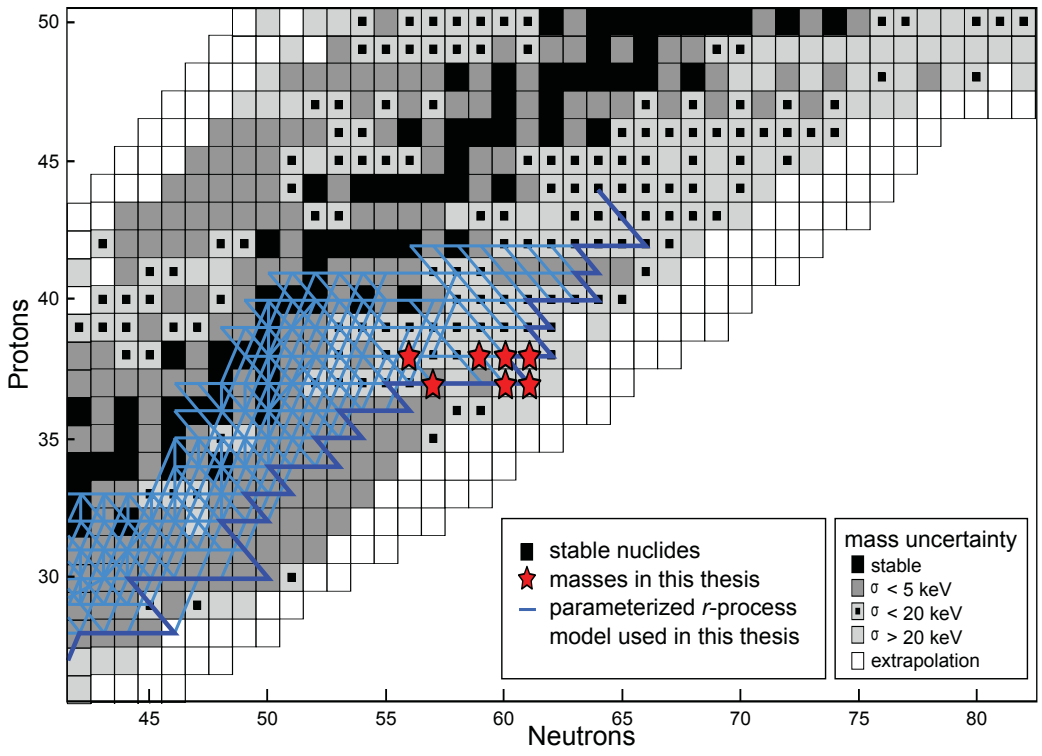

Figure 5.1: Section of the chart of nuclides. The neutron-rich nuclei studied in this work are indicated by red stars. The mass uncertainty is displayed as well as the calculated time-integrated net-reaction-flows for a single $S = 100$ component (blue) of the parameterized, high-entropy wind inspired, r-process model used in this work. Flows above a relative final abundance of 10^{-5} are denoted by light blue lines indicating the complex interplay of charged-particle-and neutron-induced reactions in this mass region; dark blue lines mark the outer boundary of the reaction flows for clarity.

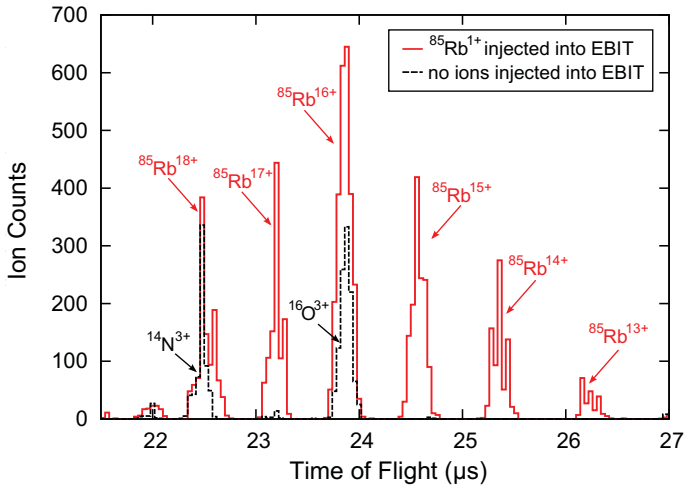

Figure 5.2: Time-of-flight spectra of charge-bred ions extracted from the EBIT. A charge-breeding time of 197 ms, a magnetic field of 3 T, an electron beam current of 30 mA, and an extraction time of 800 ns were applied to obtain this spectra. The data represents 500 ion bunches. The red line shows the charge breeding of $^{85}Rb^{1+}$ in the EBIT. The black spectrum represents background gas in the EBIT.

Therefore, an independent confirmation was desired to verify this discrepancy and to even increase the precision. To that end, precise and accurate mass measurements on radioactive, short-lived isotopes have been performed at TITAN [20, 96] at the radioactive beam facility ISAC [97]. The integrated measurement time could be reduced compared to singly charged ions due to the high charge states used for the mass measurement. The experimental time for measuring the seven masses was ≈40 hours and the charge-breeding capability was improved to be able to measure highly charged ions in charge states up to $q = 15+$.

5.1 Experimental parameters

The complete TITAN setup (see Section 4.2 for a more detailed description) was used for these measurements. The ions were first cooled and bunched in the RFQ, and then sent to the EBIT for charge breeding (see Fig. 4.5). The ions were charge-bred for T_{breed} ≈80 ms using an electron beam current and energy of 30 mA and 2.5 keV respectively. Then the ions were extracted by opening the trap barrier for 800 ns, generating a short ion pulse. This led

to a sharp time separation of ions in various charge states or with different m/q (see Fig. 5.2) and allowed for the selection of ions with a certain (m/q)-ratio using a Bradbury-Nielsen ion gate [105]. A distribution of charge-bred ^{85}Rb ions extracted from the EBIT is shown in Fig. 5.2. In this case a charge-breeding time of 197 ms was used. More details and description of the charge-breeding process and extraction out of the EBIT can be found in Sections 4.2.2 and 4.2.3. The ions of the charge state with the greatest ratio of ion of interest to background was sent to the MPET to determine the ion's mass using the time-of-flight ion cyclotron resonance (TOF-ICR) method [83, 84]. For a detailed description of this method see Section 3.2.1. In the MPET the ions were excited for 20 ms using dipole excitation followed by 77 ms of quadrupole excitation before extracted out of the trap onto a microchannel plate detector.

5.2 Data analysis and systematic uncertainties

As discussed in Chapter 3.1 and Section 3.2 the main observable in Penning-trap mass spectrometry is the cyclotron frequency $\nu_c = qB/(2\pi \cdot m)$. The charge state q is derived from a time-of-flight spectrum at a detector prior to the MPET, but the magnetic-field strength B needs to be measured to determine the ionic mass m. From a fit of the theoretical line shape [84] to the resonance data (see Figures 5.4 and 5.5), the mass can be extracted from Equation (5.2) if q and B are known. To minimize systematic effects and to calibrate the magnetic field, a reference measurement of an ion with charge q_{ref} and a well-known mass m_{ref} is performed before and after the actual measurement. The primary experimental result is the ratio R of the cyclotron frequency of the ion of interest to that of the reference ion $\nu_{\mathrm{c,ref}}$,

$$R = \frac{\nu_{\mathrm{c,ref}}}{\nu_{\mathrm{c}}} = \frac{q_{\mathrm{ref}} \cdot m}{q \cdot m_{\mathrm{ref}}}. \tag{5.1}$$

From which the atomic mass m_{atom} is given by:

$$m_{\mathrm{atom}} = \frac{q}{q_{\mathrm{ref}}} \cdot \overline{R} \cdot (m_{\mathrm{ref}} - q_{\mathrm{ref}} \cdot m_{\mathrm{e}} + B_{\mathrm{e,ref}}) + q \cdot m_{\mathrm{e}} - B_{\mathrm{e}}, \tag{5.2}$$

where $\overline{R}$ is the average of all measured frequency ratios, B_{e} is the total binding energy of the removed electrons (also known as the neutralization energy (e.g. [120])) of the ion of interest, and the index 'ref' refers to the reference ion.

The value for $\nu_{c,ref}$ at the time of the measurement of ν_c is obtained by a linear interpolation of the two reference measurements that enclose the measurement of the ion of interest and assuming a linear behavior. There is a correlation introduced between adjacent frequency ratio measurements due to shared references. For the data analysis we take into account a full covariance matrix between all the ratios [121].

In Table 5.1 the frequency ratios of $^{94,97,98}Rb^{15+}$ and $^{94,97-99}Sr^{15+}$ isotopes relative to $^{85}Rb^{13+}$ are presented. The mass excess values are shown in Table 5.2. Accuracy limitations, reflected in systematic uncertainties are due to magnetic-field instabilities, uncertainty of the mass of the reference ion and electron binding energies, unresolved charge states, ion-ion interaction, m/q-effects, and isobaric contaminants. These systematic effects are discussed below.

a) Magnetic-field instabilities

A spatially-uniform and temporally stable magnetic field is required for precision measurements. The magnetic field is homogeneous in the trap region to $\delta B/B \approx 10^{-7}$ inside a 2 cm long by 1 cm diameter cylinder [79]. We minimize the effect of instabilities in the magnetic field by using a frequency ratio. As stated in [79] the uncertainty for magnetic-field instabilities is $\Delta R/R \ll 0.2$ ppb/ hour between adjacent reference measurements. In this work the time between two reference measurements was kept to less than one hour.

b) Reference atom

The uncertainty in the mass of the reference atom can be considered negligible relative to the statistical uncertainty. The reference ^{85}Rb is known with a mass uncertainty of 11 eV [122], equivalent to 0.1 ppb.

c) Electron binding energy

The total electron binding energies were taken from [123]. The total atomic binding energy (binding energy of all remaining electrons) has been calculated using a Dirac-Fock approximation and values are tabulated for lithium- to dubnium-like systems with $Z = 3 - 118$. Uncertainties for the total electron binding energies of $Rb^{13+,15+}$ and Sr^{15+} are conservatively estimated to be below 20 eV, corresponding to 0.2 ppb [124], negligible relative to the reached statistical uncertainty.

d) Unresolved charge states

Although we aimed for single-ion injection, the time-of-flight spectra of the ions detected on the microchannel plate detector after the Penning trap, see Figure 5.3, showed a multitude of m/q states. These are unresolved charge states due to charge exchange with residual background gas in the MPET. To minimize the possibility of charge exchange a low pressure in the MPET is favored. The pressure in the MPET vacuum section (see Section 4.2.4) was measured to be $\approx 5 \cdot 10^{-11}$ mbar. The third set of parenthesis in Table 5.1 represents the uncertainty associated with gating on the charge state of interest. The time-of-flight spectra of the trapped ions in the MPET showed a peak with a tail, indicating the possibility of more than one charge state in the trap. The gating on the peak, as indicated in Figure 5.3, allowed to remove all dark counts in the time-of-flight window, which are generated either by ions of interest or other ions and to cut out the last fraction of the tail of the distribution. In the analysis the time-of-flight range was varied between a worst-case scenario and an optimal gating. The differences occurring resulted in a systematic uncertainty of 0 to 14 ppb to all measured nuclides and are shown as the third set of parenthesis in Table 5.1.

In addition to the peak of $^{94}Rb^{15+}$ a second peak at ≈ 3 μs is visible, which is due to the charge exchange in the MPET between stored HCI and the residual gas. A dipole excitation at ν_+ of H_2^+ removed this peak, establishing it to be H_2^+. However, for an excitation time of $T_{\mathrm{rf}} = 97$ ms the fraction of ions which underwent charge exchange remained at an acceptable level (Figure 5.3), and the number of counts in the H_2^+ peak was only $\approx 10\%$ of all detected signals and hence can be disregarded.

e) Ion-ion interaction

To address potential shifts in ν_c due to ion-ion interaction in situations where there is more than one ion stored in the trap, a so-called count-class analysis [125] was performed: Data from a measurement run were grouped together according to the number of detected ions per spill, usually into three groups (1, 2, and 3-7 ions per spill). The resonance of each group was fitted separately to determine a cyclotron frequency. Trends in the cyclotron frequency as a function of detected ions per ion spill could be investigated and ν_c was extrapolated to the case of a single ion stored in the Penning trap. Considering the detector efficiency of the microchannel plate detector, this corresponds to $\varepsilon = 0.6 \pm 0.2$ detected ions [126]. Due to charge exchange of HCI, ions in different charge states could be present in the trap even when a contaminant-free beam had been captured in the MPET. A count-class anal-

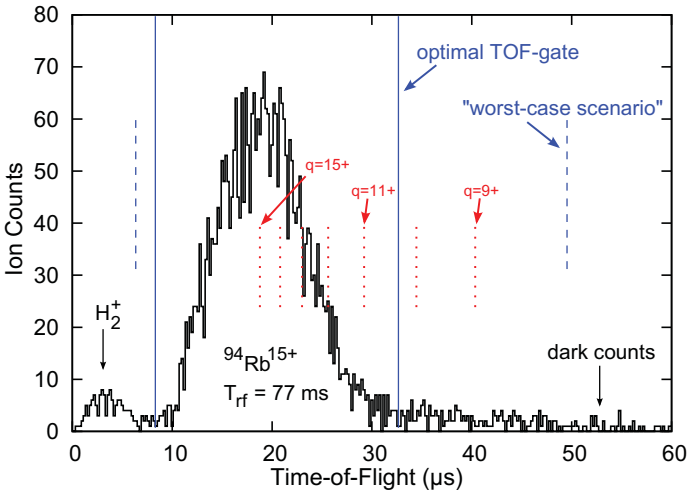

Figure 5.3: TOF histogram of detected ions after extraction from the MPET. In addition to $^{94}Rb^{15+}$, a peak corresponding to H_2^+ was observed, which was due to charge exchange in the MPET. TOF gates are indicated in blue solid and dashed lines. The position for other m/q states are marked by red doted lines.

ysis was performed, and the uncertainty was convoluted with the statistical uncertainty (see first parenthesis in Table 5.1) and varied from 0 to 3 ppb depending on the isotope.

f) Accuracy checks

Accuracy checks for HCI used in this work have been performed by measuring the cyclotron frequency of $^{85}Rb^{11+}$ vs. $^{85}Rb^{13+}$ vs. $^{85}Rb^{15+}$. Different settings (e.g. Lorentz steering [117] (see Section 4.2.3), extraction optics, etc.) as well as different timings (e.g. duty cycle, capture timings, etc.) were covered. A shift in the frequency cannot be excluded due to a possible trap misalignment, ion-ion interactions due to the increase of charge states, and relativistic mass increase. Theses effects have been studied for the TITAN system in more detail in [79]. The mass shift due to the increase of charge states scales with the difference in the ratio of m/q of the ion of interest to the reference ion, $\Delta(m/q)$, while the relativistic effect in this measurement setup scales with $\Delta(q/m)$. In addition, an oscillating ion can induce image charges in the trap electrodes (investigated in detail in [127, 128]), that create an electric field which in turn reacts on the stored ion and shifts its motional frequencies. The effect scales with q^2. Nevertheless, it is negligible

due to the large trap size of MPET and the RF amplitude used. The systematic uncertainty for the accuracy checks was conservatively estimated to be < 15.5 ppb (absolute) and is indicated in Table 5.1 in the second set of parenthesis. Therefore, a small ratio-difference $\Delta(m/q)$ of the ion of interest to the reference ion is essential. We used $^{85}Rb^{13+}$ with $(m/q) = 6.5$ as the reference ion to minimize $\Delta(m/q)$ effects.

g) Isobaric contaminations

Systematic shifts of the frequency due to isobaric contaminations need to be minimized. The Sr beam was free of contaminations since the yield was several times larger than for the isobaric isotopes. See Section 4.1.1 for a description on how the neutron-rich Rb and Sr beams were produced. For all Rb mass measurements, not all contaminant ions could be removed using ISAC's mass separator. We used a dipole radio-frequency excitation [1] (more details see Section 3.2.2) preceding the quadrupole frequency scan to remove all contaminants, identified to be the Sr isobars.

5.3 Results

The results of the mass measurements of ^{94,97,98}Rb and $^{94,97-99}$Sr performed for this thesis with TITAN are summarized in Tables 5.1 and 5.2 and discussed in the following subsections. The absolute uncertainty of all investigated isotopes is below 4 keV, including the new direct mass measurement of ^{98}Rb. Table 5.1 lists the measured TITAN frequency ratios R with the uncertainties described in Section 5.2, as well as the combined uncertainty. The next table (Table 5.2) shows the resulting mass excess value and compares it with mass values found in the literature. A visual comparison between the mass excess measured by TITAN and previous measurements is shown in Figure 5.7. A global mass evaluation as outlined in [28] was performed with the Atomic-Mass Evaluation group in Orsay, France. The final evaluated values for the ions of interest in this work can be seen in Table 5.5 and found later in the text in Section 5.4 and Table 5.5.

5.3.1 Neutron-rich Rb isotopes

^{94}Rb The measurement campaign started with ^{94}Rb ($T_{1/2}$ =2.702(5) s), which was known with an uncertainty of $\delta m = 8.4$ keV in the AME03 [28]. A cyclotron resonance of $^{94}Rb^{15+}$ is shown in Figure 5.4. The measured mass excess of -68562.6(2.4) keV is in agreement not only with the AME03

Table 5.1: Frequency ratios of $^{94,97,98}Rb^{15+}$ and $^{94,97-99}Sr^{15+}$ isotopes relative to $^{85}Rb^{13+}$ as well as their mass excesses. Uncertainties are expressed in parenthesis. The first error on the frequency ratio includes the statistical error including the count-class analysis, and time correlations. The second and third error represent systematics related to $\Delta(m/q)$-dependent shifts and ambiguities in the choice of the time-of-flight range. The fourth error in square brackets represents the quadrature sum of all errors, since all errors are considered to be not correlated to each other.

Isotope	$T_{1/2}$	# of meas.	$\overline{R} = \nu_{c,ref}/\nu_c$
$^{94}Rb^{15+}$	2.702 s	4	0.958672311(22)(16)(3)[27]
$^{97}Rb^{15+}$	169.9 ms	6	0.989404952(17)(16)(0)[23]
$^{98}Rb^{15+}$	114 ms	(6 + 4)*	0.999658513(31)(16)(14)[38]
$^{94}Sr^{15+}$	75.3 s	5	0.958559623(10)(16)(0)[19]
$^{97}Sr^{15+}$	429 ms	4	0.989294688(37)(16)(2)[40]
$^{98}Sr^{15+}$	653 ms	3	0.999525849(41)(16)(5)[44]
$^{99}Sr^{15+}$	269 ms	10	1.009776308(42)(16)(3)[45]

* Six measurements have been performed with the resonance minimum off-center; four measurements with the minimum on-center.

Table 5.2: The measured mass excess of $^{94,97,98}Rb$ and $^{94,97-99}Sr$ and their comparison to AME03 [28] and JYFLTRAP (Rb [6], Sr [5]).

Nuclide	ME_{TITAN} (keV)	ME_{AME03} (keV)	$ME_{JYFLTRAP}$ (keV)
^{94}Rb	-68562.6(2.4)	-68553.4(8.4)	-68564(5)
^{97}Rb	-58519.2(2.1)	-58356.3(30.5)	-58519(6)
^{98}Rb	-54318.4(3.4)	-54221.6(50.2)	
^{94}Sr	-78845.8(1.7)	-78840.4(7.2)	
^{97}Sr	-68581.2(3.6)	-68788.1(19.2)	-68587(10)
^{98}Sr	-66424.5(4.0)	-66645.7(26.3)	-66431(10)
^{99}Sr	-62506.8(4.1)	-62185.7(80.0)	-62524(7)

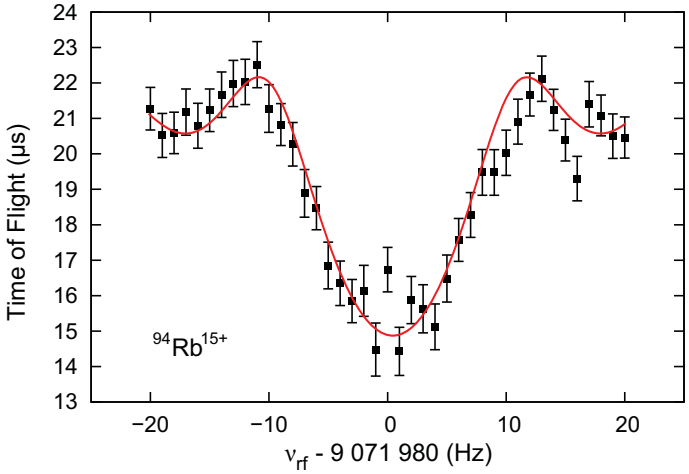

Figure 5.4: $^{94}Rb^{15+}$ cyclotron resonance taken with 80 ms charge-breeding time, 20 ms dipole cleaning, and 77 ms excitation time in MPET. The solid line is a fit of the theoretical line shape [84] to the data.

value (see Table 5.2) but also with the Penning-trap mass measurements at ISOLTRAP [129] and JYFLTRAP [6]. Moreover, the uncertainty achieved in the present work reduces the uncertainty compared to the AME03 value by a factor of three, and to the JYFLTRAP value by a factor of two.

^{97}Rb The measured mass excess value for ^{97}Rb with $T_{1/2}$ =169.9 ms of -58519.2(2.1) keV lies within the uncertainty of the JYFLTRAP value [6], but differs by 163 keV (5.3σ) from the value adopted by AME03 [28]. This work confirms the JYFLTRAP value but provides improved precision. The previous measurements considered in the AME03 were based on β end-point energies from the ^{97}Rb(β^-)^{97}Sr decay. The adjusted Q-value, including the TITAN input, is now 10063(4) keV, compared to the other measurements listed in Table 5.3. It seemed that the experiment from reference [130] missed some energy levels since the three later results obtained larger Q-values. Nevertheless, the TITAN mass value validates the first measurement [130] and greatly improves the precision of the Q-value and mass.

This new and precise value provides input for the evaluated mass in the next mass evaluation [134] with an influence of currently 87.0% (see Table 5.5).

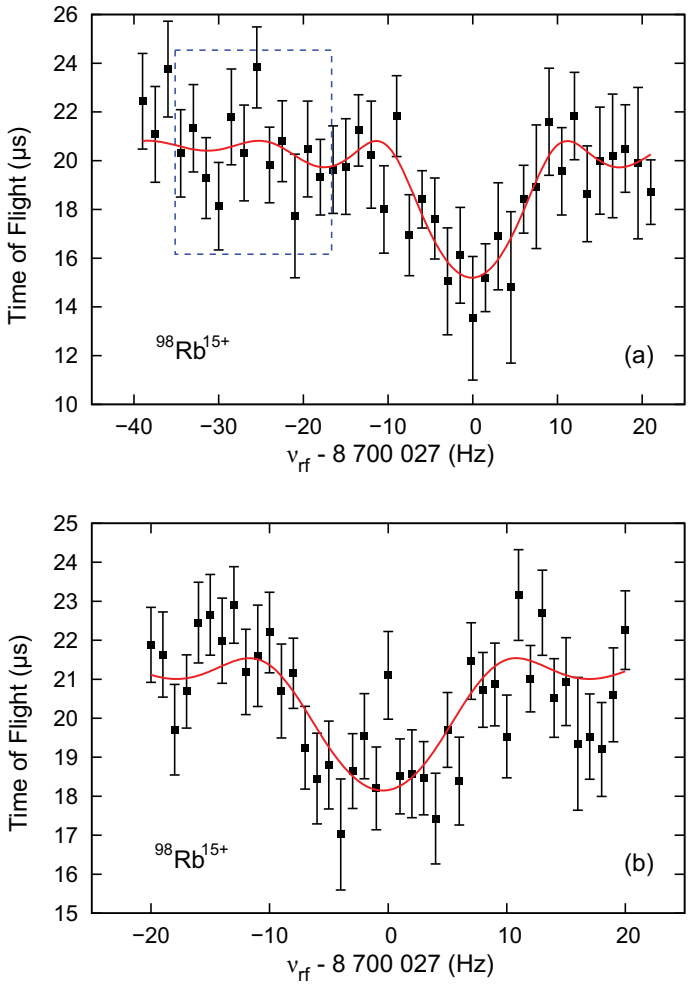

Figure 5.5: The cyclotron resonance for $^{98}Rb^{15+}$ is taken with 80 ms charge-breeding time, 20 ms dipole cleaning to eliminate $^{98}Sr^{15+}$, and 77 ms excitation time in MPET. The solid line is a fit of the theoretical line shape [84] to the data. (a) The graph shows the resonance off-center to include the range of the proposed isomer ^{98m}Rb in frequency space, indicated by a dashed blue square. (b) The graph shows another measurement with a centered resonance. See Tables 5.1 and 5.2 for results.

Table 5.3: The Q-values from previous mass measurements of ^{97}Rb considered in the AME03 were based on β end-point energies from ^{97}Rb(β^-)^{97}Sr. Now, the adjusted Q-value (including the TITAN input) is 10063(4) keV.

Q-value (keV)	Reference	Deviation to this work
10020(50)	[130]	0.9σ
10450(30)	[131]	12.9σ
10440(60)	[132]	6.3σ
10462(40)	[133]	10.0σ

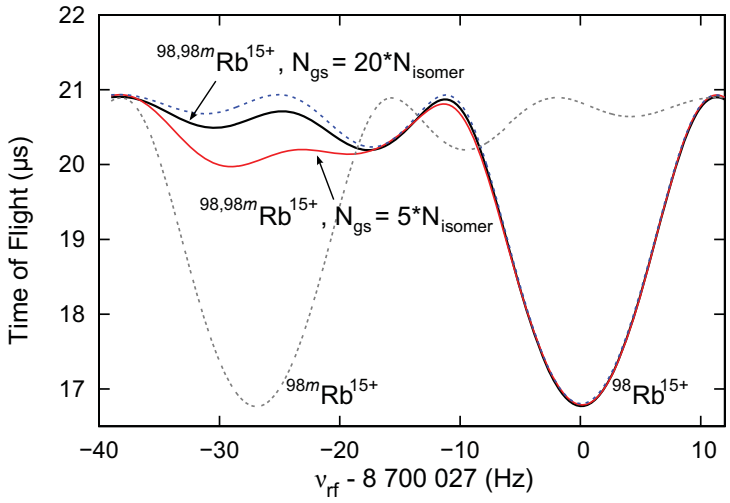

Figure 5.6: This calculation displays the theoretical line shape of the assumed isomer in dashed gray and the ground state in dashed blue for ^{98}Rb^{15+} if only one of them is present. If both were present, the solid lines indicate the line shapes for the resonance. If the yield of the isomer were a factor of 20 (5) less than for the ground state, the resonance line shape is displayed with a solid black (red) line.

^{98}Rb (ground and isomeric state)

This work presents the first Penning-trap mass measurement of ^{98}Rb. The measured mass excess of ^{98}Rb ($T_{1/2}$ =114(5) ms) is -54318.4(3.4) keV and differs from the adopted value in AME03 [28] of -54221.6(50.2) keV by 97 keV (1.9σ). The previous mass excess value was determined from the end-point energy of the β spectrum of ^{98}Rb(β^-)^{98}Sr [132, 133] with 80.4% weight and from the measurement of (^{97}Rb, ^{98}Rb, ^{95}Rb) [135] with 19.6% weight.

A low-lying isomeric state in ^{98}Rb was proposed at 286(128) keV [134] with a half-life of $T_{1/2}$ =96(3) ms [136]. In an effort to confirm the energy of the isomer, a frequency range corresponding to 630 keV was scanned (see Figure 5.5a), in which the isomer is expected to be observed. If the isomer had been present, two main minima would have been visible in the resonance curve (see Figure 5.6). Only one minimum, presumably the ground state, was observed; however, the absence of a second resonance does not exclude the possibility of an isomer. The strength of the resonances depends on the ratio of the population of the isomeric and the ground states. Yield measurements at ISAC (see [103] and Section 4.1.1 for more details) indicated the yield of the ground state to be 20 times larger than the isomeric state. If this ratio were observed with MPET, the signal is expected to be the black, solid curve in Figure 5.6, from which the isomer cannot be detected. If, however, there were only five times more ions in the ground state than in the isomeric state, the isomeric state would be detectable (red, solid curve). Unfortunatley, the yields for ^{98}Rb and ^{98m}Rb decreased over the period of the beamtime, making it impossible to see the isomeric state. To further confirm the energy of the isomeric state a higher charge state, preferably an isoelectronic series of Ar or Ne corresponding to $q = 19+$ and $q = 27+$, respectively, could be used for the mass measurement. This would imply charge breeding to a closed electron shell, which results in a narrower charge state distribution. The higher charge state would enhance the resolving power and allows one to separate the states even more in frequency space, according to Equations (3.38) and (3.39) $\mathcal{R} \propto qBT_{\mathrm{rf}}/m$. In addition, this would allow for the implementation of dipole cleaning of the ground state to enhance the resonance of the isomer.

Combining the adopted mass excess in Table 5.5 for the ground state with the one for the isomer derived from the Q-value from [132], we derive an excitation energy for this isomer of 600(120) keV.

5.3.2 Neutron-rich Sr isotopes

For all the measured Sr masses the uncertainty was reduced from previously measured values, and their impact on the adopted value in the next mass

Table 5.4: The adjusted Q-value for ^{97}Sr$(\beta^-)^{97}$Y, including the TITAN input, is now 7545(8) keV. Previously measured Q-values were underestimated and were determined from ^{97}Sr$(\beta^-)^{97}$Y.

Q-value (keV)	Reference	Deviation
7452(40) keV	[131]	2.3σ
7420(80) keV	[132]	1.6σ
7480(18) keV	[137]	3.6σ

evaluation can be seen in Table 5.5.

^{94}Sr The mass excess of ^{94}Sr was known to 7 keV accuracy from measurements at ISOLTRAP [28]. The measurement in this work agrees and improves the accuracy by a factor of 4 to 1.7 keV as presented in Table 5.1, Table 5.2 and Figure 5.7.

^{97}Sr For ^{97}Sr the measured mass differs by 207 keV (10.8σ) from the AME03 [28], but it confirms the mass measurement from JYFLTRAP [5]. In AME03 the mass of ^{97}Sr was mainly determined from ^{97}Sr$(\beta^-)^{97}$Y. The adjusted Q-value, including the TITAN input, is now 7545(8) keV. The previously measured Q-value was underestimated (see Table 5.4). The mass value measured with TITAN is a factor of three more precise than previous Penning-trap mass measurements.

^{98}Sr The scenario for ^{98}Sr is similar where the measured mass excess value of -66424.5(4.0) keV is in agreement within the error of JYFLTRAP [5] and more precise, but disagrees with AME03 [28] by 221 keV (8.4σ). AME03 adopted its value from β end-point energy experiments, with 95.5% from ^{98}Sr$(\beta^-)^{98}$Y [131] and 4.5% from ^{98}Rb$(\beta^-)^{98}$Sr [132, 133].

^{99}Sr In the case of ^{99}Sr where the mass may play an important role for the r-process and further mass extrapolations, the mass excess is found to be -62506.8(4.1) keV. This value lies within 2.5σ with the JYFLTRAP measurement [5], but it disagrees by 321 keV (4.0σ) with the mass evaluation AME03 [28]. The measured mass excess for ^{99}Sr gravitates slightly away from the JYFLTRAP value towards AME03 [28] where the adopted

Table 5.5: The most influential data to and their influences on its mass as it will appear in the next mass evaluation [134] following AME03 [28] and extended by the TITAN mass values from this work. Influences are given as a percentage and the evaluated mass excess (Eval. ME) in keV. Experimental techniques displayed as '^{94}Rb vs. ^{85}Rb' indicate Penning-trap mass spectrometry and '^{94}Sr(β^-)^{94}Y' β end-point energy experiments.

Nucl.	Infl.	TITAN	Infl.	Experiments	Eval. ME (keV)
^{94}Rb	70.2%	this work	29.6%	^{94}Rb vs. ^{88}Rb [6]	-68562.3(2.0)
^{97}Rb	87.0%	this work	12.9%	^{97}Rb vs. ^{88}Rb [6]	-58518.5(1.9)
^{98}Rb	100%	this work			-54317.7(3.4)
^{94}Sr	98.4%	this work	1.6%	^{94}Sr(β^-)^{94}Y [130]	-78845.1(1.7)
^{97}Sr	87.4%	this work	12.6%	^{97}Sr vs. ^{97}Zr [5]	-68581.8(3.4)
^{98}Sr	85.2%	this work	14.8%	^{98}Sr vs. ^{97}Zr [5]	-66425.6(3.7)
^{99}Sr	75.9%	this work	24.0%	^{99}Sr vs. ^{99}Zr [5]	-62511.7(3.6)

mass stems from β end-points from ^{99}Sr(β^-)^{99}Y [138], with 91% weight and ^{99}Rb(β^-)^{99}Sr [138], with 9% weight.

5.4 Implications for nuclear structure

Masses of exotic nuclides give valuable information concerning nuclear structure. This is particularly true in the $A \approx 100$ region where shape changes are reflected by the mass surface (see Figure 5.8). Nuclear mass models aim to accurately describe such structure in order to predict with confidence the behavior of the mass surface out to the neutron drip-line. Changes of a few hundred keV in neutron separation energy, such as those found in the $A \approx 100$ region, will have impact on the r-process path and hence, on the resulting calculated elemental abundances.

As the atomic-mass evaluation is a global evaluation of all mass measurements and results in a mass surface, the mass values obtained in this work influence mass values linked by decay chains or relative mass measurements. The measured Rb and Sr mass values have an effect on various isotopes e.g. ^{96}Zr, ^{97}Zr, ^{102}Nb, and ^{104}Nb where the mass excess changes by one standard deviation. This is shown in a more systematic way in Table 5.5. Listed here are the most important contributing data used to determine the mass value of the nuclide. A global mass evaluation was carried out, and the impact was investigated. The details of this evaluation can be found in the upcoming

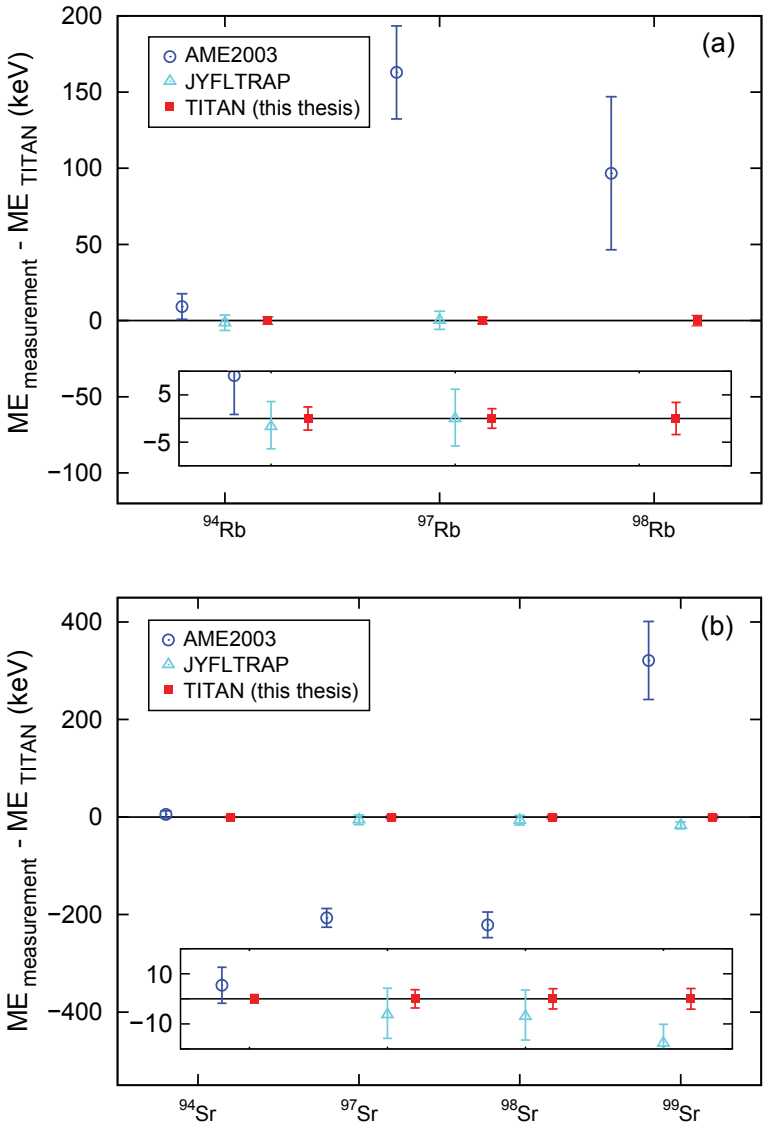

Figure 5.7: Comparison of the mass excesses determined in the present work (red squares), with JYFLTRAP [5,6] (turquoise triangles) and in AME03 [28] (blue circles). The inset displays an enlarged view.

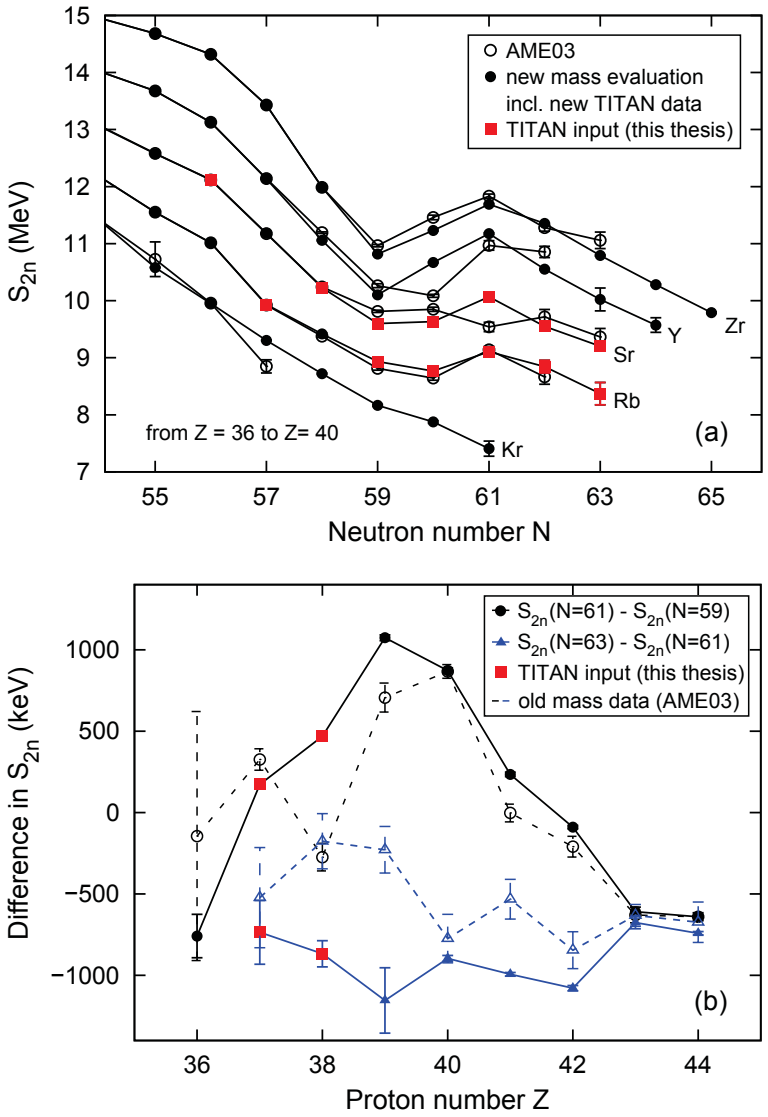

Figure 5.8: (a): Two-neutron separation energies (S_{2n}) for $Z = 36 - 40$ (Kr to Zr) versus neutron number N. Here data from AME03 [28] (open black circles) and for comparison (filled black circles), a new mass evaluation [134] including recent mass spectrometry experiments from JYFLTRAP [5–7] and ISOLTRAP [10, 139] extended by the TITAN masses are shown. The TITAN contribution of this thesis work itself is indicated by red squares. (b): Differences between the S_{2n} of the isotones $N = 61$, $N = 59$ (black circles), $N = 63$, $N = 61$ (blue triangles), and previous AME03 [28] data (dashed lines) versus the proton number Z.

mass evaluation [134]. This evaluation procedure follows AME03 [28].

To assess the impact of the measurements of this thesis on nuclear structure, Figure 5.8 (a) shows the mass surface defined by the isotopic two-neutron separation energies S_{2n}. It illustrates the deformation for $Z = 36-40$ (Kr to Zr) with data from AME03 in open black circles, recent mass spectrometry results from JYFLTRAP (for Rb, Sr, Y, Zr, Nb, and Mo masses [5–8]) and ISOLTRAP (for Kr masses [10, 139]) in filled black circles, and the neutron-rich Rb, Sr data from TITAN (this work) in red squares. Extrapolated masses are excluded due to the extrapolation procedure, which does not include physics but a smooth mass surface.

The smooth trend of the S_{2n} as seen for Kr (see Figure 5.8 (a, b) and [10]) is interrupted for other isotopic chains indicating a sudden change in the nuclear structure. The new data from this work agree with previous experiments showing an onset of large deformation for $A \approx 100$ nuclei with $N \geq 60$. This can be seen most pronounced for Rb and Sr. Previous work indicates rapidly changing behavior in nuclear structure in the region of $58 \leq N \leq 61$. To highlight the deformation, the difference between the S_{2n} of the isotones $N = 61$, $N = 59$ (black circles) and $N = 63$, $N = 61$ (blue triangles) is plotted as a function of the proton number Z as shown in Figure 5.8 (b). This observable illustrates the so-called, previous discovered, quantum nuclear shape transition [41] between $N = 61$ to $N = 59$. A shape transition is visible for Rb to Mo, whereas Kr presents the lower limit and Tc, Ru the upper limits of the deformation, respectively. With the input from this work (indicated in red squares), we obtain new data points extending to more neutron-rich isotopes. In contrast, the difference in S_{2n} for $N = 63$, $N = 61$ displays the smooth behavior again, and indicates a strengthening of a nuclear shape. For the Sr isotones from $N = 61$ to $N = 59$, previous data (AME03, dashed black lines in Figure 5.8 (b)) showed no signature of unusual behavior, while the data in this thesis strongly display the shape transition in Sr.

Previous work, especially on the theory side [13, 36] shows a detailed analysis of the shape coexistence and shape transitions in the Rb and Sr isotopes. In Figures 5.9(A) and (B) two graphs from Rodriguez-Guzman *et al.* can be found. Here the TITAN mass values are added to the 2010 publication to indicate the location in the two-neutron separation energies. A combination of charge radii (a) $\delta\langle r_c^2\rangle$ and (b) S_{2n} enables the authors to refine his model for different shapes. Experimental results from charge radii stem from [140,141], and masses from AME03 [28] and JYFLTRAP [5,6]. For the Rb isotopes the theory model from a Gogny-D1M HFB calculation allows one only to calculate odd-A Rb isotopes and all Sr isotopes. The charge radii in combination with S_{2n} permit to make a statement on the shape of the

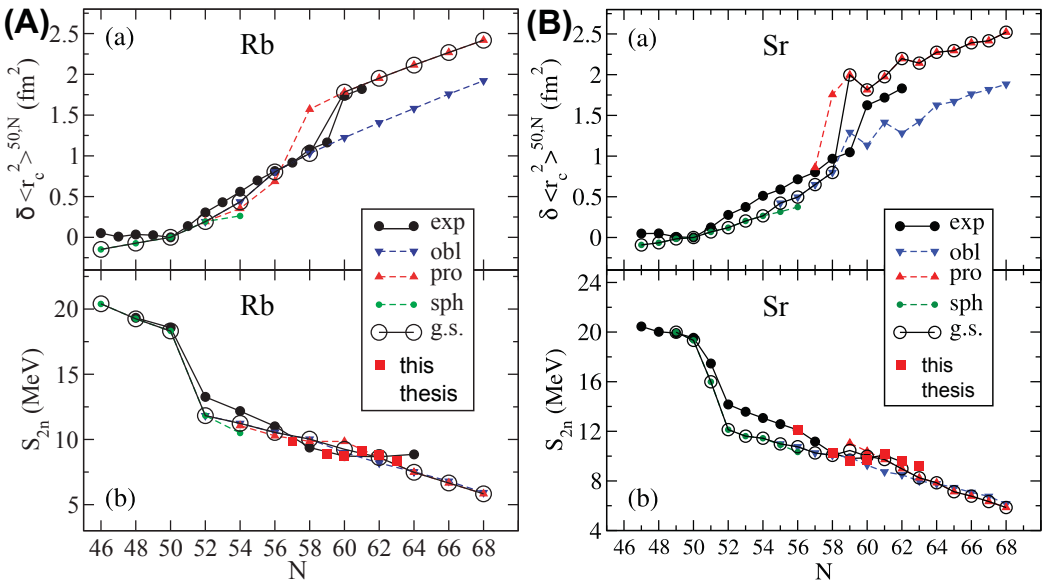

Figure 5.9: Results from a Gogny-D1M HFB calculation from [13] and [36] displaying results for (a) the charge radii $\delta\langle r_c^2\rangle$ and (b) S_{2n} in (A) odd-A Rb isotopes and (B) Sr isotopes. They are compared to previous experimental data: masses from [5, 6, 28] and radii from [140, 141]. Results for prolate, oblate, and spherical minima are displayed with different symbols (see legend). Open circles correspond to ground-state results and red squares to the mass values from this thesis.

measured isotopes in the scope of this thesis. For the Rb isotopes one finds a shape transition at $N = 60$ from oblate to prolate. This is visible in the charge radii in Figure 5.9 and in the S_{2n} in Figures 5.8(a) and 5.9(A). For the Sr isotopes a similar identification towards the deformation can be drawn from the two observables as shown in Figures 5.8(a) and 5.9(B). The mass values measured in this work point towards a prolate shape for $N \geq 60$. A transition from oblate to prolate at $N = 60$ is visible.

5.4.1 Mass models

Mass models are instrumental tools to understand various changes and behaviors in the mass surface. Particularly near the proton and neutron drip-lines, astrophysicists rely solely on mass models. Their uncertainties decrease as they are constrained by new mass measurements far from stability such as those presented in this thesis.

In this section the behavior of some selected mass models in the $A \approx 100$

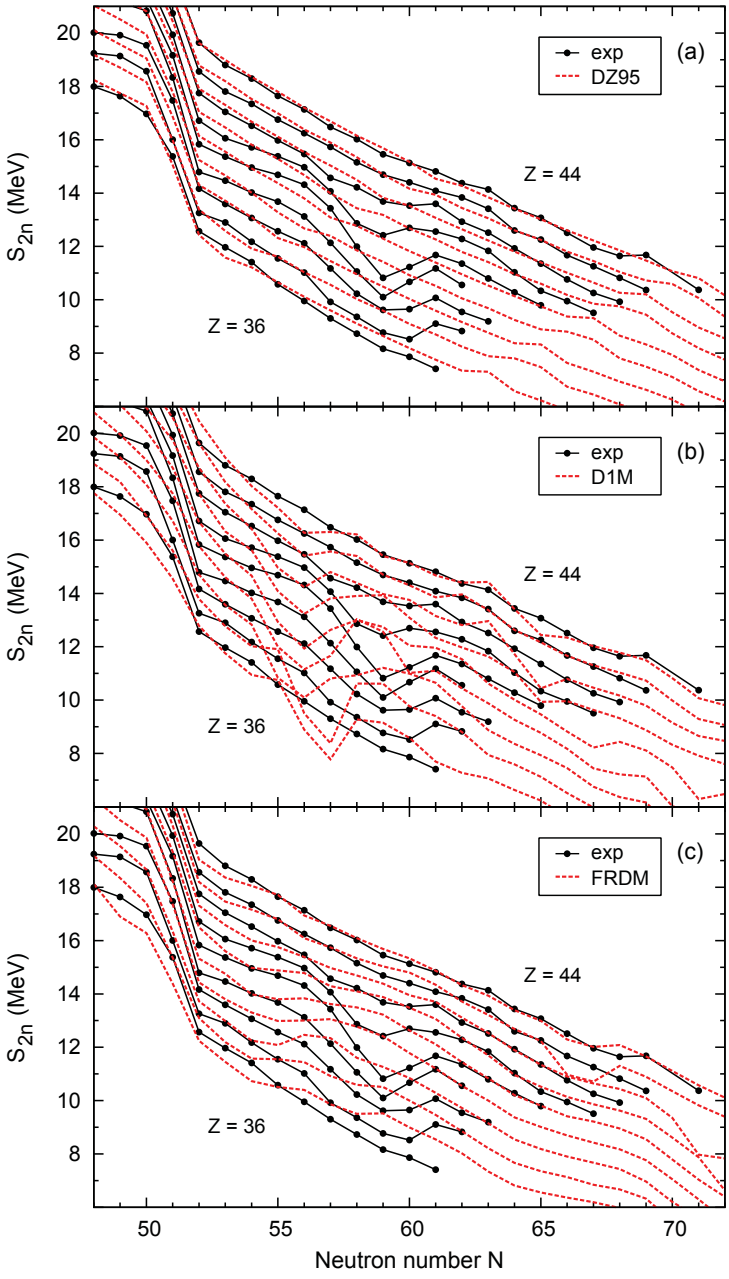

Figure 5.10: Selected mass models compared to experimental data from the new mass evaluation [134] and extended by this work. (a) Duflo-Zuker model [37] derived from a shell-model Hamiltonian, (b) HFB model with the microscopic Gogny parametrization (D1M) [35], (c) Finite-Range Droplet Model (FRDM) [31].

region (see Figure 5.10) are examined. A more detailed description of the mass models can be found in Section 2.1. A similar study was performed by Hakala *et al.* [8], who first pointed out that a comparison to a liquid drop model is clearly insufficient for this region where sudden shape changes occur. They turn to the microscopic HFB model with the Gogny-D1S and D1N parametrizations. However, only even-even nuclides are available from these models. Thus, using only a quarter of the available mass data, the most pronounced features of this region are washed out.

In order to examine this region more closely, three models have been chosen, including the most recent microscopic Gogny parametrization that has produced mass values of all nuclides: D1M [35]. For comparison, the Finite-Range Droplet Model (FRDM) of Möller *et al.* [31, 66] is also used. It is the most developed of the macroscopic-microscopic formulas. The third model will include the formula by Duflo and Zuker [37] derived from a shell model Hamiltonian. For a detailed description and comparison of these models, see Reference [2] and references therein.

Figure 5.10 shows the known two-neutron-separation energies in the $A \approx 100$ region for $Z = 36 - 44$. The different panels of Figure 5.10 show the predictions of the three different mass models mentioned above. The Duflo-Zuker model exhibits remarkable smoothness. However, though deformation is included in the model, it clearly misses this difficult $A \approx 100$ region. The FRDM model appears to anticipate the onset of deformation in this region, but the predictions go in the opposite direction, starting from the $N = 55$ sub-shell closure. The D1M masses show the trademark feature of this region – it has been interpreted as a nuclear phase transition (see [10] and references therein) – except about four neutrons (and two protons) too soon. This qualitative behavior is satisfying but some detailed corrections remain to remedy the predictions in this structure-challenging region. As mentioned by Hakala *et al.* [8], as well as by Rodriguez-Guzman *et al.* [13], who performed these calculations for the odd-A case of Rb, the answer most probably lies in a modification of the chosen model to allow for a better fit. More experimental mass measurements in this region as well as further away to more neutron-rich isotopes would enhance this process and help refining these mass models.

5.5 Astrophysical implications

The masses measured in this work are relevant for a variety of r-process models. A more detailed description can be found in Section 2.2. To explore any astrophysical implications a parametrized, fully dynamical r-process model

following Freiburghaus *et al.* [64] was employed. A model and code from H. Schatz were used [57]. The model is inspired by the conditions that might be encountered in high-entropy winds emerging from the nascent neutron star in a core collapse supernova explosion. As a starting point the model assumes a fluid element that is heated to a very high temperature ($T \approx$9 GK) and that is composed essentially of protons and neutrons, with the electron abundance Y_e being set by weak interactions. The fluid element, as can be seen in Figure 2.9, then undergoes a rapid expansion at constant velocity v, Y_e, and entropy S. The model parameters were chosen similar to Hosmer *et al.* [119], i.e. $Y_e = 0.45$ and a velocity $v = 7500$ km/s. The model is coupled to a full reaction network with 5410 nuclides that includes all relevant charged-particles, β-decays, and neutron-capture rates. For unknown masses, mass extrapolations from [28] and calculated values from the FRDM-model [31] were used. Masses enter exponentially in the calculation of (γ,n)-photo disintegration rates from the forward (n,γ)-rates via detailed balance. Calculations are carried out for a grid of entropies with the resulting isotopic abundances being calculated with equal weight. Low entropies lead to low neutron-to-seed ratios and a weak r-process producing mainly lighter r-process nuclides, while higher entropies lead to more extended reaction paths all the way to the heavier elements. An entropy range from $S = 40 - 260$ (S in units of Boltzmann's constant per baryon) is sufficient to capture all entropies that contribute to the r-process. The attractive features of this model are the following: First, it assumes a scenario of high-entropy winds from nascent neutron stars in core collapse supernovae. Second, the solar system r-process abundance pattern can be reproduced reasonably well with just two free parameters – Y_e and v [64].

To explore the relevance of the masses measured in this work for r-process simulations two calculations were performed where the neutron separation energies of $^{96-99}$Rb and $^{96-100}$Sr were varied either all up (AME03high) or all down (AME03low) by their AME03 [28] 3σ errors. This results in variations of $\pm$36, $\pm$42, $\pm$60, and $\pm$140 keV for the (A = 96, 97, 98, and 99) Rb isotopes, respectively, and of $\pm$28, $\pm$33, $\pm$33, $\pm$84, and $\pm$150 keV for the (A = 96, 97, 98, 99, and 100) Sr isotopes, respectively. A 3σ variation was chosen as such deviations are not uncommon for non Penning-trap mass measurements. In fact, the average deviation from the new masses determined in this work is 3σ, but extends to values as high as 6σ for the neutron separation energies of ^{97}Sr and ^{99}Sr.

Figure 5.11 shows the resulting composition produced by the r-process for both cases. Although the masses used for this figure stem from AME03 [28] with AMEhigh and AMElow for the isotopes measured in this work, it clearly illustrates that the new masses introduce significant variations in the

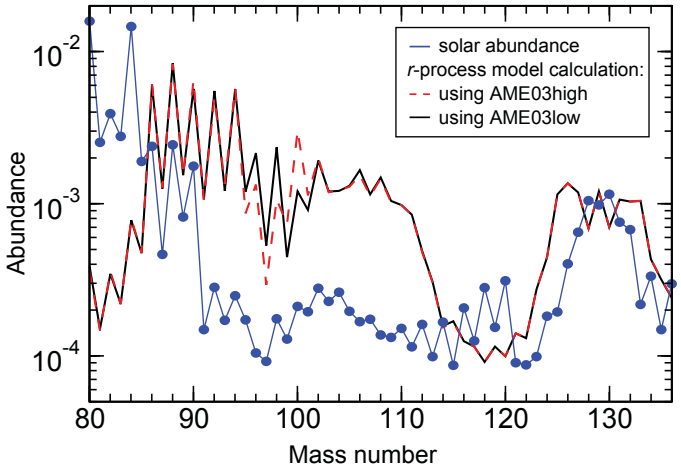

Figure 5.11: Calculated r-process abundances as a function of mass number summing all entropies for AME03high (dashed red) and AME03low (solid black) neutron separation energies for $^{97-99}$Rb and $^{97-100}$Sr. The used neutron separation energies are taken from AME03 [28] and varied either by their 3σ uncertainty up (AMEhigh) or down (AME03low). Also shown for comparison are the solar r-process residuals (filled blue circles) [142].

composition around $A = 95 - 100$ due to their deviation from AME03 of up to 6σ in neutron separation energies. The affected entropy components are about $S = 70 - 110$. The component that is most dramatically affected by the new masses is the $S = 100$ component, which is shown in Figures 5.1, 5.12(a) and (b). The reaction flows up to $A \approx 90$ are characterized by a complex network of charged-particle- and neutron-induced reactions and their inverse reactions. This charged-particle process provides the seeds for the r-process which then occurs at a somewhat later stage when temperatures have dropped and charged-particle reactions have stopped. The remaining free neutrons are rapidly captured, driving the composition to more neutron-rich species and, via β decays, up to heavier elements. The Sr isotopes are located in the transition region between these two types of reaction sequences and mark the lightest element involved in a 'rapid neutron capture' reaction sequence at this entropy. At higher entropies neutron capture starts at lower element numbers, but the r-process converts all nuclei into heavier species so there is no longer a contribution to the $A \approx 100$ mass region. As Figure 5.13 shows, higher neutron separation energies for the Sr isotopes shift the reaction flow towards more neutron-rich nuclei. For low S_n the dominant Sr waiting point, the point in an isotopic chain where the β decay into the next isotopic

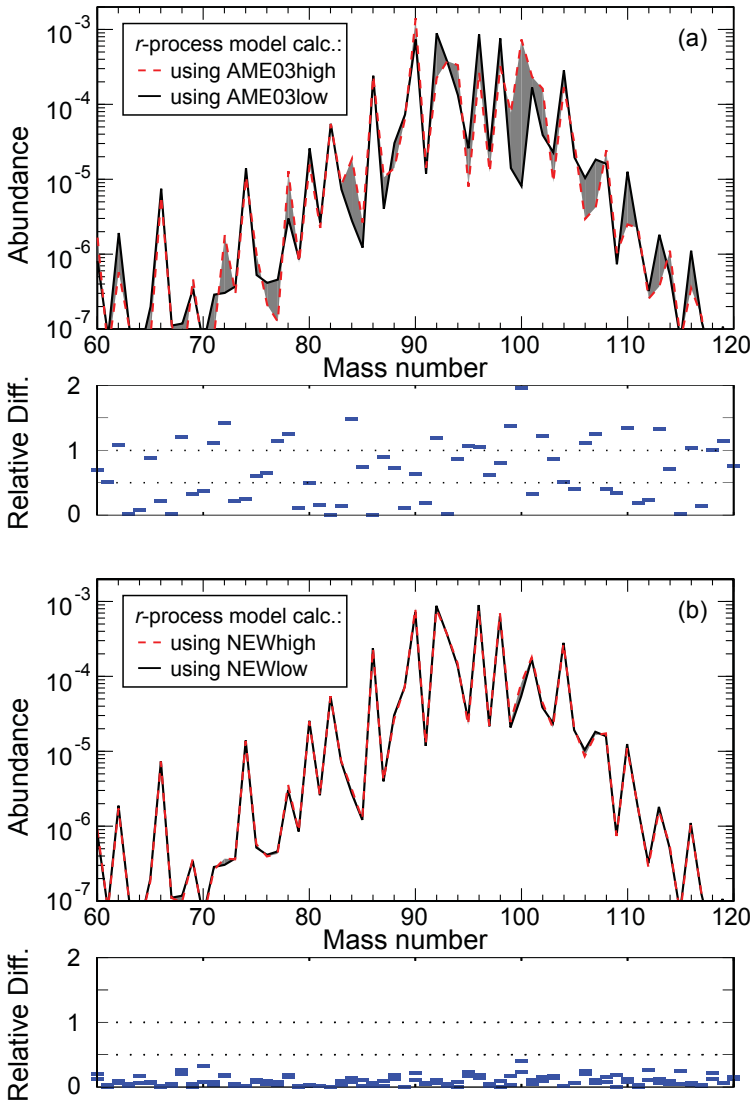

Figure 5.12: Calculated r-process abundances as a function of mass number for a single $S = 100$ component for several data sets of neutron separation energies for $^{97-99}$Rb and $^{97-100}$Sr. The upper figure (a) shows results for variations in the neutron separation energies using AME03high (dashed red) and AME03low (solid black) with the difference marked with a gray area; The lower figure (b) shows results using neutron separation energies from this work varied by the new experimental uncertainties with 3σ (NEWhigh and NEWlow, respectively). In addition both figures display the relative difference between calculated abundances using the high and the low neutron separation energies with $|\text{high} - \text{low}|/[(\text{high} + \text{low})/2]$, which is the normalization to the average value.

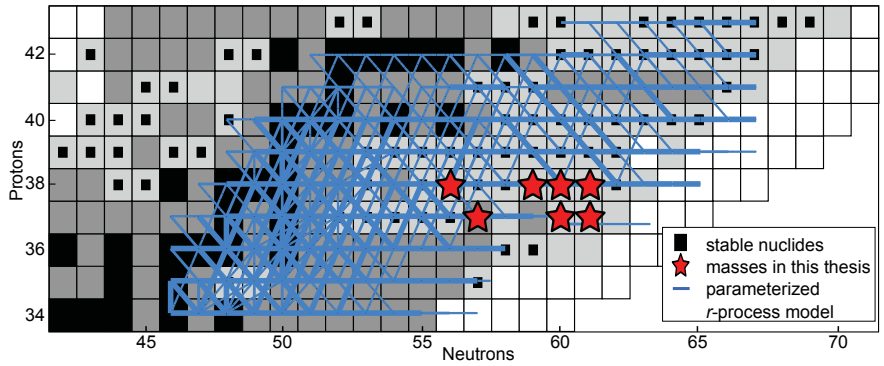

Figure 5.13: Calculated time integrated net reaction flows for a single $S = 100$ r-process component using AMEhigh. Flows above 10^{-4}, 10^{-5}, and 10^{-6} are denoted by thick, thin, and dashed lines, respectively. The nuclides of interest for this work are marked in red.

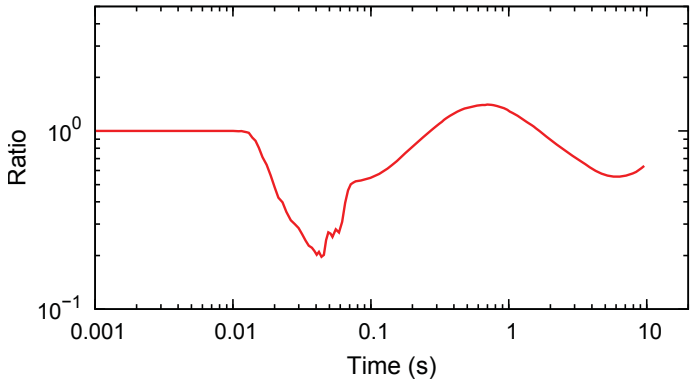

Figure 5.14: Ratio of neutron abundances in r-process model calculations with neutron separation energies AME03high to AME03low as a function of modeling time. Calculations are for a single $S = 100$ component.

chain occurs, is ^{98}Sr. For high S_n, a significant fraction of the reaction flow proceeds via neutron capture on ^{98}Sr to the ^{100}Sr waiting point, leading to an increase in the production of $A = 100$ nuclei.

With the new Penning-trap mass measurements in this work, combined with the work of Hager *et al.* [5], the contribution of mass uncertainties in neutron-rich Rb and Sr isotopes to the r-process abundance pattern becomes negligible. This is displayed in Figure 5.12(b), which shows almost no change when varying the new neutron separation energies within their new 3σ uncertainties, with NEWhigh being the variation up and NEWlow the variation down.

Also shown in Figure 5.11 are the solar r-process abundances [142], revealing the common problem of all models of this type in reproducing the solar composition of the light r-process elements with $A < 115$. While it is apparent that the mass uncertainties of the nuclei considered here cannot explain this discrepancy, the measurements in this thesis are an essential step towards removing the nuclear physics uncertainties to allow one to better characterize the disagreement.

A somewhat surprising result is that changes in the Rb and Sr masses in the $A = 96 - 100$ range result in significant abundance changes across the entire $S = 100$ component for mass numbers as low as $A = 70$. Clearly the neutron capture reaction flow in the Sr region feeds back into the nucleosynthesis of the charged-particle reaction sequence. The only possible explanation is that the switch in Sr waiting points affects the free neutron abundance. Indeed, Figure 5.14 shows drastic changes in the neutron abundance between the AME03high and AME03low calculations that sets in as soon as the Sr is reached. The shift of the reaction path towards more neutron-rich nuclei for AME03high leads to a reduction in the neutron abundance. Two conclusions can be drawn from this. First, masses can affect the final r-process abundances globally, including the production of nuclei with lower mass number. Second, neutrons clearly play an important role in shaping the composition produced by the charged-particle reaction sequence leading to an interplay between r-process and seed production.

Hence, these calculations show that the masses measured in the scope of this thesis are now known to a precision where their uncertainty does not contribute to the used r-process model uncertainty anymore.

5.6 Further developments

The mass measurements presented here represent the first time that on-line produced radioactive isotopes were measured in a Penning trap reaching such

a high charge state ($q = 15+$). In general, the increase in precision scales linearly with the charge state (see Equation (3.40)). Nevertheless, this does not include statistical losses, and it would be only true if one can counter the facts, that having an additional system in the setup reduces the efficiency, and charge breeding only results in a production of few percent of the charge state of interest (here ≈ 30 %). The approach of using highly charged ions for the mass measurement can only be exploited to date, if the production yields of the nuclides are high enough to counteract additional losses introduced by the charge-breeding process. To allow for the full benefits of using highly charged ions for the mass measurement, which yields to an increase in the precision and a reduction in the measurement time, an additional process is required to mainly reduce the energy spread of the ions coming out the EBIT. The cooler trap, developed as part of this thesis (see Chapters 6 and 7), is the tool of choice to enhance and strengthen the advantages of using highly charged ions for the mass measurement.

Chapter 6

The Cooler Penning Trap

The design of the Cooler PEnning Trap (CPET) has been accomplished in this work. This chapter gives details of the choice of cooling technique for highly charged ions (HCI) as well as in the design process. The technical implementation of electron and proton cooling is discussed. The conceptional design, followed by the mechanical and electrical design, the proposed switching schemes, and the environmental requirements to cool HCI at TITAN are presented.

6.1 Motivation for the cooler trap

The benefit of using HCI for high-precision mass measurements can be easily seen from Equations (3.1) and (3.40). A higher charge state results in a higher cyclotron frequency and thus, a higher precision can be achieved.

Due to the charge-breeding process in the EBIT (see Section 4.2.2), HCI have a much higher energy spread than singly charged ions. Based on existing data [143, 144], energy spreads of tens of eV/q are expected.

This spread as well as contaminations from the charge breeding of residual gas in the EBIT disturbs the mass measurement in the MPET. For mass measurements at the precision level performed at TITAN one needs an energy spread of ≤ 1 eV/q. The attainable precision depends strongly on the possibility of ion cooling. Cooling of HCI in a Penning trap refers to a reduction of the motional amplitudes of the HCI oscillating in the trap potential. Cold ions are located in the potential minimum of the trap and are confined in a smaller volume, and therefore probe less field imperfections. Due to the geometry of the EBIT, an extraction of a full EBIT pulse cannot be captured in the MPET [145], and a reduced longitudinal emittance is desired for efficiency. Additionally, a more bunched ion beam results in a more efficient

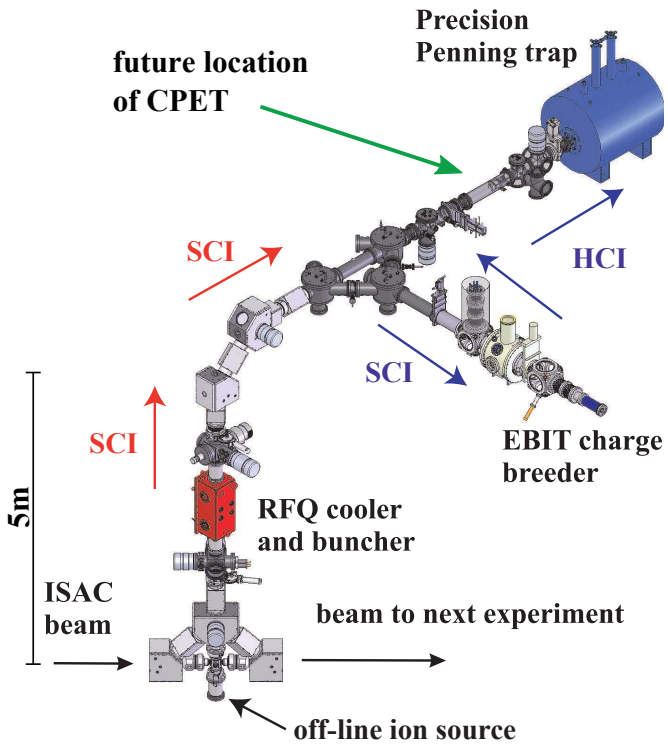

Figure 6.1: The current TITAN system (see Section 4.2) consists of three ion traps: RFQ, EBIT and MPET. The CPET for cooling HCI will be placed between switchyard and MPET (green arrow). The implementation of the full CPET setup is discussed in Chapter 7.

beam transport due to the reduced longitudinal and transverse emittance.

The new cooler trap should be fully integrable into the logic, electrical, and vacuum system of the TITAN setup. Following the logistics of cooling HCI, the preferred location for the new cooler trap (CPET) is between the switchyard and the MPET, as shown in Figure 6.1. This location should allow one to use CPET during the HCI-operation and function as a transmission device for very short-lived singly charged ion-operation. In addition to the implementation of HCI cooling, the implementation of isobaric cleaning is envisioned, which helps to prepare a clean ion sample prior to the injection into the MPET for the mass measurement. One of the main requirements is set by TITAN's measurement program and the demands for a short and efficient cooling process to allow for mass measurements of radioactive, short-lived nuclides.

6.2 Cooling methods and techniques

This section will give an overview of several methods used to cool ions in Penning traps. The relevance of each method with respect to the application of the CPET will be discussed, and the cooling techniques implemented at CPET are consolidated.

Buffer-gas cooling

Buffer-gas cooling [108] is a very commonly used technique to cool radioactive ions that are stored in a Paul or Penning trap. The TITAN RFQ (see Section 4.2.1) implements this technique while several radioactive beam facilities use it as well to cool and manipulate ions, including ISOLTRAP [109], CPT [146], and others.

In buffer-gas cooling, the ions enter the trap and lose kinetic energy due to collisions with buffer-gas atoms. After the ions are cooled and accumulated in the potential minimum, they are released and exit the trap. The buffer gas affects the ion motion and can be described as a viscous drag force $\vec{F}$. For an ion with velocity $\vec{v}$ and mass m the damping force is given by

$$\vec{F} = -\delta m \vec{v}, \tag{6.1}$$

where δ is the damping constant that can be expressed with the ion mobility K_{ion} as

$$\delta = \frac{q}{m} \frac{1}{K_{\text{ion}}} \frac{p/p_s}{T/T_s}. \tag{6.2}$$

Here, p and T are the gas pressure and temperature in units of the standard pressure p_s and temperature T_s, respectively. Generally, noble gases are used as buffer gas due to their high ionization potential and thus the reduced possibility of charge exchange. The cooling process lasts only a few milliseconds and hence is an ideal cooling technique for short-lived nuclides in Penning-trap mass spectrometer experiments. Nevertheless, the buffer-gas cooling technique cannot be applied to HCI due to charge-exchange losses.

Resistive cooling

Resistive cooling [147, 148] describes the damping of the motional energy of the stored charged particles due to the use of an external circuit which is kept continuously in resonance with the motion of the ions.

Resistive cooling uses image charges that are created on a trap surface due to the charge state of the ion. For simplicity, one considers an ion oscillating between two parallel plates. The image charges create a potential drop across

the two electrodes. As the ions oscillate the energy is driven out by means of an external resistor in a circuit, which is usually kept in a liquid helium bath at ≈ 4.2 K.

The energy dissipated as heat when a current I passes through a resistor R is I^2R (Ohm's law). Using the simple approach of an ion with charge-to-mass ratio q/m, oscillating along the x-direction between two parallel plates of distance d, the resulting current is

$$I = \frac{q}{t} = \frac{qv_x}{d}, \tag{6.3}$$

where v_x is the velocity along x-direction. The energy E dissipated through heating of the resistor damps the ion motion and can be described as

$$\frac{dE}{dt} = -I^2R = -R\frac{q^2v_x^2}{d^2}, \tag{6.4}$$

with $v_x^2 = 2E/m$

$$\frac{dE}{dt} = -I^2R = -R\frac{1}{\tau}E, \tag{6.5}$$

where $\tau = md^2/(Rq^2)$ is the constant for energy damping.

Another method is so-called 'negative voltage feedback' [149, 150]. Here the phase and amplitude is read by an external circuit, and a reverse voltage is fed back to the electrodes to enhance the damping of the ion motion.

Resistive cooling is especially efficient for ions with a large q/m ratio and the time constant can be made small using a large resistor R. Due to the long cooling times, this cooling technique is not applicable for short-lived nuclides, and is not used at TITAN. For example, a single highly charged carbon ion ($^{12}C^{5+}$) was stored and a cooling constant of $\tau = 170$ ms was demonstrated in Mainz [151]. The cooling time for resistive cooling decreases with increasing charge state. However, the cooling time increases with the square of the trap size needed to capture the ions, which can be large for particles with a high-energy spread, such as HCI. Hence, this cooling technique is not useful for CPET which has to trap ions with large longitudinal emittance. In addition, resistive cooling is q/m specific, and ions with a different q/m would have different cooling times.

Evaporative cooling

If there is a large number of ions available, evaporative cooling can reduce the ion energy distribution. A large-sized trap is needed to store the large amount of ions. While lowering the trapping potentials, a certain number of trapped 'hot' ions can evaporate out of the trap. The trapping potentials are slowly

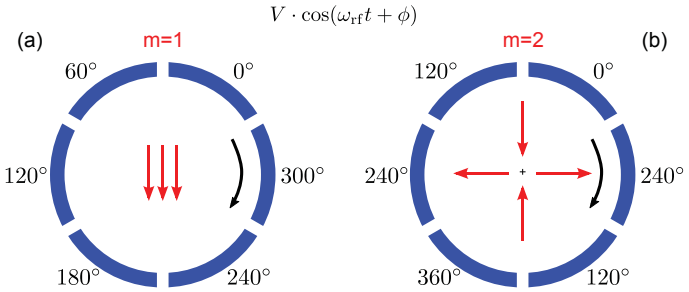

Figure 6.2: Two possible applications of rotating-wall cooling showing (a) m=1 and (b) m=2 perturbations. The sample electrode is six-fold segmented and at each segment a different phase of radio-frequency is applied. The applied voltage is rotating and the red arrows indicate the force on the ions in the center of the trap.

raised again without introducing energy to the ions, and the remaining ions can equilibrate to a thus lower temperature. The still trapped ions will have a lower motional energy. Evaporative cooling is routinely used in atom traps (e.g. [152]). Also, SMILETRAP uses this technique to cool stable HCI [153].

In ion traps evaporative cooling of few stored ions is not that efficient due to the Coulomb collisions. In an electron beam ion trap (for the TITAN EBIT see Section 4.2.2) evaporative cooling can be employed to evaporate low-Z and low-charged ions to cool the HCI. The implementation of this technique is currently tested using the TITAN EBIT (see Section 4.2.2). The novel cooler Penning trap will be a trap of large size, but unfortunately evaporative cooling will dramatically reduce the number of ions which is already limited by the yield from ISAC.

Rotating-wall cooling

The space charge effect plays a major role when the ion density is high [154]. If the density is high enough, the size of the ion cloud increases and eventually ions are lost as they hit the trap wall. Rotating-wall cooling is an effective way of reducing the radial dispersion of the ion cloud under such a condition. The quasi-cooling is performed using segmented electrodes (six- to eight-fold segmented) while the ions are confined radially in a strong magnetic field. As the spheroid of ions rotates around the trap axis, a multipole frequency is applied to the trap electrodes which drags and rotates the ion cloud around the trap axis on top of the ion's intrinsic rotation. If the applied multipole frequency is higher than the ion-spheroid's intrinsic frequency, an

overall spatial (radial) compression is achieved by exciting the plasma wave [155]. In Figure 6.2 two applications of rotating-wall perturbations are shown schematically.

In general, for a higher number of ions the radius of the ion cloud is a function of temperature [154]. However, in rotating-wall cooling the temperature effect is reduced and the radius of the ion cloud becomes a function of the ion number instead.

Rotating-wall cooling will not be implemented in CPET to cool HCI due to the low ISAC yields of short-lived nuclides. Nevertheless, CPET incorporates eight-fold segmented electrodes where rotating-wall cooling is envisioned for the electron cloud.

6.2.1 Cooling of highly charged ions

Sympathetic cooling, which refers to cooling of one type of particle through scattering by another type, was introduced in Section 6.2 with a neutral gas used for buffer-gas cooling. In this section, the focus lies on sympathetic cooling using charged particles where collisions involve Rutherford scattering. Electrons, positrons, protons and light ions can be employed in the sympathetic cooling of HCI.

Cooling HCI using positrons [156] has the benefit of no charge exchange during the mixing process, but requires a complicated setup to produce the number of positrons needed to cool HCI. As this is both man-power and money intensive, there are no plans to implement positron cooling for the CPET system. CPET has been designed and developed in the scope of this thesis to facilitate sympathetic phase-space cooling of HCI using electrons and protons. Proton cooling has not been demonstrated to date. Electron and proton cooling will be discussed in the following sections.

Electron cooling

Electron cooling is a well established technique used in storage-ring facilities (e.g. ESR at GSI [157]) as well as in cooling for protons and antiprotons as shown by G. Gabrielse [158]. Electron cooling in a Penning trap was first employed at LEAR at CERN, where antiprotons were slowed down from an energy of 3 keV to rest [158]. The Penning-trap systems ATRAP [159] and ATHENA [160] also use this technique to cool antiprotons. It is used as a key process to produce antihydrogen atoms at CERN [159] [161]. The HITRAP project [162,163] at GSI has been investigating electrons as a coolant for HCI but has not successfully demonstrated it to date.

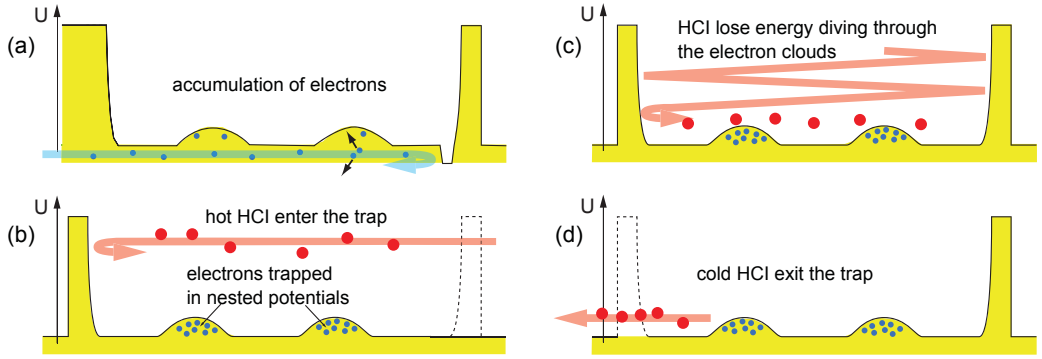

Figure 6.3: Electron cooling scheme to be implemented at CPET. (a) The electrons are injected from an electron source and accumulated in the trap. (b) HCI enter the trap while lowering the trapping gate. (c) HCI collide with electrons and lose energy. (d) The cooled HCI are extracted from the trap, while the electrons stay in the nested potentials.

In a Penning trap the magnetic field confines the charged particles in the direction perpendicular to the magnetic-field lines and the electrostatic field in the direction parallel to the magnetic-field lines. By using a cylindrical nested Penning trap such as CPET, both electrons and ions can be stored in the same trap which is required for cooling of HCI. A schematic of electron cooling as it will be implemented at CPET can be found in Figure 6.3. First, electrons are loaded and accumulated into local potential wells. This loading can employ a bunched or continuous beam of electrons (see details in Chapter 7). HCI are then trapped by lowering and raising the large trap end gate. The HCI interact with the electrons through Coulomb interaction, which leads to a frictional force that deaccelerate the ions. The ions lose energy through many collisions with the electrons until they reach the desired temperature. After electron cooling, the HCI are spatially separated from the electrons and extracted from the trap in order to be transfered to the precision Penning trap.

The primary advantage of electron cooling is that electrons cool themselves via the emission of synchrotron radiation. In a magnetic field of a few Tesla, the emission of synchrotron radiation is significant and dampens the electron motion transverse to the magnetic-field lines at time scales of seconds or faster. The emitted power of synchrotron radiation scales inversely with the fourth power of the mass of the particle, $1/m^4_{\mathrm{coolant}}$, and is therefore negligible for protons. The dissipation via synchrotron radiation has to be taken into account for electron cooling.

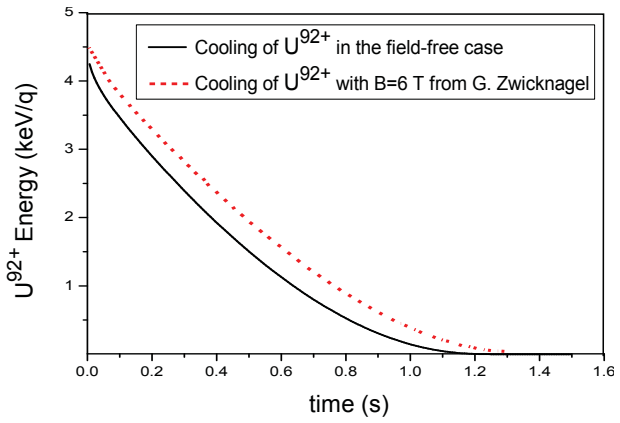

Figure 6.4: Cooling of U^{92+} in a field-free case and cooling of U^{92+} in a $B = 6$ T field [164]. Figure from [165].

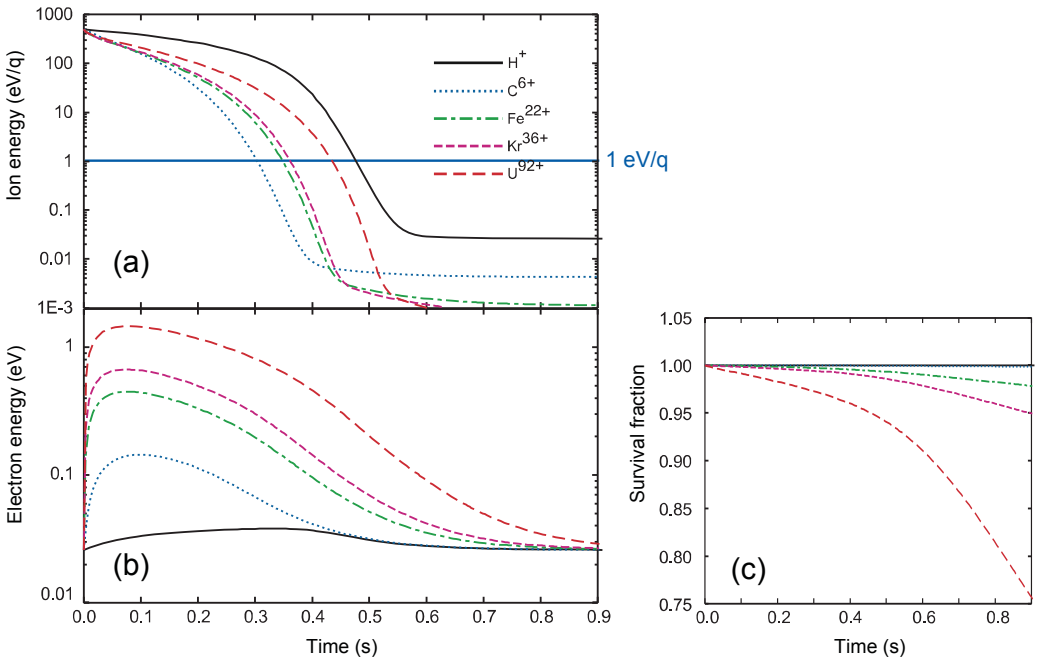

Figure 6.5: Electron cooling simulations. (a) The energy decrease for different ions over time. The horizontal line marks the desired energy of 1 eV/q. (b) The resulting electron energy. (c) Fraction of ions that survive cooling with electrons without undergoing recombination. Figures modified from [165]. Initial conditions are $n_e = 10^7$ cm^{-3}, $N_i/N_e = 10^{-4}$, $T_{res} = 300$ K, and $T_{i,0} = 500$ eV per q, respectively.

The time evolution of the electron and ion energy can be modeled using an ideal two component plasma in the absence of a magnetic field. A comparison of this simple model (details can be found in [165]) to a full theoretical description of electron cooling for the HITRAP project [164] does not show a significant difference in behavior, as illustrated in Figure 6.4 [165].

Considering an ideal two-component plasma with number of ions N_i and electrons N_e in the absence of a magnetic field, the time evolution of the electron temperature T_e and ion temperature T_i is given by

$$\frac{dT_e}{dt} = \frac{1}{\tau_i}\frac{N_i}{N_e}(T_i - T_e) - \frac{1}{\tau_e}(T_e - T_{res}) \tag{6.6}$$

$$\frac{dT_i}{dt} = -\frac{1}{\tau_i}(T_i - T_e)\,. \tag{6.7}$$

Here T_{res} is the ambient temperature (room temperature for CPET) and τ_e is the time constant for electron self-cooling via synchrotron radiation, which is ≈ 0.07 s in a 7-T magnetic field [165]. The time constant for equilibrium in a two-component plasma τ_i is given by

$$\tau_i = \frac{3(4\pi\epsilon_0)^2 m_e m_i c^3}{8\sqrt{2\pi}\, n_e q^2 e^4 \ln(\Lambda)} \left(\frac{k_B T_i}{m_i c^2} + \frac{k_B T_e}{m_e c^2}\right)^{3/2} \tag{6.8}$$

where k_B is the Boltzmann constant, q is the charge of the ion, n_e is the electron density, and m_i and m_e are the ion and electron mass, respectively. The Coulomb logarithm $\ln(\Lambda)$ for the electron-ion plasma is given by

$$\ln(\Lambda) = \ln\left(4\pi\left(\frac{\epsilon_0 k_B}{e^2}\right)^{3/2}\frac{1}{q}\sqrt{\frac{T_e}{n_e}}\left(T_e + \frac{m_e}{m_i}T_i + 2\sqrt{\frac{m_e}{m_i}T_e T_i}\right)\right). \tag{6.9}$$

The difference between cooling of HCI and antiprotons lies in the fact, that electrons are attracted to HCI and recombination processes become important. Electron-ion recombination can be divided into three processes: radiative recombination, dielectronic recombination, and three-body recombination. Radiative recombination is the most prominent one [165], and can be expressed as

$$A^{q+} + e^- \longrightarrow A^{(q-1)+} + h\nu. \tag{6.10}$$

An ion interacts with an electron and the electron is captured directly into a vacant bound state, and the emitted photon carries away the excess energy $h\nu$. Simulations of electron cooling of different ions is shown in Figure 6.5 which displays the decrease of the ion energy as a function of time. A line at 1 eV/q represents the desired energy. On the same time scale the electron

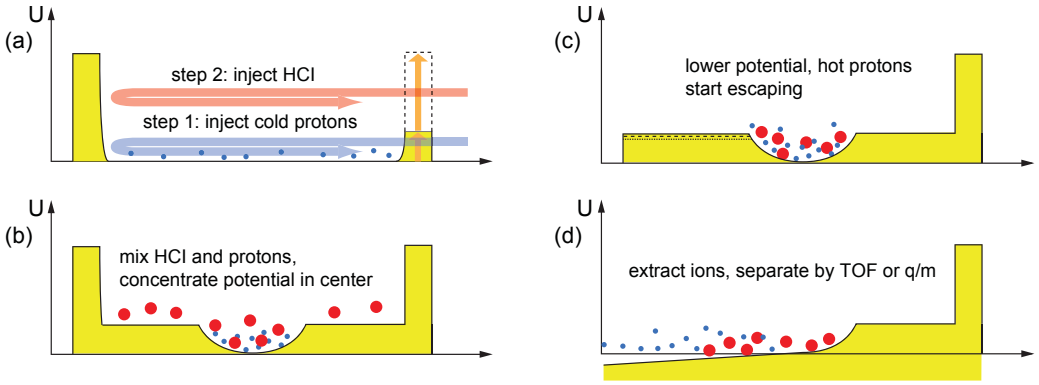

Figure 6.6: Proton cooling scheme to be implemented at CPET. (a) Cold protons are injected into the trap. After rising the gate potential to keep the protons, HCI are injected. (b) While HCI and protons mix, they are confined in a smaller potential well. (c) HCI lose energy due to collisions with protons, and will rest deeper in the potential well. Lowering the potential allows for hot protons to escape. (d) The cooled HCI and protons are extracted from the trap and can be separated by TOF- or q/m-separation.

energy first increases rapidly due to collisions, but decreases again due to the emission of synchrotron radiation.

The cooling of HCI with electrons happens on a timescale of $\approx 0.24{-}0.35$ s (depending on the ion species) [166]. In this time the HCI survival fraction (i.e. the number of ions left in the initial charge state) remains high (see Figure 6.5(c)), which would even allow sympathetic cooling of U^{92+}.

Proton cooling

Proton cooling is very similar to electron cooling, except protons do not cool efficiently via synchrotron radiation. Therefore, a source of cold protons is required. The collisional processes are similar to electron cooling and Equations (6.6) to (6.9) convert to the following equations:

$$\frac{dT_p}{dt} = \frac{1}{\tau_i}\frac{N_i}{N_p}\left(T_i - T_p\right) \tag{6.11}$$

$$\frac{dT_i}{dt} = -\frac{1}{\tau_i}\left(T_i - T_p\right) \tag{6.12}$$

$$\tau_i = \frac{3(4\pi\epsilon_0)^2 m_p m_i c^3}{8\sqrt{2\pi}\cdot n_p q^2 e^4 \ln(\Lambda)}\left(\frac{k_B T_i}{m_i c^2} + \frac{k_B T_p}{m_p c^2}\right)^{3/2} \tag{6.13}$$

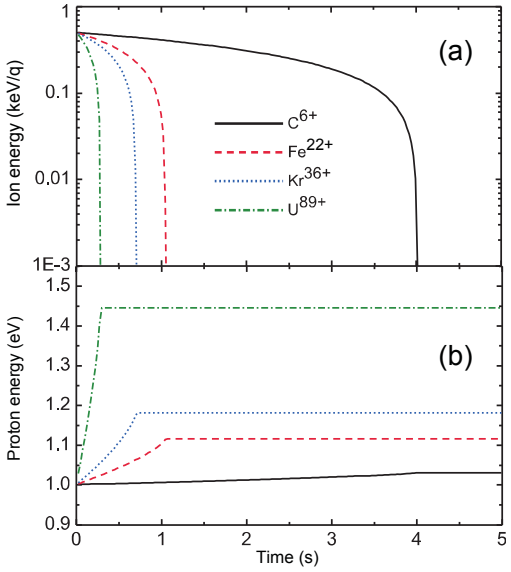

Figure 6.7: Proton cooling simulations. (a) The energy decrease for different ions over time. (b) The resulting proton energy. Figures modified from [165]. Initial conditions are $n_p = 10^8$ cm^{-3}, $N_i/N_p = 10^{-5}$, $T_{res} = 300$ K, and $T_{i,0} = 500$ eV per q, respectively.

$$\ln(\Lambda) = \ln\left(4\pi\left(\frac{\epsilon_0 k_B}{e^2}\right)^{3/2}\frac{1}{q}\sqrt{\frac{T_p}{n_p}}\left(T_p + \frac{m_p}{m_i}T_i + 2\sqrt{\frac{m_p}{m_i}T_pT_i}\right)\right), \quad (6.14)$$

with proton mass m_p, density n_p, and temperature T_p. Terms relative to dissipation through synchrotron radiation have been neglected.

A schematic of proton cooling, is shown in Figure 6.6. The cooling cycle begins with the injection of protons into the trap and raising the trap gate to prevent protons from escaping. HCI are then injected. While both ions and protons collide with each other, the potential well is made tighter to confine both species in a smaller volume. Hot protons will escape the trap as their energy gets to large to be confined, while HCI lose energy and move deeper into the potential well. Evaporative cooling techniques can then be applied to force more hot protons to escape. After cooling, both HCI and protons get extracted from the trap to the precision Penning trap, where they can be separated via TOF or q/m selection.

Proton cooling simulations [165] are shown in Figure 6.7, where the decrease in ion energy and the increase in proton energy are plotted over time.

It indicates the possibility of proton cooling on a timescale of $\approx 0.15 - 2.3$ s (depending on the ion species). This makes proton cooling applicable for cooling of radioactive HCI at TITAN.

6.3 Conceptual design

To fully exploit the benefits of using HCI for high-precision mass measurements, the cooler trap is needed. From a careful consideration of cooling techniques, which could be used to cool short-lived HCI ions effectively, electron and proton cooling using Coulomb interaction are envisioned.

The two cooling techniques and the requirements for the cooler trap, as described in Section 6.2.1, set the conceptual design parameters which have to be addressed in the overall design of the cooler trap:

- Since electron cooling requires a high magnetic field to cool the electrons efficiently using synchrotron radiation, a Penning trap design with a solenoid magnet is foreseen, and hence the name Cooler Penning Trap (CPET).

- A full integration into the TITAN system is required. The magnet therefore needs to be a shielded magnet so that no magnetic-field lines interfere with mass measurements in MPET. In addition, the CPET system should allow for a transmission operation of singly charged ions (SCI) towards MPET (e.g. no diagnostics on-axis). The whole CPET-setup should fit between the TITAN switchyard and the MPET.

- A full ion bunch extracted from the EBIT should fit in the CPET trap structure. The length of the trap region sets the requirement of a homogeneous magnetic-field region to be in the order of 400 mm.

- To manipulate HCI efficiently without losses, the vacuum requirement is quite high. A pressure approaching 10^{-11} Torr (calculated in Section 6.8.2) is desirable to keep the ions of interest in their initial charge state without any charge-exchange losses.

- A nested trap is needed for the cooling processes. This requires many electrodes that can flexibly shape nested potentials. In addition, high-voltage is needed to dynamically construct nested potentials and furthermore move particles from one end to the other. No additional heating of the charged particles is wanted during this process. A flexible shaping of a multitude of nested hills and wells sets a requirement

for electronics. Moreover, the trap structure should implement fast-switching and dynamical gates, to trap a particle bunch, and to extract it without additional heating, respectively.

- Many particles (i.e. electrons, HCI, and protons) are involved where electronics and potentials need to be switched between all participating particles.

- CPET is designed to cool HCI with electrons or protons. Additionally, areas to pre-cool the coolant should be envisioned as well as areas for the implementation of different cooling and excitation techniques which can be studied. Dipole excitation for isobaric cleaning and the application of plasma cooling techniques are envisioned.

6.4 Mechanical design

The Cooler Penning trap (CPET) was designed and constructed in the course of this thesis, and the status of the system was published at various stages [167, 168]. To aid in the design of a trap concept meeting the requirements as presented in Section 6.1 and 6.3, the simulation software SIMION [80] was used to perform a full set of simulations for the sympathetic cooling of HCI using electrons and protons. SIMION is a charged particle optics simulation package used to simulate particle trajectories in electric and magnetic fields. SIMION solves the Laplace equation using the 4^{th} order Runge-Kutta method with variable-length and dynamically adjustable time-steps. To include space-charge effects in SIMION, charge-repulsion methods can be enabled, which account for Coulomb-like particle-particle forces including ion-cloud corrections and simulate repulsion between all the beam particles. In addition, forces between the particles and the electrodes surfaces were included for particle trajectories while including the so-called Poisson Solver, which uses an iterative method to solve the Poisson equation.

Based on extensive simulations and their results, it was found that a multi-ring cylindrical Penning trap (MRT) satisfied the CPET design requirements. The flexibility of the MRT provides for the shaping of nested potentials, regions of high harmonic quality, and regions for different excitation techniques. As shown in Figure 6.9, it consists of 29 ring electrodes with identical inner diameter (35.0 mm) and length (12.7 mm, separated by 1 mm long macor spacers). Figure 6.8 (and Figure 3.2 in Chapter 3) show the electrodes modeled in a SIMION simulation used to determine the design of the CPET trap structure. The large number of electrodes permits one to shape the potential in the most flexible way, similar to discussion in [169, 170].

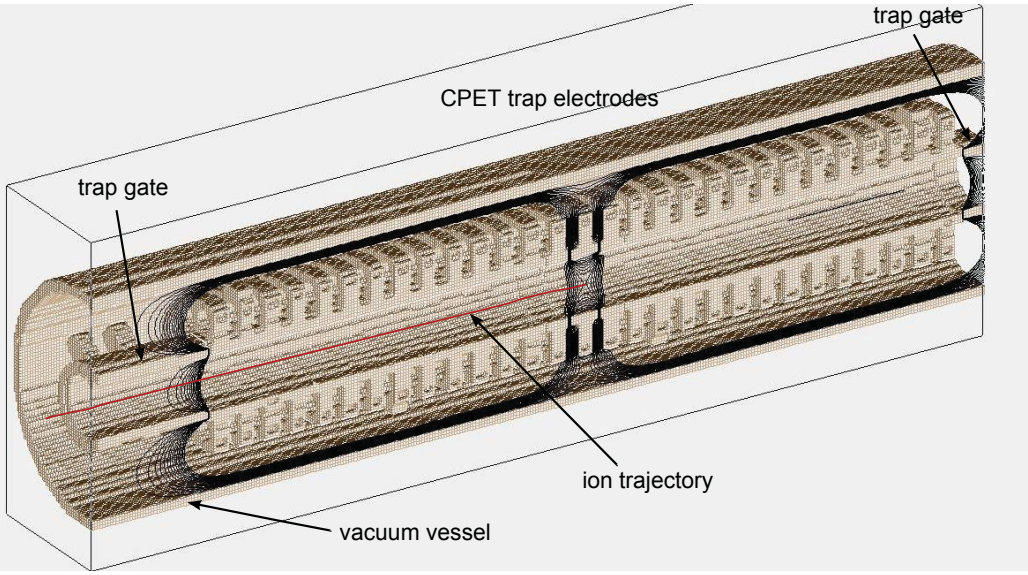

Figure 6.8: SIMION simulation of the CPET electrode structure with a cross-sectional view. The red line shows the trajectory of an ion injected into the trap while switching the applied potentials on the trap electrodes, and then trapped in the center.

The length of the trap structure is set by the maximum length of an ion bunch coming out of the EBIT. This varies for different species and breeding times, and a value of 40 cm should be very suitable. A 7-Tesla actively-shielded magnet with a homogeneous region of $\delta B/B = 10^{-3}$ over 40 cm in the magnet center is ensured. For more details on the magnet and the magnetic field, a three-dimensional magnetic-field mapping has been performed and is discussed in Section 6.8.1. For the simulations the finite length of the homogeneous region was considered.

Figures 6.10 and 6.12 show a picture of the assembled trap structure, and Figure 6.13 (right) displays the majority of components which went into its construction. The HCI enter from the right hand side. They pass through a Lorentz steerer [117] and a long drift tube before entering the main trap region. The two longer electrodes on either side of the gold trap electrodes form the end-caps of the trap and are the so-called gate electrodes that can be switched within 100 ns (see Chapter 7) to capture and extract ion bunches. Details of the actual trap electrode structure are displayed in Figures 6.9 and 6.10 as well. In the center of the trap, there is an 8-fold segmented electrode, surrounded by two 2-fold segmented electrodes. An identical set of 2-8-2 segmented electrodes is installed downstream on the

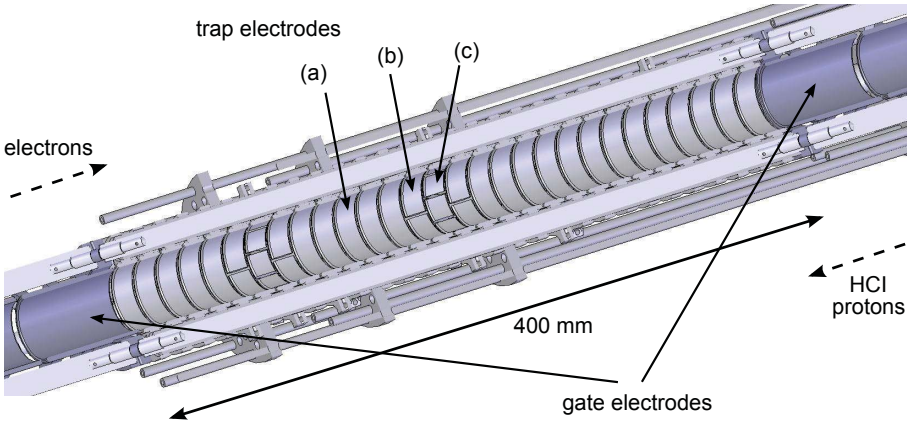

Figure 6.9: Cross section of a Solid Works drawing of the trap structure showing the arrangement of the electrodes. Electrons enter the trap region from the left, and HCI and protons from the right, respectively. The main electrode structure is a multi-ring trap design, consisting of 29 cylindrical ring electrodes. Three different types are used: (a) non-segmented, (b) 2-fold segmented, and (c) 8-fold segmented electrodes.

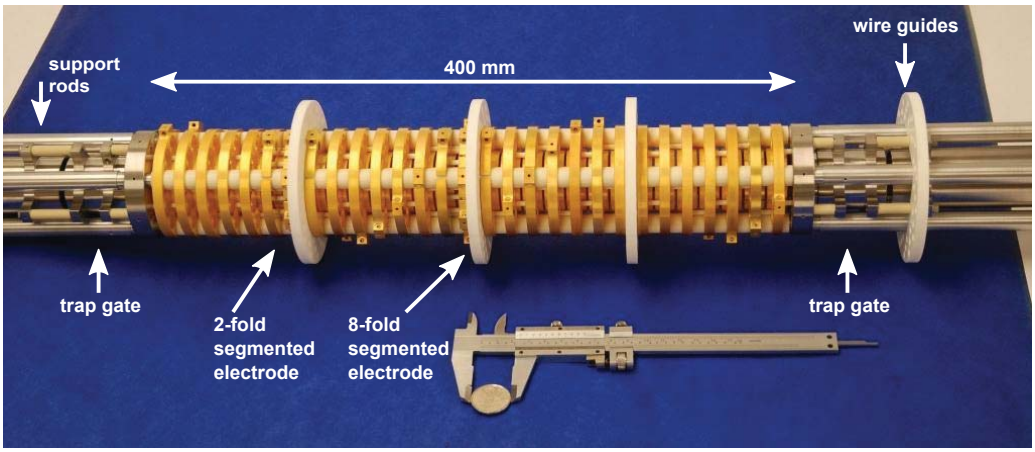

Figure 6.10: Picture of the assembled CPET trap structure. For clarity, the wires and ceramic tubes guiding the wires are not mounted.

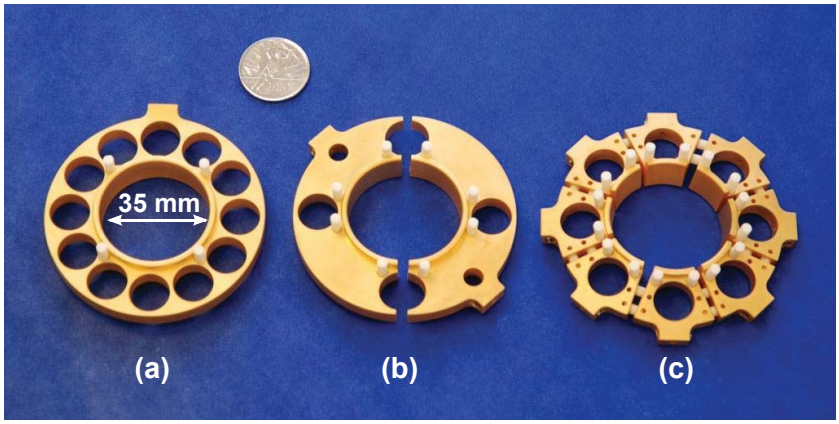

Figure 6.11: Picture of the three types of electrodes implemented in the CPET trap structure. (a) non-segmented, (b) 2-fold segmented, and (c) 8-fold segmented electrode.

electron-injection side. The purpose of the split electrodes is to facilitate RF excitation (dipole, quadrupole and octupole) (see Section 3.2), plasma diagnostics, and the application of a rotating-wall technique for the electron plasma (see Section 6.2). Additionally, one could apply a quadrupole excitation and perform all mass-measurement-specific excitations as mentioned in Section 3.2.

Figure 6.11 shows the three different types of machined electrodes made from high-purity oxygen-free copper. Patched oxidation of the electrode surfaces causes undesired stray electric fields [171], which modify the electric potential. To minimize such effects, the trap electrodes' surfaces have been silver and then gold-plated with each $\approx$ 10 μm thick layers. To reduce weight and add pumping speed, the outer parts of the electrodes are reduced in thickness and have holes. Axial spacing of the trap electrodes is maintained using ceramic spacers, visible in Figure 6.11. Additional ceramic spacers provide the distance between the segments of the 8-fold segmented electrodes.

The gate electrodes, as can be seen in Figures 6.9 and 6.10, are machined from high-purity stainless steel and form the end-caps of the trap structure. On either side of the end gates are long stainless steel drift tubes (see Figure 6.12). On the electron-injection side the drift tube will then be biased close to the electron-source bias voltage to allow the electrons to enter the trap structure. This drift tube will be biased to ground potential to let the HCI exit the trap and accelerate them towards the MPET.

Simulations were performed to determine the most suitable location and shape of the steerer for the ions. Ideally, the steerer should be implemented in

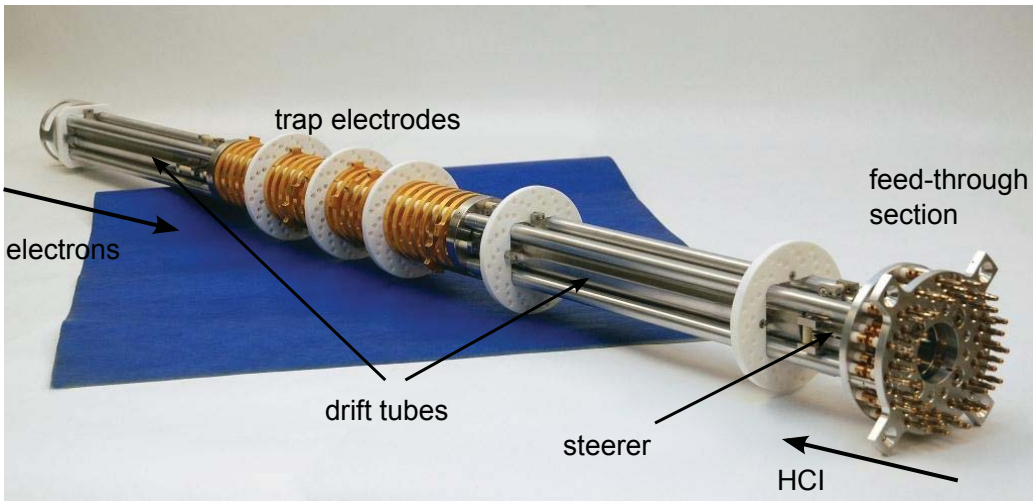

Figure 6.12: A complete picture of the CPET structure which will be installed inside the magnet. It includes the trap structure, trap gates, drift tubes and the steerer in the HCI injection side. The first part of the feed-through section with its 45 plugs can be seen.

the form of a Lorentz steerer (see Section 4.2.3), which operates in the weak fringe field of the magnet. A four-split cylindrical steerer with similar diameter to the trap electrodes was designed and located close to feed-through section as can be seen in Figure 6.13 (left and middle). Having the steerer in the magnetic fringe field enables the possibility to bring the ions on a magnetron radius as discussed in Section 4.2.3. This permits to perform mass measurements in the CPET, which is not intended at this point but could be used in the future.

The large number of electrodes allows for flexible shaping of the trapping potentials, but presents a challenge for the mechanical design. In particular, the fixed magnet bore and trap tube diameters requires a compact design for feeding high-voltage to the electrodes. To accomplish this, a complex feed-through section was designed and can be seen in Figures 6.14 (left, middle, and right). The left picture shows the feed-through plugs that are part of the trap structure. The middle picture shows an intermediate stage of the assembly, whereas the right picture is the complete version. The part of the trap structure (left) then plugs into the feed-through section and forms a connection between the electrodes in the vacuum and power supplies outside the vacuum. Electrical contact to the wires is provided by high-purity oxygen-free copper wires, which are guided using ceramic tubes.

The assembly of the trap electrode section is complicated by the need to

Figure 6.13: Left and Middle: Pictures of the four-split cylindrical steerer in the magnetic fringe field of the magnet. The middle pictures shows the close location to the feed-through section. The picture on the right displays many of the fabricated parts for the CPET trap structure.

Figure 6.14: Pictures of the CPET feed-through section. The left picture shows the feed-through plugs that are part of the trap structure. The middle picture displays an intermediate stage of the assembly, whereas the right picture is the complete feed-through section.

wire things in a certain order. First, the labeling scheme and wiring configuration needs to be covered. Since 45 different feed throughs are available, explicit labeling is necessary. Table 6.1 explains the abbreviations given for each electrode in the trap structure, whereas Figure 6.15 (left) shows the specific location of each electrical feed through. The electrodes are fed by high-purity oxygen-free copper wires that are guided in ceramic tubes which are cut to specific lengths. During the assembly few wire guides get blocked. This is indicated by a different color scheme and helps during the assembly process. All trap support plates have 15 sets of three holes. Each set is numbered, starting with the set at 12:00 and increasing clockwise. In each set the inner, middle, and outer holes are labeled as -1, -2, and -3, respectively. A section of the trap structure is shown in Figure 6.15 (right), where a few ceramic tubes, wires and the wire guides are visible.

Table 6.1: Labeling scheme and abbreviations for each electrode in the trap structure.

Component	Label	Quantity
Steerer	S	3 (4 quadrants, whereas two neighboring are shorted to each other)
Drift tube	DT	2
Gate	G	2
Trap electrode, non-segmented	T	26 (starting with T1 with the first electrode closest to the ion-injection side)
Trap electrode, 2-fold segmented	D	2 lenses with D1a and D1b being the first lens *
Trap electrode, 8-fold segmented	O	8 *

* Here, the 2-8-2 section on the downstream side is shorted to a 1-1-1 configuration.

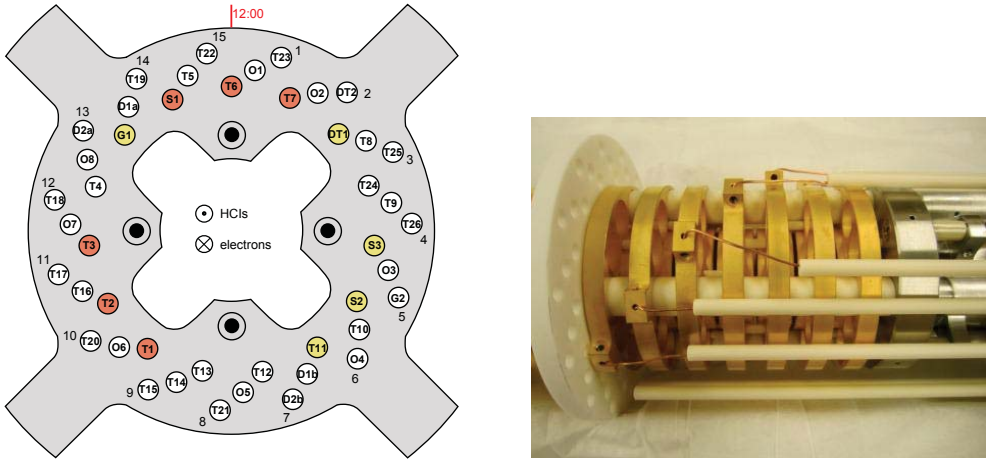

Figure 6.15: Left: Wiring diagram and labeling of each electrode and the corresponding feed through. Table 6.1 explains the abbreviations. Right: Picture of a section of trap electrodes displays how the wiring is achieved.

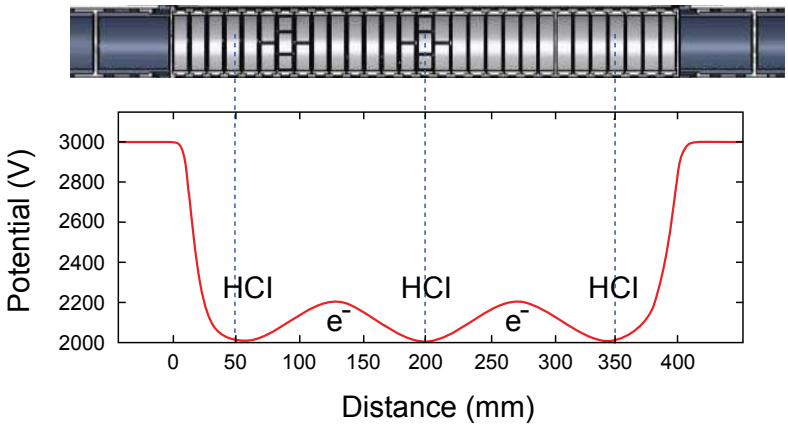

Figure 6.16: A possible nested trap configuration of CPET. In the upper part, a section of the electrode stack of CPET is displayed. The diagram below shows the electric potential (only indicative) on the longitudinal axis. Simultaneous trapping of positive and negative charges can be achieved in the nested hills and wells.

6.5 Electronics and voltage switching schemes

6.5.1 Trap potentials

For the implementation of electron cooling nested potentials are crucial to facilitate trapping of both negative and positively charged particles. A possible nested trap configuration of the CPET is shown in Figure 6.16. The CPET trap structure will be floating on a 2 kV potential to match the ions' transport energy. The gate electrodes are switched between 2 and 3 kV and the nested wells (for trapping ions) and hills (for trapping electrons) are created by applying voltages to the correct electrodes. Figure 6.17 displays an overview of the potentials used in simulations in this thesis and a comparison to the 'real' potential applied to the electrodes. To form a potential similar to the one shown in Figure 6.17 (left), one can apply different voltages to five electrodes, e.g. 100 V at electrode 1 and 5, no voltage at the center electrode, and 25 V at electrode 2 and 4. The effective potential (green) that is then seen by the charged particle is similar to a harmonic potential (red).

Simulations in the Particle-In-Cell code performed by the HITRAP group, see Figure 6.17 (middle and right) [170], show that a few volts is already sufficient to efficiently trap an ion cloud of 10^5 U^{92+} ions. Going to higher voltages has the advantage that the potential deformation (difference between ions in the trap and empty trap) becomes much less significant for higher

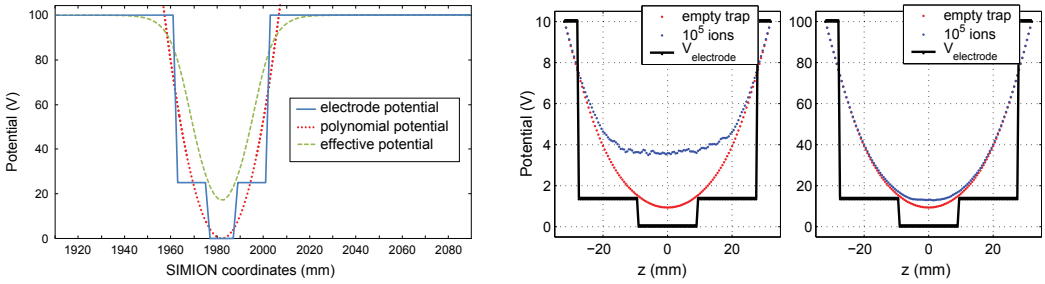

Figure 6.17: Left: Overview of different potentials used in the simulations studies in this thesis. Potential applied to the CPET electrodes (blue), a simple harmonic potential (red), and the effective potential as calculated by SIMION (green). Middle and Right: Particle-In-Cell Code simulations for the HITRAP cooler trap [170].

potential wells. Highly charged ions sit deeper in the potential well than singly charged ions.

As discussed in Section 6.2.1, sympathetic cooling with charged particles requires modulation of the potentials in order to manipulate the trapped particles. These operations can be performed on both electrons and ions and are done using time dependent potentials applied to the trap electrodes. It is very important not to introduce additional energy and heating to the particles while moving them around. An adiabatic transfer of charged particles is required, i.e. the transport time is much larger than the time of an oscillation period.

Simulations to move charged-particle bunches in a potential well from one end of the trap to the other have been investigated for electrons. For simulations performed in 1D and 3D [172], it was found that $N = 100$ switching steps (corresponding to a shift of the trapping potential by $\Delta z = 3$ mm) limits the energy gain of the electrons to the order of eV. These are realistic numbers which should be addressable using special electronics, which will be discussed in the next section (Section 6.5.2).

6.5.2 Electronics

The CPET loads and extracts various species of particles (highly charged ions, electrons, protons) during a macro-cycle of its operation, which is repeated at the 100 ms to 10 s time scale. For the operation of the trap and the surrounding beam optics (see Chapter 7) three different types of drivers are needed to supply time-dependent voltages to the electrodes:

- Fast (100 ns) bi-level switches: Used for the trap end-gates, which will allow for fast trapping and extraction of particles. These trap gates will be switched quickly between two preset potentials.

- Slow (1 ms) bi-level switches: Most beam optics outside of the trap region as to be presented in Chapter 7 (steerers, drift tubes, Einzel lenses, extraction anode for electron gun) need to be optimized for each type of particle passing through during the macro-cycle. For example, proton cooling would require protons (from a source upstream) and HCI from the EBIT (also upstream) to pass through the same set of injection optics. As a result, the Einzel lens used to focus the particles through the magnetic-field gradient of the cooler trap might have to be tuned to different settings for optimal efficiency. However, the voltage switching in this case could occur at much longer (e.g. 1 ms) timescales.

- The trap electrodes between the two trap gates: These electrodes need to be adjusted continuously, to obtain a smoothly varying, time-dependent potential inside the trap. The implementation is radically different from the fast and slow bi-level switches, requiring an arbitrarily multi-channel, programmable function generator.

A schematic of the CPET electronic system is displayed in Figure 6.18, showing the trap structure and the connected switches and amplifiers as well as the switching scheme for electron cooling. The electrodes outside of the trap will support two different voltage settings and are supplied by bi-level Behlke HV-switches. The trap electrodes will be floated on a 2 kV potential with an additional 0 to 200 V applied by arbitrarily programmable switches to form the trapping potentials. There are two advantages to the floating: First, there is no need to adjust the MPET injection parameters to account for the presence of CPET. Second, fluctuations in the voltage of the platform will affect every channel in the same way and will not cause potential fluctuations across individual channels and electrodes.

The switches and amplifiers are configured and triggered using arbitrary waveform generators (AWG) and multi-channel, programmable pulse generators (PPG). In addition, Figure 6.18 shows sample potentials for stages of the CPET cycle for electron cooling with electron injection (top), HCI injection (middle), and the final extraction scheme (bottom).

The CPET electronics system will use fast bi-level high-voltage HV-switches and programmable amplifiers. The switches drive the drift tubes and the trap gate electrodes. The trap gates have to be switched fast to close the trap and confine the ions once the ions have entered the trap. The drift tubes can be switched between two different voltage settings depending

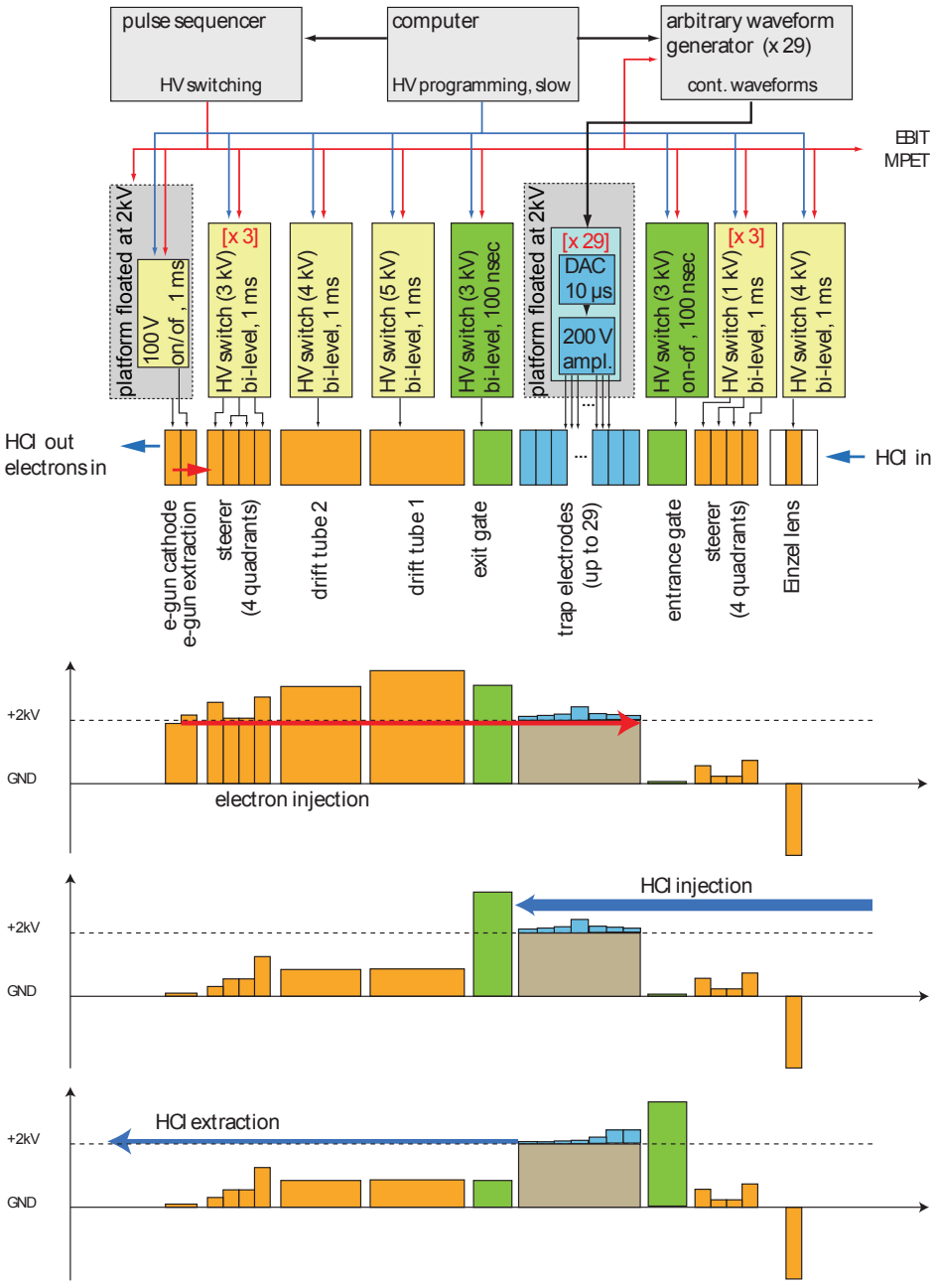

Figure 6.18: The switching scheme and a simplified operation cycle for electron cooling. This figure was produced for [167]. The upper part shows the controls, power supplies and actual electrodes (not to scale). The requirement for the timescale of the high-voltage switches is indicated. The graphs at the bottom show sample potentials for the CPET cycle for electron cooling.

on the type of particles traveling through (e.g. HCI will exit the trap on the side where the electrons are injected). The amplifiers will be arbitrarily programmable to supply 0 to 200 V. All amplifier channels will be floated together on a 2 kV platform, which matches the 2 kV kinetic energy that is given to the ions from the EBIT.

In order to shape different potentials in the trap (e.g. for loading and extracting particles or to set up nested potentials) the amplifier has to be programmed to apply different potentials to the trap electrodes with precise timing (see also the schematic of the operation cycle shown in Figures 6.3 and 6.6). To accomplish this, the programmable power supply is equipped with an internal memory large enough to store several thousand data points. This should provide roughly 50 switching operations, thus moving the charged particles without introducing additional heat. A prototype of a programmable power supply is being designed that will allow potential changes on the order of 10 ns between two voltage settings. The capabilities of a prototype amplifier, similar to the one that is under construction at TRIUMF, have been tested (see [172]).

A 32-channel programmable pulse generator (PPG) has been developed at TRIUMF to provide experimental timing. Each channel provides trigger pulses with well-defined timing and width, which will be used to trigger the HV switches. The module can be triggered externally or by its own internal clock which will be used for the initial test setup in Chapter 7. In the future, the PPG cycle for the on-line CPET system will be triggered either by the RFQ, EBIT or the MPET PPG, enabling synchronization across the whole system.

6.6 Electron source

The electron source will produce the electrons required for the cooling of HCI. An electron cloud with density of at least $n_e = 10^7$ cm^{-3} is envisioned. In the CPET system the electron source will be placed off axis outside the magnet in the magnetic fringe field. The electrons are then steered onto the magnetic-field axis using an $\vec{E} \times \vec{B}$ drift.

For CPET purposes a field emission array (FEA) is suitable. However, for initial testing and diagnostics a field emission tip (FET) will be used as an electron source. These tips have been fabricated at NSCL using electrochemical etching of a tungsten wire in a NaOH solution. Pictures in different image magnifications are shown in Figure 6.19 (left and middle), and their operating mode is described in Section 7.2. The right of Figure 6.19 shows a picture of the FEA from SRI International [173] that will be used at a later

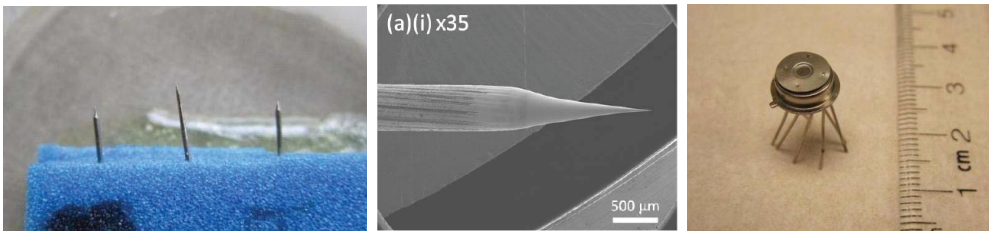

Figure 6.19: Pictures of the electron sources. Left: field emission tips. Middle: A scanning electron microscope image with a factor of 35 magnification. Right: Picture of a field emission array for comparison.

stage. It has a 1 mm-diameter array consisting of 50,000 emitter tips on a 10-30 Ω cm silicon substrate. The tips are fabricated on a square silicon chip, and mounted on a TO-5 header (as seen in Figure 6.19 (right)) to facilitate electrical contacts and handling. Tests of the cathode can be performed using a 60 Hz pulse driving voltage. The FEA will allow to produce 100 mA of pulsed electron beam and a few mA in continuous mode.

6.7 Proton source

For proton cooling, a proton source will be mounted upstream on the ion-injection side of CPET, in the TITAN switchyard. To deliver 10^8 protons in a single bunch (i.e. with a length corresponding to the round trip time in the trap), a source current of 1.6 μA ($\leq$ 10 eV energy spread) is required. A complete plasma ion source was purchased from Colutron for this purpose [174], which can be used as a surface ion source as well. The Colutron ion source is a simple low voltage arc discharge source capable of producing high quality ion beams of several μA with very low energy spread (0.1-0.2 eV) [175]. This corresponds to a thermalized plasma with a temperature of about 1000°C.

If the protons from the source require additional cooling, this can also be accomplished in CPET. For example, protons trapped in a nested well in the CPET trap structure could be pre-cooled using electron cooling (see Section 6.2.1) prior to HCI injection.

6.8 Environmental requirements

To facilitate sympathetic cooling in a cylindrical Penning trap, requirements are set to the magnetic-field strength and homogeneity as well as the vacuum that is required inside the vacuum vessel that is housing the trap structure. These two requirements are discussed in the following Subsections 6.8.1 and 6.8.2.

6.8.1 Magnetic field

The requirement for the strength of the magnetic field is set by the need for electron self-cooling via synchrotron radiation at sub-second time-scales. In addition, the homogeneous region of the magnet needs to be sufficiently long to accommodate extended bunches of HCI from the EBIT and the large number of electrodes required to implement the nested potentials. Furthermore, the close proximity of CPET to the TITAN MPET and other magnetic-field sensitive experiments in the ISAC hall mandates an actively-shielded magnet. To fulfill these requirements, a 7-Tesla superconducting solenoid manufactured by Cryomagnetics Inc. [176, 177] was purchased. In the center of the magnet the field homogeneity is $\delta B/B = 10^{-5}$ in a cylindrical region of 100 mm length and 50 mm in diameter, while along the axis the field is constant to $\delta B/B = 10^{-3}$ over a region of 400 mm. In the 7-Tesla field, the electron self-cooling time constant is ≈ 0.07 s (see Section 6.2.1).

Mapping of the magnetic field has been performed to establish the alignment of the magnetic-field axis with respect to the center axis of the cryostat bore, which is a crucial information for the alignment of the vacuum pipe inside the magnet. An axial Hall probe was used to carry out the measurements in steps of 2.54 cm. Figure 6.20(a) displays the magnetic-field strength inside the magnet, as well as the location of the 40 cm trap structure in the center. Radial field mapping was performed using a radial Hall probe mounted in a rotating cylinder which mocks the trap structure vessel. Figure 6.21 shows the equipment and mounting of the Hall probe to allow for a precise three-dimensional field mapping. The radial mapping showed that the magnetic-field axis does not coincide with the magnet bore axis (see Figure 6.20(b)). This is very crucial especially for the beamline alignment and the injection of light, charged particles, e.g. electrons. The offset on the south-pole face of the magnet is $x_s = -2.1$ mm and $y_s = -4.5$ mm, and on the north-pole face $x_n = 0.8$ mm, $y_n = 3.9$ mm.

The alignment of the magnetic-field axis with the beamline is accomplished using a precise tube holding structure mounted on the faces of the magnet. Figure 6.22 shows the south-pole and north-pole mounting brackets.

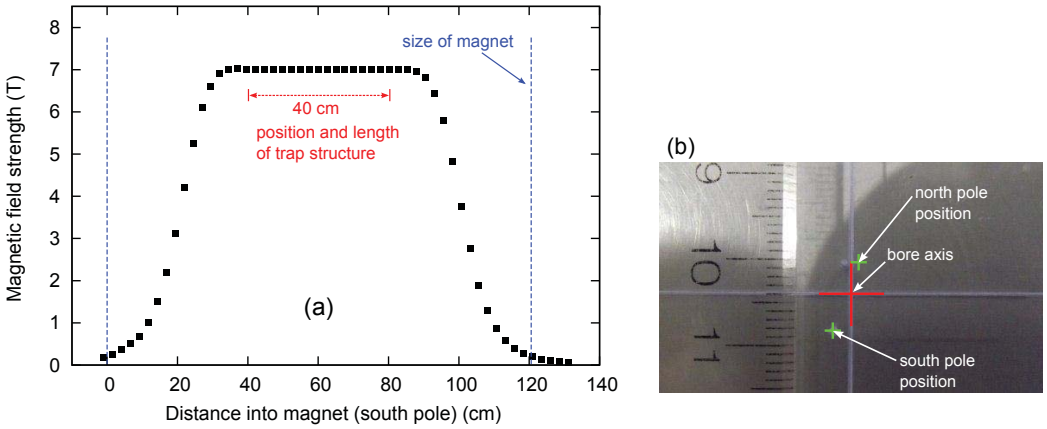

Figure 6.20: (a) Measurement of the magnetic-field strength along the magnet bore axis. The size of the magnet, and the position of the trap structure are indicated with blue and red dashed lines, respectively. (b) With the help of the radial field mapping it was established that the magnet bore axis (red cross) and field axis (green crosses) are not identical. The difference is shown, marked on acrylic glass windows that can be mounted on the faces of the magnet.

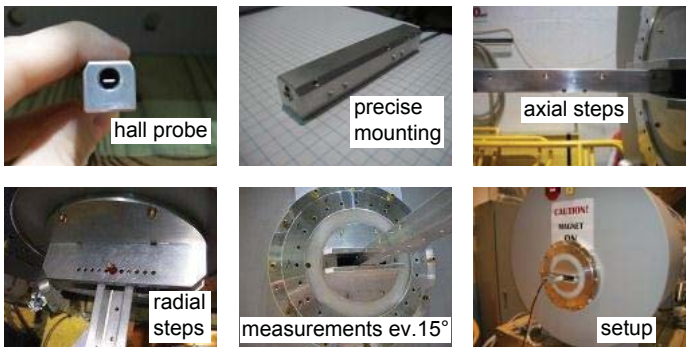

Figure 6.21: Magnetic-field-mapping equipment, manufactured for the purpose of axial and radial field mapping.

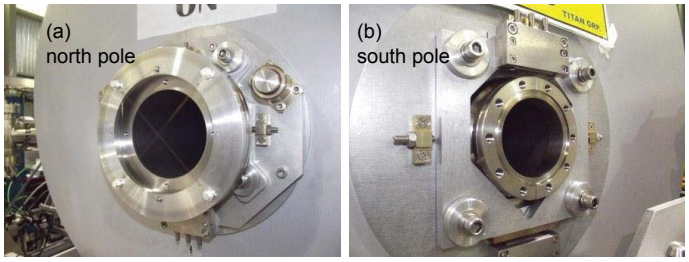

Figure 6.22: Alignment structure for the CPET tube inside the magnet: (a) north pole, (b) south pole.

6.8.2 Vacuum

The use of HCI places strict requirements on the vacuum quality, due to the increased probability of charge-exchange collisions with the background gas. The collision rate R for a charged ion in a background gas of density n is given by $R = nv_{rel}\sigma$, where the charge-exchange cross section σ can be estimated from [178]. For our purpose, the relative velocity v_{rel} between the collision partners is dominated by the ion motion, and using pressure instead of density, we obtain a charge-exchange collision rate of

$$R = \sqrt{2c^2 q \frac{K/q}{mc^2}} \cdot \frac{p}{kT}\sigma, \tag{6.15}$$

where K is the kinetic energy of the ion, m its mass, q its charge, and p and T are the pressure and temperature of the background gas, respectively. Assuming a $q = 20+$ ion of mass 50 u with $K \approx 100\,\mathrm{eV}/q$ and a charge-exchange cross section of the order of $1{\cdot}10^{-13}\mathrm{cm}^2$ [178], one obtains a collision rate of ≈ 2 Hz at room temperature and a pressure of 10^{-10} Torr. This defines the minimum requirement for the vacuum. Clearly, a pressure approaching 10^{-11} Torr is desirable.

The vacuum system (see Section 7.1.2 and Figure 7.6) has large turbo pumps (with a pumping speed of 500 l/s for nitrogen) sitting on the crosses at each side of the trap structure. While the pumping speed is given by the conductance and is higher close to these pumps, the pumping speed in the center of the trap structure is limited due to the surrounding material, as well as the tube diameter. To increase the pumping speed and decrease the achievable vacuum, an additional technique is used: The inside of the vacuum vessel has been coated with non-evaporable getter (NEG) material

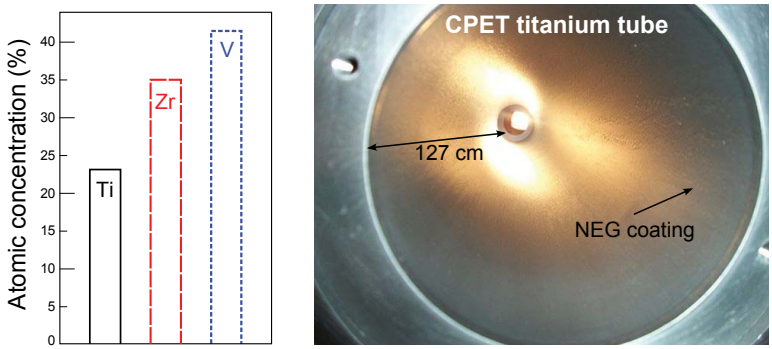

Figure 6.23: (a) The surface metallic composition of the NEG-coated titanium vessel that houses the trap structure. (b) Picture of the NEG-coated tube.

to increase the pumping speed in the trap region [179]. An X-ray photoelectron spectroscopy analysis of our coated vacuum vessel was performed [180] to identify the surface metallic composition of the NEG material (see Figure 6.23(a)).

The NEG coating needs to be chemically activated to act as an active pump. The temperature at which the activation sets in is $\approx (100 - 150)°C$, achieved during a baking time of 24 hours. Some experimentally determined features of the NEG coating are listed in Table 6.2. Tests with gold- and silver-plated copper test-electrodes have been carried out and no discoloration indicating any gold evaporation was visible. After activation, the NEG film acts as a conductance-free distributed pump inside the chamber. The NEG film also acts as a gas barrier, which reduces thermal out-gassing and further enhances the vacuum. These features are ideal for very narrow, conductance limited chambers, which cannot always be efficiently pumped by ordinary means. Experimental tests, carried out in several high energy machines and synchrotron radiations facilities (e.g. CERN [179], ESRF [181]) have confirmed the benefits of NEG films in terms of better vacuum, longer beam life time and stability, simplified machine design, reduced conditioning time and overall improved machine performances. A picture of the NEG-coated tube is shown in Figure 6.23(b).

Vacuum performance tests of the titanium vacuum vessel that houses the trap structure have been carried out. Baking of the empty vessel for several days at $\approx 200°C$ resulted in a pressure of $p \leq 1.0 \cdot 10^{-11}$ Torr (see Figure 6.24(b)), reaching the limit of the vacuum gauges. Loading the vessel with different materials such as Kapton, ceramic tubes etc. along with careful baking lead to similar low pressures. A picture of the baking station can be

Table 6.2: Investigations of the titanium tube coated with the non-evaporative getter (NEG) material, which will be housing the trap structure. Test electrodes are mounted inside.

NEG coating	Comments
Activation temperature	between $\approx (100-150)$°C, while baking for 24 hours
Achieved pressure	$\leq 1.0 \cdot 10^{-11}$ Torr (limit of gauge controller)
Active time	NEG coating remained active for more than 30 days without any trend of saturation. Total active time not investigated so far.
Partial pressures	Pressure dominated by H_2, other gases (H_2O, N_2, CO_2) present in very negligible amounts ($\approx 10^{-12}$) as tested with a residual-gas analyzer.

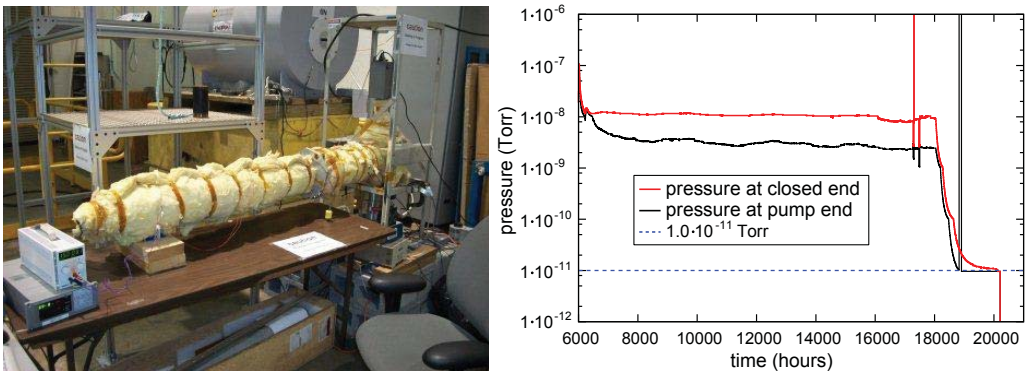

Figure 6.24: (a) Picture of the baking test station of the CPET tube. (b) The CPET tube is coated with NEG and a plot of pressure over time shows the reachable pressure. The pressure gauges only read pressure down to $1.0 \cdot 10^{-11}$ Torr (dashed blue line).

seen in Figure 6.24(a).

The overall performance of the NEG coating is satisfactory with the requirements for vacuum. Housing the trap structure in the coated vacuum vessel will allow the achievement of the UHV conditions required for storing HCI without charge exchange for the duration of the cooling process (several hundreds of ms). Further investigations can be found in Section 7.1.2. For the first part of the initial CPET setup no baking of the trap structure is foreseen. It is planned at a later stage once the base pressure is determined, which can be reached without baking.

Chapter 7

CPET Commissioning

In order to perform initial testing of CPET without disturbing on-line work at TITAN, CPET has been mounted off-line adjacent to the existing TITAN MPET beamline. The so-called off-line setup contains optics and diagnostics needed for studying electron and ion injection as well as the two HCI cooling methods. Once off-line testing is completed, CPET can be inserted into the permanent position in the TITAN beamline using a rail system. This chapter discusses the design and implementation of the off-line setup and presents first-stage experiments.

7.1 Off-line setup

The off-line setup is located adjacent to the TITAN MPET beamline. This location is advantageous as it is very close to the future on-line position (see Section 7.3). Therefore, all of the electrical equipment can be installed in its final location, in electronics racks located with the rest of the TITAN equipment. Additionally, equipment used at TITAN can easily be shared during the commissioning phase. The CPET off-line setup incorporates the equipment to study the two cooling techniques and to implement reasonable switching cycles and duty cycles for a full cooling scheme.

7.1.1 Beamline design

The CPET off-line setup was designed to facilitate investigations of cooling techniques, including particle injection and trapping. The Solid Works drawing of the off-line setup can be seen in Figure 7.1 and a picture in Figure 7.2. The orientation is as follows: The electron source is located downstream of the CPET magnet and is referred to as the electron-injection side. The ion-

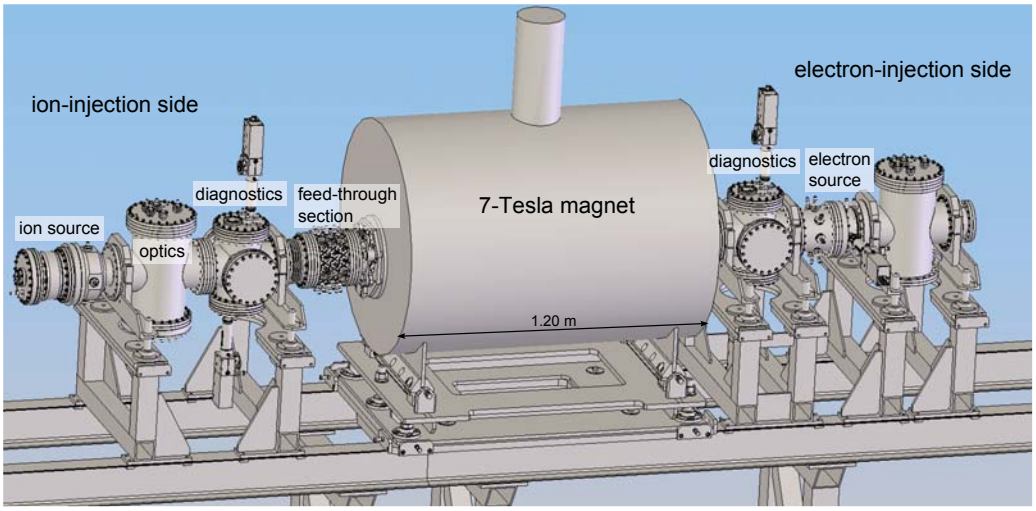

Figure 7.1: Solid Works drawing of the CPET off-line setup. The left hand side shows the ion-injection beamline, the right hand side shows the electron-injection beamline.

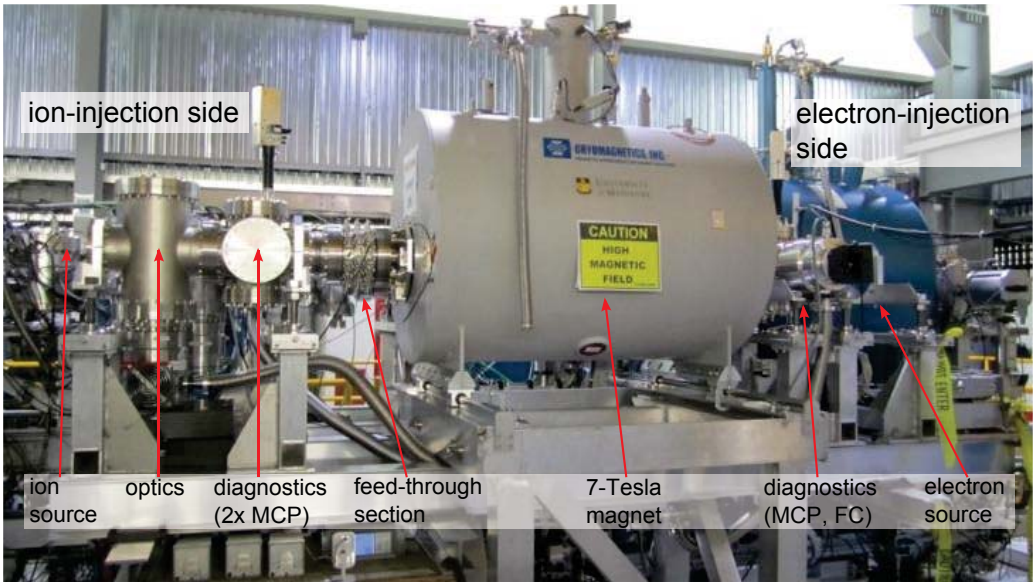

Figure 7.2: Picture of the CPET off-line setup with its location adjacent to the MPET beamline. On the left the ion-injection beamline, and on the right the electron-injection beamline can be seen.

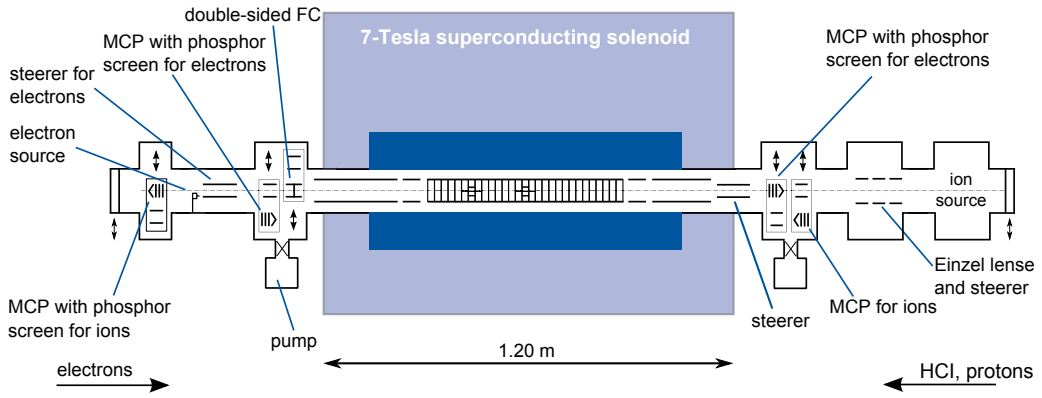

Figure 7.3: Outline of the CPET off-line setup, located adjacent to the TITAN MPET beamline (not to scale). Displayed are optics and diagnostics that are used. Electrons are injected from the left, protons and HCI from the right.

injection side, which corresponds to the side from which radioactive ions will enter the trap structure in the future, is located on the upstream side of the CPET magnet. In both figures (Figures 7.1 and 7.2) the beamline frame and support structure are visible.

Extensive SIMION simulations have been carried out to define and place electrostatic beamline optics and diagnostics to inject and extract all different charged particles (i.e. HCI, SCI, protons, and electrons). A sketch of the resulting setup can be seen in Figure 7.3, which shows the location of the sources and diagnostics for the electron-injection and ion-injection sides, as well as the trap electrodes. The purpose of these elements will be described in the following sections.

The diagnostic elements employed in the setup are Faraday cups and microchannel plate (MCP) detectors. Electrostatic ion optics elements include cylindrical and plate steerers, drift tubes, lenses, and extraction optics for the electron and ion sources.

Two different types of MCPs are placed in the setup. Three MCP assemblies will have a phosphor screen (see Figure 7.5[E, L, M]). The fourth MCP assembly has no phosphor screen, and will be used as a position-sensitive detector (see Figure 7.5[B]). Here, the signal on the MCP anode is read-out at all four corners which gives information about the position of the incident particles.

A double-sided Faraday cup has been designed which will allow particle detection from either side. It consists of a high-purity oxygen-free copper

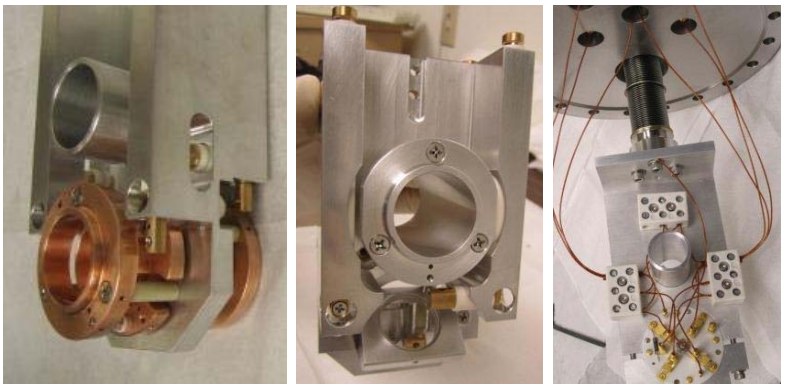

Figure 7.4: From left to right: Pictures of Faraday-cup, MCP-with-phosphor-screen, and position-sensitive MCP assemblies for the CPET off-line setup. Each of those assemblies is mounted on a linear motion feedthrough. The actuator has two positions, which allow for the insertion of either a detector or a drift tube into the beam line.

cylinder and lenses mounted on either side. The lens repels electrons produced inside the cup. A picture of the Faraday-cup assembly is shown in Figure 7.4(left). The unit consists of the double-sided Faraday cup and a drift tube, which are attached to a linear motion feedthrough.

Electron-injection

Figure 7.3 displays a schematics of the optics for electron manipulation and detection. A Solid Works cut-away view of the electron-injection side is shown in Figure 7.5 where the whole off-line setup is presented. The electron-injection side is shown on the left side with labels A to G, and the ion-injection side on the right with labels J to O, respectively. The labeling scheme is listed in Table 7.1. Removed from the display is the trap structure, for which a detailed discussion can be found in Chapter 6.

For the process of electron injection and extraction from the trap the following units in Figure 7.5 are needed: [C, D, E, F, G, J, and L]. Electrons are produced in an electron source at position [C], which will either be a field-emission array (FEA) or field-emission tip (FET). For initial testing the electron source is on-axis, but it can be mounted off-axis. It allows for a precise mounting and in the off-axis version, for a shielding towards the ion

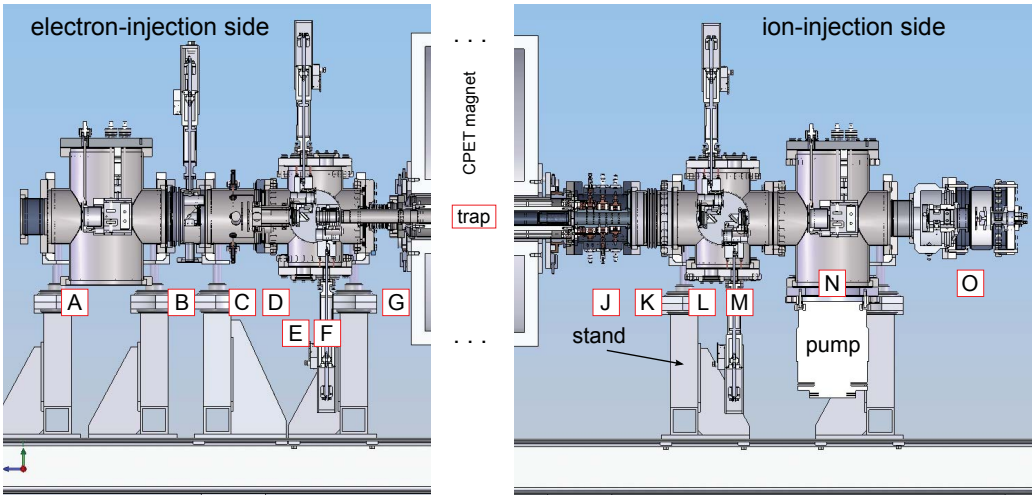

Figure 7.5: A cross section of the CPET off-line setup with its diagnostics and ion optics on the electron-injection (left) and ion-injection side (right). Labels identify the different units in the setup and are displayed in Table 7.1. A more detailed description can be found in the text.

beam passing through. A fixed position allows for a precise mounting, and the off-axis version shields the source from the passing ion beam. An extraction lens is placed in front of the electron source to accelerate the electrons and reduce the transverse emittance of the beam. The extracted electrons then pass through a steerer at position [D]. SIMION simulations show that a cylindrical shape is preferred, so a quad-split cylindrical steerer has been implemented. For off-axis mounting of the electron source, the steerer (in combination with the fringe field of the magnet) will use an $\vec{E} \times \vec{B}$ drift to bring the electrons on-axis for injection. Prior to injection, electron beam flux and position can be monitored with an MCP detector at position [E] plus phosphor screen. Electron current readings can be made with a double-sided Faraday cup at position [F]. A drift tube is mounted in the bellows section (label [G]) before the magnet, which is connected to the long drift tube in the trap section. It can be used to accelerate the electrons through the magnetic-field gradient into the trap. Label [J] indicates the complex structure of the electrical feed-through section of the trap electrodes. Electrons can also be extracted onto the ion-injection side and monitored with an MCP unit with a phosphor screen at position [L]. This MCP can be used to detect whether the electrons are on- or off-axis.

Table 7.1: Labeling scheme of the different elements in the CPET off-line setup in Figure 7.5.

Label	Module
A	X- and y-steerers, and lens assembly for manipulating the ion beam going to the MPET
B	Position-sensitive MCP unit
C	Electron source with extraction optics
D	Quad-split cylindrical steerer
E	Unit with MCP with phosphor screen and drift tube
F	Unit with double-sided Faraday cup and drift tube.
G	Drift tube in bellows section which is connected to the trap drift tube
J	Electrical feed-through section of the trap structure.
K	Bellows section
L	Unit with MCP with phosphor screen and drift tube facing towards the trap
M	Unit with MCP with phosphor screen and drift tube facing towards the ion source
N	X-and y-steerer and lens assembly for ion-source beam optimization
O	Ion source with extraction optics and steerer-lens assembly

Ion-injection

For the process of ion injection and extraction from the trap the following modules in Figure 7.5 can be used: [O, N, M, L, K, J, F, B, and A]. A surface-heated ion source (label [O]) has been designed to produce singly charged ions (SCI) or protons. An additional plasma ion source has been purchased from Colutron [174] (see Section 6.7), which will also provide SCI and protons. The Colutron source is able to deliver up to 10^8 protons in a single bunch, with a source current of ≈ 1.5 μA and an energy spread of less than 10 eV [175]. Both source modules contain integrated extraction optics with focusing lenses and x-, y- steerer plates. Between sections, labeled [O] and [N], there is an aperture installed on the flange to allow for differential pumping to maintain the pressure at the trap region. An Einzel lens and steerer assembly is located in the cross at position [N] to allow for additional focusing and steering of the ion beam prior to injection into the trap. Moreover, the steerer could function as a 'dump' for the ion beam by working as a beam gate. To monitor the ion flux and beam location, an MCP with a phosphor screen [M] is placed before the magnet. The ions then pass through the drift tube at position [L], the bellows section at position [K], the electrical feed-through section at position [J], and finally enter the trap section. Ions can be extracted in both directions while monitoring the ion beam in reverse mode on the MCP at position [L] or in forward mode on the Faraday cup at position [F]. After passing through drift tubes in modules labeled with [G, F, E, D], the ion beam can be monitored on the electron-side MCP at position [B]. This MCP will have a resistive anode to allow for position-sensitive detection. Module [A] will not be in place for the CPET off-line setup. It is designed for the on-line setup (see Section 7.3) to provide steering and focusing of the cooled HCI beam prior to injection into the MPET for the mass measurement.

7.1.2 Vacuum system

The vacuum system of the CPET off-line setup is designed to fit into the existing TITAN vacuum system. For now, the CPET vacuum system will be self-containing, and will be integrated with the TITAN beamline when off-line testing is complete (see Section 7.3). Figure 7.6 shows a vacuum-system schematic. The system contains four 500 l/s turbo pumps, a smaller 80 l/s turbo pump, a multitude of valves, and gauges (convectron and ion) to read out the pressure in each vacuum section. Convectron gauges can detect pressures from one atmosphere ($\approx$760 Torr) to 10^{-3} Torr, whereas the ion gauges can detect pressures down to $\approx 1.5 \cdot 10^{-11}$. As discussed earlier, the titanium tube housing the trap structure is coated with a non-evaporative

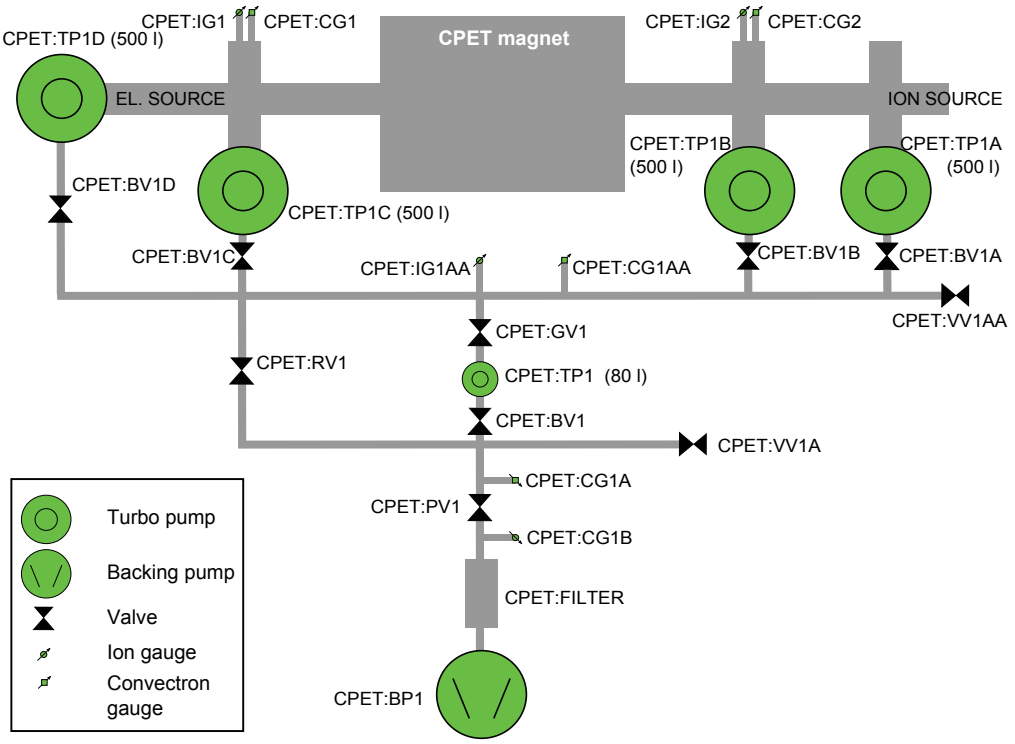

Figure 7.6: The CPET off-line vacuum system with its four turbo pumps (TP1A-D) with a pumping speed of 500 l/s, a smaller turbo pump (TP1) of 80 l/s speed, a backing pump (BP1), its many valves, and gauges to read out the current pressure. The valves are named by their purpose: e.g. BV for backing valve and VV for venting valve.

getter (NEG) material which can be activated to work as an active vacuum pump. Section 6.8.2 discusses the vacuum requirements and the NEG coating in more detail.

7.2 Initial experiments

The off-line stand was designed in order to test optics and diagnostics, as well as for preliminary studies of cooling techniques. These goals will be achieved in a series of sequential steps. First, electrons will be injected, trapped and extracted. Subsequently, singly charged ions will be trapped and cooled using electrons as a coolant. After characterizing the process for electrons, the same tests will be attempted with protons. Finally, isobaric separation

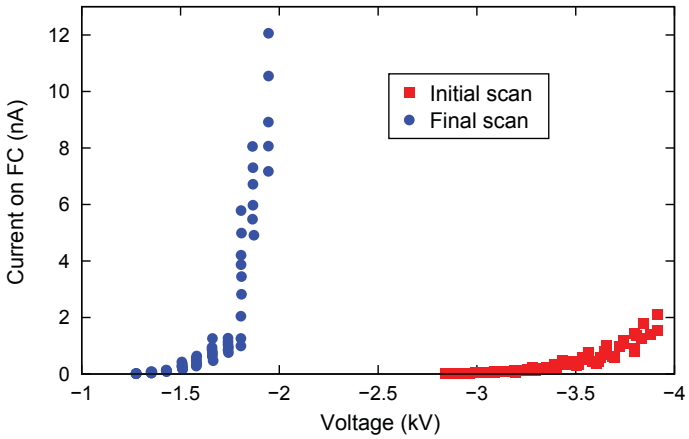

Figure 7.7: First electron production for injection into CPET. The voltage applied to the FET is scanned and the average field-emission current produced by the tip is read-out at a Faraday cup. The two data sets correspond to measurements taken after the FET first fired and after conditioning for 1 hour.

methods will be investigated, for which an aperture is placed between the gate electrode and the last trap electrode. Once the CPET system is sufficiently understood, it can be moved into the on-line position in the TITAN beamline (see Section 7.3). First results of the commissioning process will be discussed in this section.

Before the electron-injection process can be characterized, several steps need to be fulfilled. An alignment of the beamline components (see Figure 7.5) was achieved using a surveying telescope. The magnetic-field axis, trap tube (see description in Section 6.8.1), and main beamline crosses were aligned and fixed in their final positions. Since the magnet is mounted on rails it can easily be moved in and out of position, allowing for the tube to be inserted.

For the initial setup, a reasonable vacuum ($\approx 10^{-9}$ Torr) is required, which should be achievable without special steps. Therefore, baking of the vacuum tubes and activation of the NEG pump will be performed at a later stage. Each vacuum vessel has been tested for leaks, and modifications have been implemented to counter possible leaks.

For initial electron tests, a decision was made to implement the field-emission tip (FET) as an electron source (see Section 6.6 for more details) due to its relative simplicity. An FEA will be installed at a later stage. First commissioning experiments included the conditioning of the FET, which was

mounted on-axis. A vacuum of $6.9 \cdot 10^{-9}$ Torr was achieved in the electron-injection beamline after one week of pumping without any baking, and the tip was biased to a negative potential between a few hundred volts and a few kilovolts. The large electric field at the sharp tip of the FET enabled conduction electrons to penetrate the potential barrier at the surface of the tip after which they were accelerated away from the tip by the electric field. A grounded Faraday cup at position [F] in Figure 7.5 was used to collect the electron beam, and the current was monitored with an electrometer. The voltage required to initiate field emission was recorded, and a scan of field-emission current as a function of applied bias potential was performed. for conditioning, the tip was then operated at ≈4 nA for one hour, and the scan of field-emission current versus bias potential was repeated. The current and accordingly the number of electrons is shown in Figure 7.7 for both measurements taken at different times. The voltage required to produce a given field-emission current decreased over time and became stable after a one-hour conditioning time. Between the initial and final scan a difference is shown attributing to physical changes in the geometry of the tip arising from sputtering or melting of the tip, respectively.

For off-line tests the trap structure will not be floating at 2 kV (foreseen at a later stage), but rather be on ground potential. Figure 7.8 shows the potential distribution along the CPET electrodes. The harmonic potential well is formed by applying different voltages to the electrodes from three power supplies: V_1, V_2, and V_3. For this experiment the electrodes are bridged by a resistor chain, defining a voltage at each electrode of

$$V(z) = V_t \cdot \frac{2z^2}{L_t}, \tag{7.1}$$

where $V_t = |V_1 - V_2|$ is the well depth during electron injection, z the axial distance from the trap center, and L_t is the effective trapping length. The latter can be varied by choosing a different number of electrodes to form the trap potential.

The electron injection and accumulation cycle as can be seen in Figure 7.8 includes the following steps:

1. Prepare a harmonic potential with V_{1-3}, as can be seen by the solid red line in Figure 7.8.

2. Turn on an electron beam of ≈ -1056 V from the FET.

3. Open the potential barrier at V_1 (i.e. $V_1 = -1050$ V) for electron injection (dotted green line). The electrons are injected and get reflected at the potential barrier V_3.

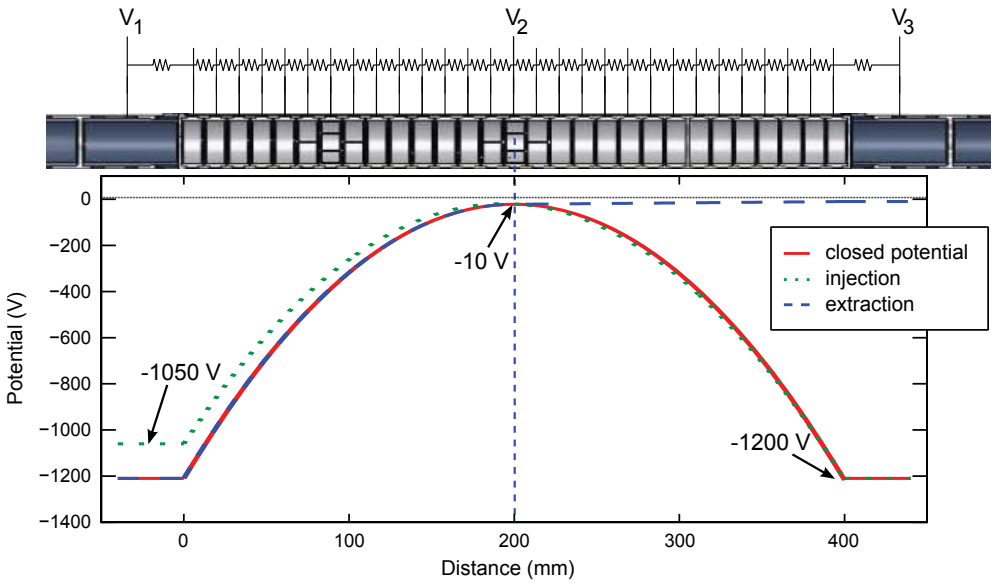

Figure 7.8: Potential distribution along the CPET axis during injection (dotted green line), trapping (solid red line), and extraction (dashed blue line) of electrons.

4. The potential barrier is switched to $V_1 = -1200$ V again, and electrons are trapped. Electrons now cool via emission of synchrotron radiation with a time constant $\tau_c \approx 0.07$ s for a magnetic field of $B = 7$ T.

5. After a trapping time τ_t the electrons are extracted by switching V_3 from -1200 V to 0 V (dashed blue line). The MCP with a phosphor screen at position [L] is biased to a positive voltage and the electrons are monitored.

Here V_1 and V_3 are each controlled by a box consisting of two Pico power supplies and a Behlke switch.

Accumulation of more than 10^{10} electrons within a fraction of a second has been demonstrated [182]. The trapping time τ_t can be used as an indication of the quality of the magnetic-field alignment, as a better alignment results in a longer electron lifetime in the trap.

7.3 Off-line to on-line transition

Once the CPET system is sufficiently understood, it can be moved into the on-line position in the MPET beamline. Almost the entire CPET off-line

setup will move between the switchyard and MPET as indicated in Figure 6.1. Since the off-line setup was designed to fit in the TITAN beamline, no additional modifications have to be made before the off-to-on-line transition occurs. The whole section will be replaced with the CPET setup and more diagnostic tools will be available for on-line beam manipulation.

To allow for the whole CPET off-line setup (without the ion source, module [O] in Figure 7.5) to be placed between the switchyard and MPET, the TITAN platform was extended. A length of 91.5 cm has been added to the existing holding structure. Figure B.1 in the appendix shows the differences between the current switchyard-to-MPET beamline and the future one, including CPET and all its diagnostics and optics.

The transition of the CPET off-line setup to its on-line position will start when the system is understood and efficient cooling cycles have been implemented. Once CPET has been fully integrated into the existing TITAN setup, full testing can begin. HCI with charge q will be extracted from the EBIT to ground potential with a nominal energy above 2 kV$\cdot q$ such that the CPET trap structure, which will float on a 2 kV platform, can accept the HCI bunch with the lowest possible kinetic energy.

Chapter 8

Conclusion and Outlook

This thesis covered two main topics. First, mass measurements of highly charged, neutron-rich nuclides have been performed for the first time and their impact and relevance to nuclear structure and nuclear astrophysics have been investigated. Second, the design of the Cooler Penning Trap (CPET) has been accomplished, which will strengthen the highly charged ion (HCI) mass-measurement program at TITAN. In addition, a complex off-line setup to investigate the cooling processes has been designed and constructed, and commissioning experiments have been performed.

Masses of ^{94,97,98}Rb and $^{94,97-99}$Sr have been measured to a relative mass precision better than $4.5 \cdot 10^{-8}$ (corresponding to $\delta m = 4$ keV/c^2) using the Penning-trap mass spectrometer TITAN. This thesis produced accurate and precise mass measurements of highly charged ions in the charge state $q = 15+$ and the first direct mass measurement of ^{98}Rb. For the first time, on-line produced isotopes were measured in a Penning trap with such a high charge state.

Nuclear structure properties, such as the neutron separation energy S_{2n}, reveal and validate theory predictions of a sudden onset of large deformation from slightly deformed oblate or prolate shapes to strongly prolate shapes in the $58 \leq N \leq 61$ region for Rb and Sr isotopes. A phenomenon that is manifested in Rb and more strongly in Sr with the data presented in this thesis. In contrast, the more neutron-rich $61 \leq N \leq 63$ region reveals no shape transition, and the smooth S_{2n} trend is stabilized again. Adopted mass values of several neighboring neutron-rich isotopes are also influenced [134] by the masses measured here. Hence, this work allows one to validate theoretical models and to refine calculations towards more neutron-rich isotopes, e.g. in Rb and Sr. In the region of interest, several mass models try to accommodate the extreme conditions present. The new mass values will enable e.g. the self-consistent mean-field approximation based on the D1S- or D1M-Gogny

energy density functional ([15] and references therein) to be tested and refined under these extreme conditions.

Differences to previous work of up to 11σ deviation in mass and 6σ deviation in neutron separation energies motivated a study on how these changes influence predictions of the r-process. The r-process model calculations performed indicate that the measured masses are now known to a precision where their uncertainty does not contribute to model uncertainties anymore. This is an essential step forward in removing the nuclear physics uncertainties to better characterizing the problem of r-process models. Nevertheless, the demand for more experimental studies towards more neutron-rich isotopes is pressing. Thus, a further extension of mass measurements in this region is planned. A research proposal (S1373: "Precise mass measurements of Sr and Rb isotopes in the vicinity of the r-process path" [183]) has been submitted to and accepted by the Experiments Evaluation Committee (EEC) at TRIUMF. We request experimental time to perform mass measurements of $^{98}\mathrm{Rb}^{m}$, $^{99-102}\mathrm{Rb}$, and $^{100-102}\mathrm{Sr}$, and the research proposal has been awarded with the highest priority and 16 shifts of 12 hours each.

In general, the increase in precision scales linearly with the charge state (ignoring statistical losses) (see Equation (3.40)). Albeit TITAN's EBIT for charge breeding has become an invaluable tool, the full precision gain has been unattainable, principally due to the large energy spread of the ion bunch ejected from the EBIT. An enhancement of the system efficiency and a reduction of the energy spread would maximize the overall benefit of the charge-breeding program. These effects will be achieved with the implementation of the Cooler Penning Trap (CPET).

Therefore, another major part of this thesis is the design and construction of a preparation trap to strengthen the mass measurement program of HCI with TITAN. The goal of CPET [167, 168, 184] is to increase the precision of mass measurements with HCI and to compensate for negative effects due to the charge-breeding process (efficiency losses, energy spread, etc.). Two cooling techniques using either electrons or protons as a coolant will be investigated to decrease the phase space of the HCI beam.

The design of the multi-ring cylindrical Penning trap of 29 electrodes is based on extensive simulations. The flexibility of the trap structure with its large number of electrodes and the two regions of many-fold segmented electrodes provides for shaping of nested potentials, with regions of high harmonic quality, and regions for the application of various excitation schemes.

Cooling of HCI in a Penning trap requires not only an ultra-high vacuum but also a high magnetic field. The requirements, and the measurement and implementation of both were discussed. Electron and proton sources have been chosen and tested to fit the requirements. To accomplish injec-

tion, trapping, cooling, and extraction of all participating charged particles (i.e. electrons, protons, and HCI), a complicated voltage switching scheme and customized electronics are required. The trap potentials for different manipulation procedures of charged particles have been presented, and the electronics such as high-voltage switches, programmable pulse generators, and arbitrary waveform generators have been introduced.

A design of a full CPET off-line setup with electron- and ion-injection beamlines has been finalized and is currently being implemented. All the ion optics and numerous diagnostics were designed. A vacuum setup has been established; high-voltage switches and pulse programmable generators have been custom-designed and tested. The off-line setup is located on the TITAN platform adjacent to the TITAN beamline, where the support structure of the off-line setup has been placed. The first stage of the commissioning process is documented where electron injection into the trap region, trapping, and extraction have been tested.

The new design of the TITAN beamline is outlined, where the CPET setup is included. The transition from off-line to on-line operation is described and it is planned for 2013, after a full successful off-line commissioning. Once CPET is on-line, the investigations of cooling a HCI beam from the EBIT can commence and an expected on-line commissioning is planned for summer 2013. The implementation of the cooling scheme described in this thesis and its integration into a full TITAN duty cycle, which includes the RFQ, EBIT, CPET, and MPET, will take place at that point. A detailed characterization of both cooling techniques will help to establish the preferred one for the mass measurement of highly charged, short-lived radionuclides.

The boost in precision of high-precision mass measurements, ideally linear in the charge state q, will be fully harnessed if the energy spread of HCI is reduced to ≈ 1 eV/q for the mass measurement. Consequently, CPET is the tool of choice and designed, constructed, and the first commissioning tests have been performed in the scope of this thesis. The new trap is envisaged to have a significant impact for mass measurements at TITAN.

Appendix A

Resonances of Rb and Sr

The main observable in Penning-trap mass spectrometry is the cyclotron frequency $\nu_c = qB/(2\pi \cdot m)$. From a fit of the theoretical line shape [84] to the resonance data (see Figure A.1), the mass can be extracted from the equation above if q and B are known. From the cyclotron frequency the mass can be determined as discussed in Chapters 3 and 5.

Figures A.1 (a) - (d) display cyclotron resonances taken for each rubidium isotope measured: (a) $^{94}Rb^{15+}$, (b) $^{97}Rb^{15+}$, and (c, d) $^{98}Rb^{15+}$ with different frequency scan ranges; Figures A.1 (e) - (h) for each strontium isotope measured: (e) $^{94}Sr^{15+}$, (f) $^{97}Sr^{15+}$, (g) $^{98}Sr^{15+}$, and (h) $^{99}Sr^{15+}$. Each data set shows a cyclotron resonance of the ion of interest for the charge state $q = 15+$. The isotopes were charge bred in the EBIT for 80 ms, and a dipole and quadrupole excitation scheme was applied for 20 ms and 77 ms, respectively. The solid line is a fit of the theoretical line shape [84] to the data, from which the mass of the ion is inferred. As a reference ion $^{85}Rb^{13+}$ was used. A detailed description on the measurement procedure, a discussion on the determined mass value, and their impact on nuclear structure and nuclear astrophysics are presented in Chapter 5.

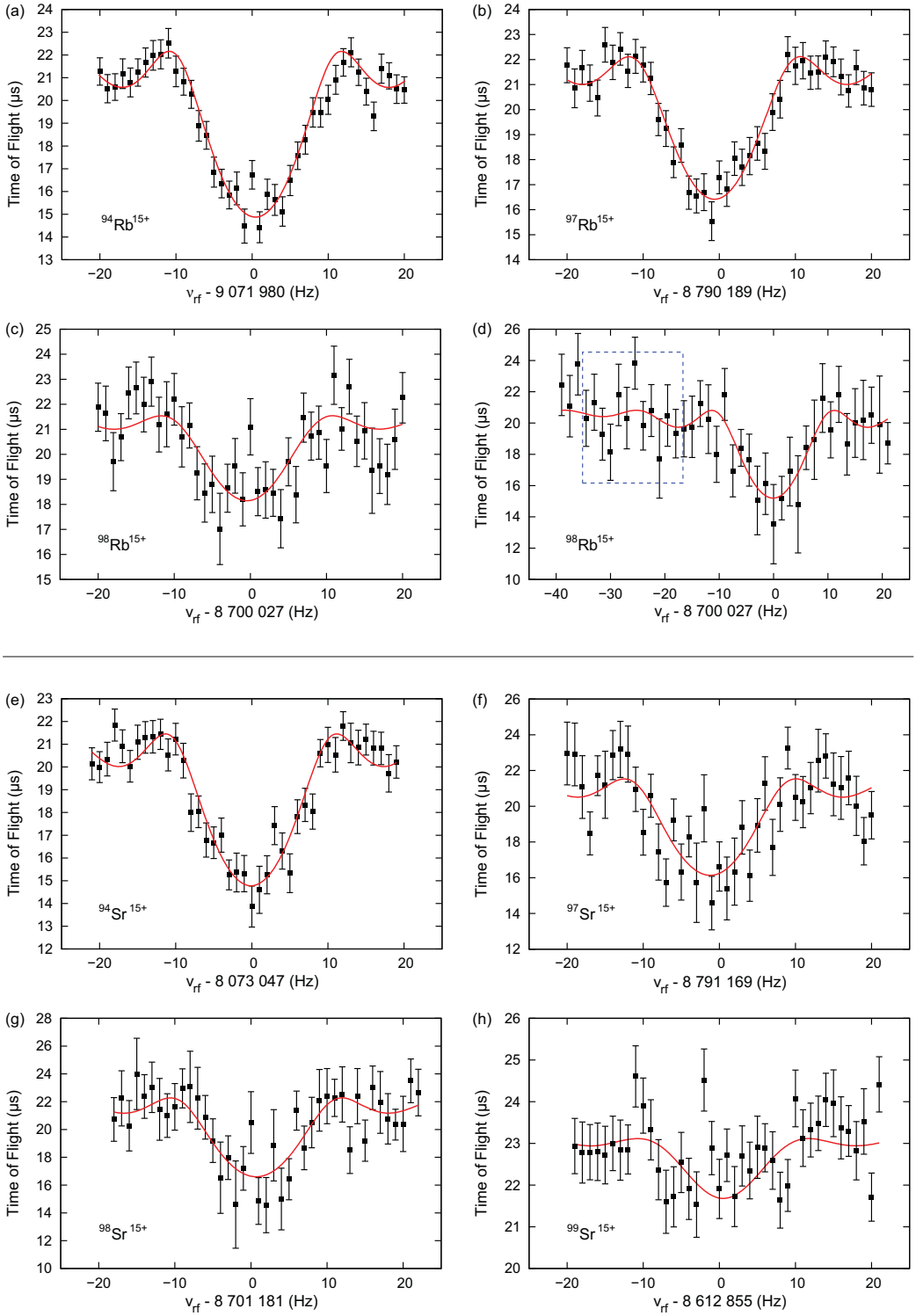

Figure A.1: Cyclotron resonances for Rb and Sr isotopes. For details see text.

Appendix B

TITAN beamline modifications

The TITAN system presently consists of three ion traps, the RFQ, the EBIT, and the MPET (see Chapter 4), all of which are connected by beamlines. The TITAN beamline between EBIT and MPET will be changed completely due to the implementation of CPET (see Chapter 6). The optimal location for the CPET is between EBIT and MPET as shown in Figure 6.1. Here, CPET can serve its purpose to cool the highly charged ions extracted from the EBIT prior to the mass measurement in the MPET. The off-line setup of CPET (see Chapter 7) was designed in this thesis to investigate the two different cooling techniques, the implementation of the cooling switching cycles, and for the commissioning processes of CPET. In addition, the design allows for an easy transition from its off-line location to its on-line location into the TITAN beamline. This process was described in detail in Section 7.3.

Figure B.1 shows a technical drawing of the TITAN beamline (from right to left) between the RFQ, the switchyard, and the MPET. When moving CPET into the TITAN beamline, the existing beamline (see Figure B.1 (top)) will substantially be modified. The platform has been extended, and the new TITAN beamline (see Figure B.1 (bottom)) will include the CPET beamline section as described in Chapter 7 with the so-called CPET off-line system. All diagnostics and optical elements as well as vacuum vessels will be removed and exchanged by the CPET system.

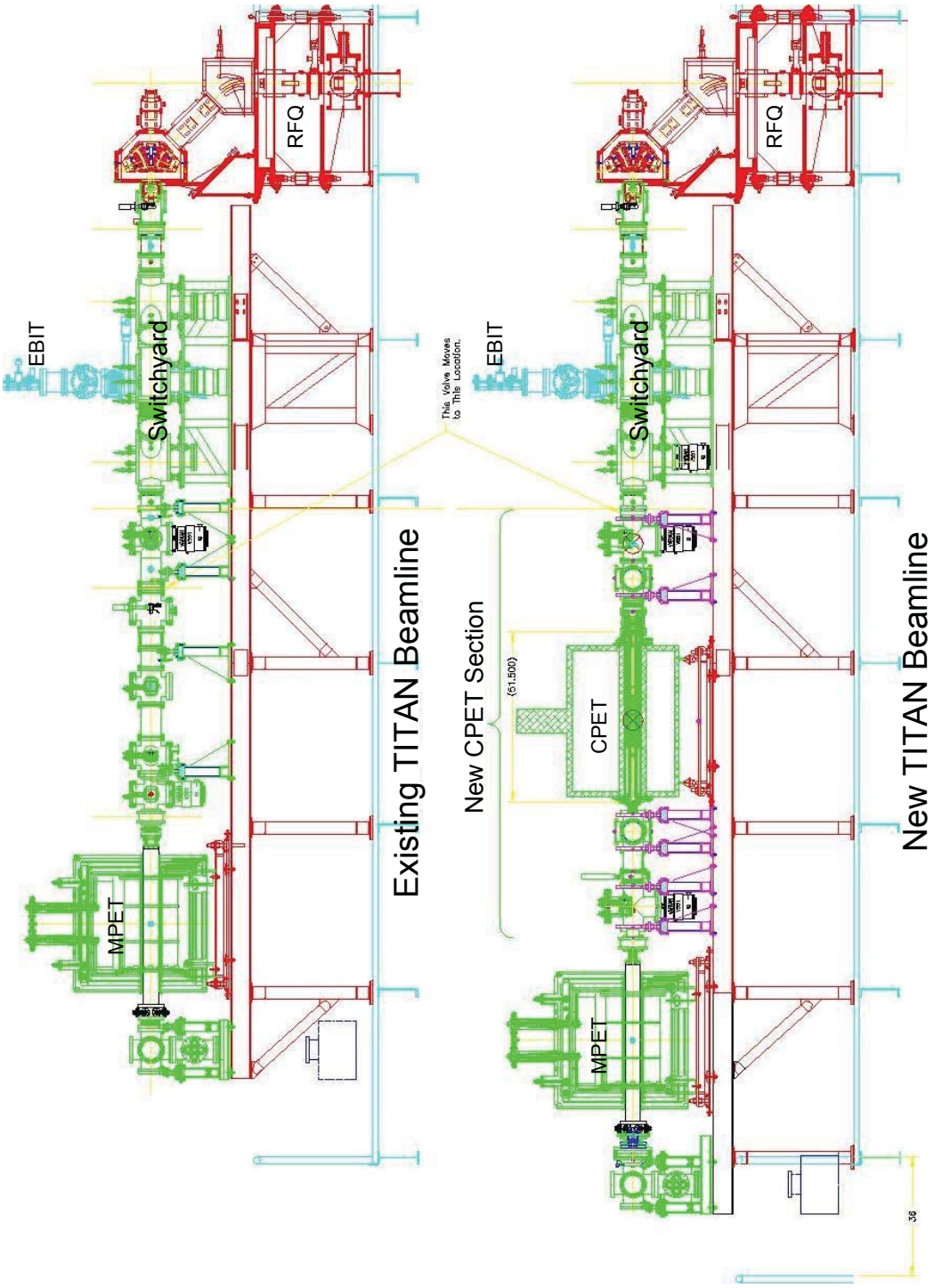

Figure B.1: The existing TITAN beamline (top) and the future TITAN beamline (bottom) including the CPET setup.

Appendix C

Select CPET Drawings

The Cooler Penning Trap (CPET) was designed in the scope of this thesis. Based on ion simulations performed during the design process of the CPET trap structure (see Chapter 6) and the CPET off-line setup (see Chapter 7) many drawings and sub-drawings have been created using Solid Works. Since a display of all of them would expand this thesis dramatically, only a few of the most important drawings will be shown. All of this work in reference to the mechanical drawings, the electronics, and logic is documented on TRIUMF's Archive Database [185, 186].

The entire CPET system design is described in Chapters 6 and 7, and it is incorporated in the assembly drawing IEX 1475, which can be seen in Figures 7.1 and 7.5.

The following figures are presenting main features of the design of the CPET setup. Shown in Figure C.1 are the trap structure, the three types of electrodes in Figure C.2, which are used for constructing the trap region, the stacking and assembly of the single-lens electrodes in Figure C.3, and the two regions of segmented electrodes in Figure C.4, the four-split cylindrical steerer in the fringe magnetic field in Figure C.5, the complicated design of feed-through section and its 45 feeds in Figures C.5, C.6, and C.7, two of the diagnostic units placed on a linear motion feed-through, i.e. an MCP unit in Figure C.8, and the double-sided Faraday-cup unit in Figure C.9, and the combined Einzel lens and steerer assembly in Figure C.10. The two different ion sources are displayed in Figures C.11 and C.12 with the ion source and the electron source with each their extraction optics, respectively. The design of the electron source presents the off-axis location of the field-emission array, which has been determined via ion simulations.

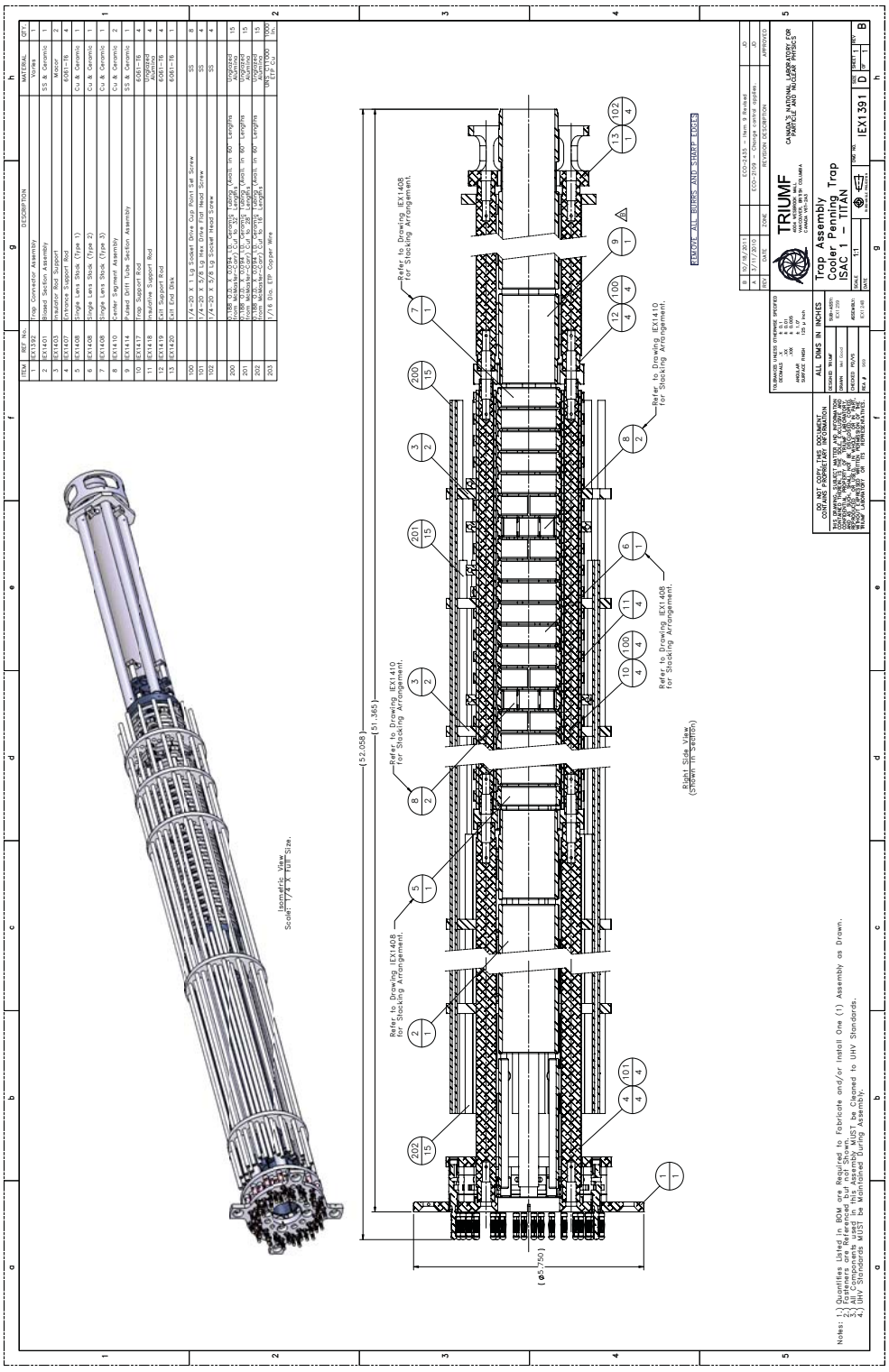

Figure C.1: The design of the CPET trap structure (IEX 1391) is shown.

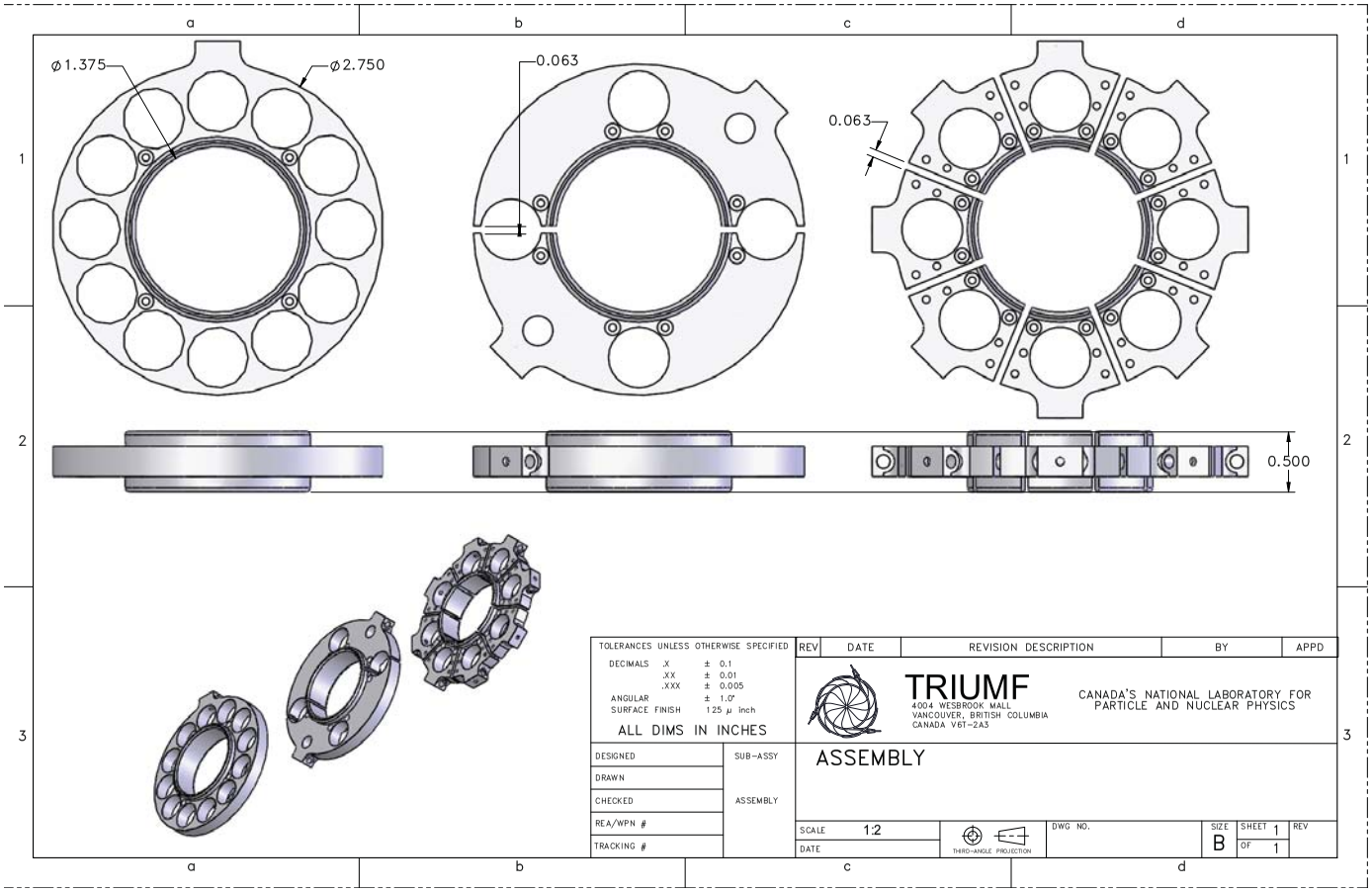

Figure C.2: The CPET trap structure consists of 29 trap electrodes with 23 non-segmented single electrodes, four two-fold segmented, and two eight-fold segmented electrodes. The display is part of the drawing IEX 1410.

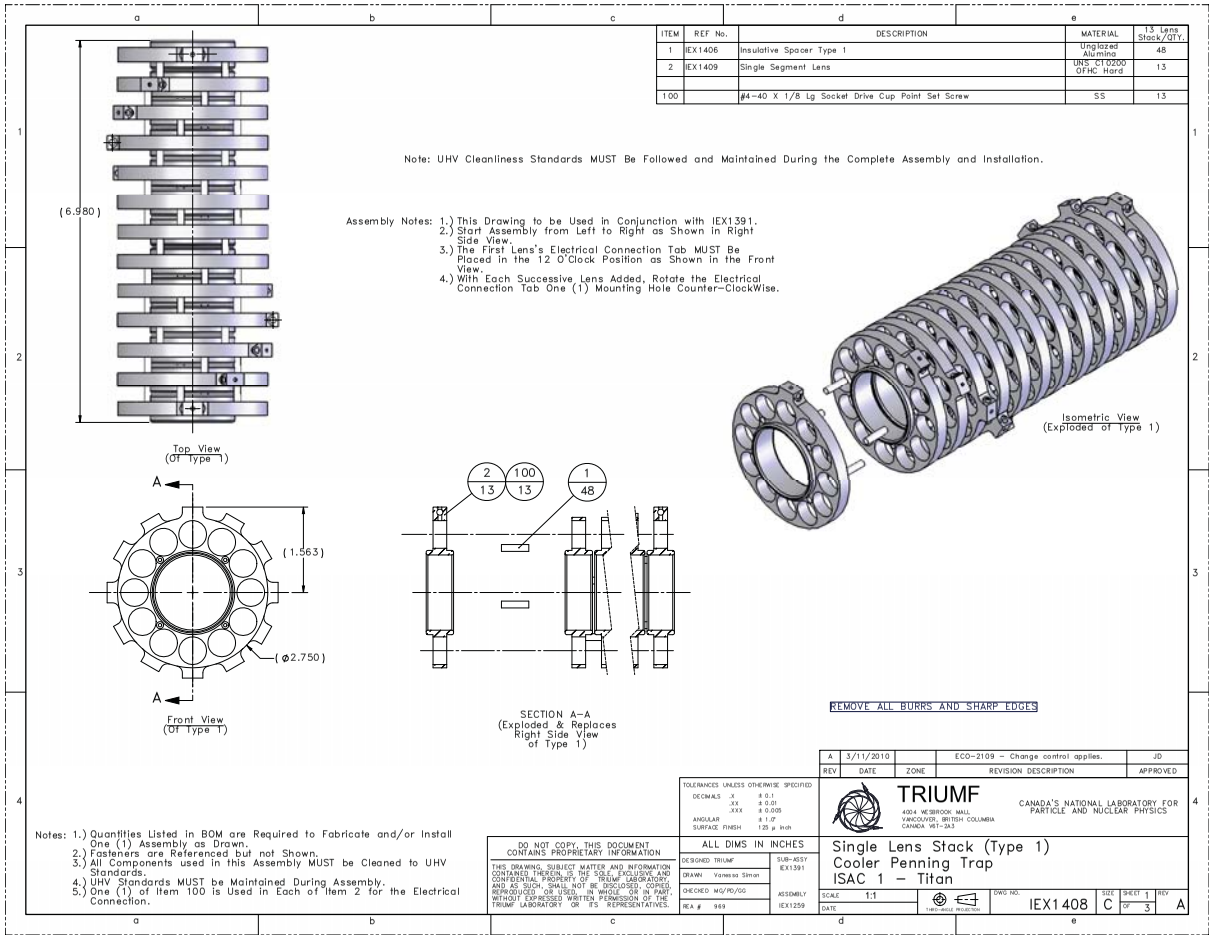

Figure C.3: IEX 1408 displays the stacking of the single electrodes (see Figure C.2 for their individual design) with the ceramic spacers in between.

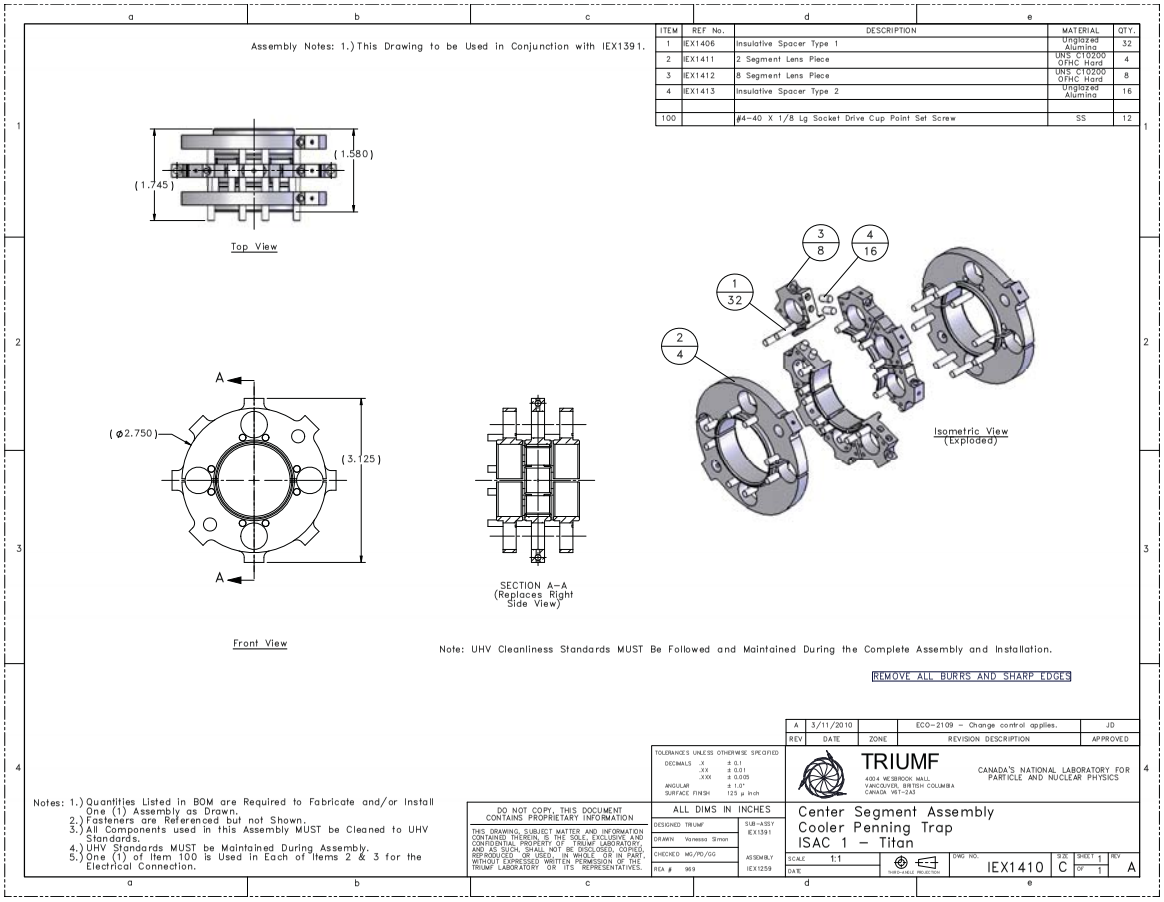

Figure C.4: The trap structure consists of two regions with a series of (2-8-2)-fold segmented electrodes (see Figure C.2 for their individual design). For the stacking as shown in this drawing (IEX 1410) two types of ceramic spacers are used.

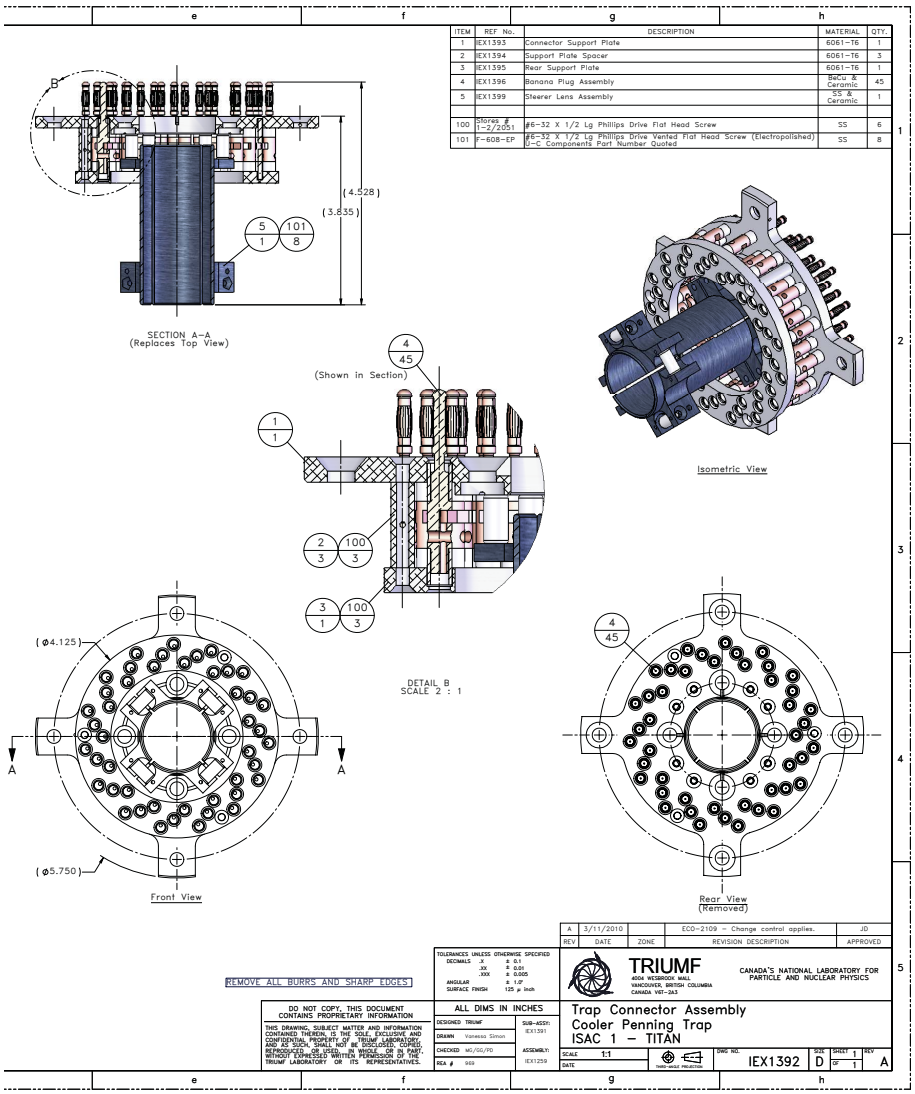

Figure C.5: The trap connector assembly (IEX 1392) consists of the four-split cylindrical steerer and the connection between the feed-through section (see Figures C.6 and C.7). The 45 plugs connect the wires that are going to the electrodes to the feed-through section where they are fed to power supplies.

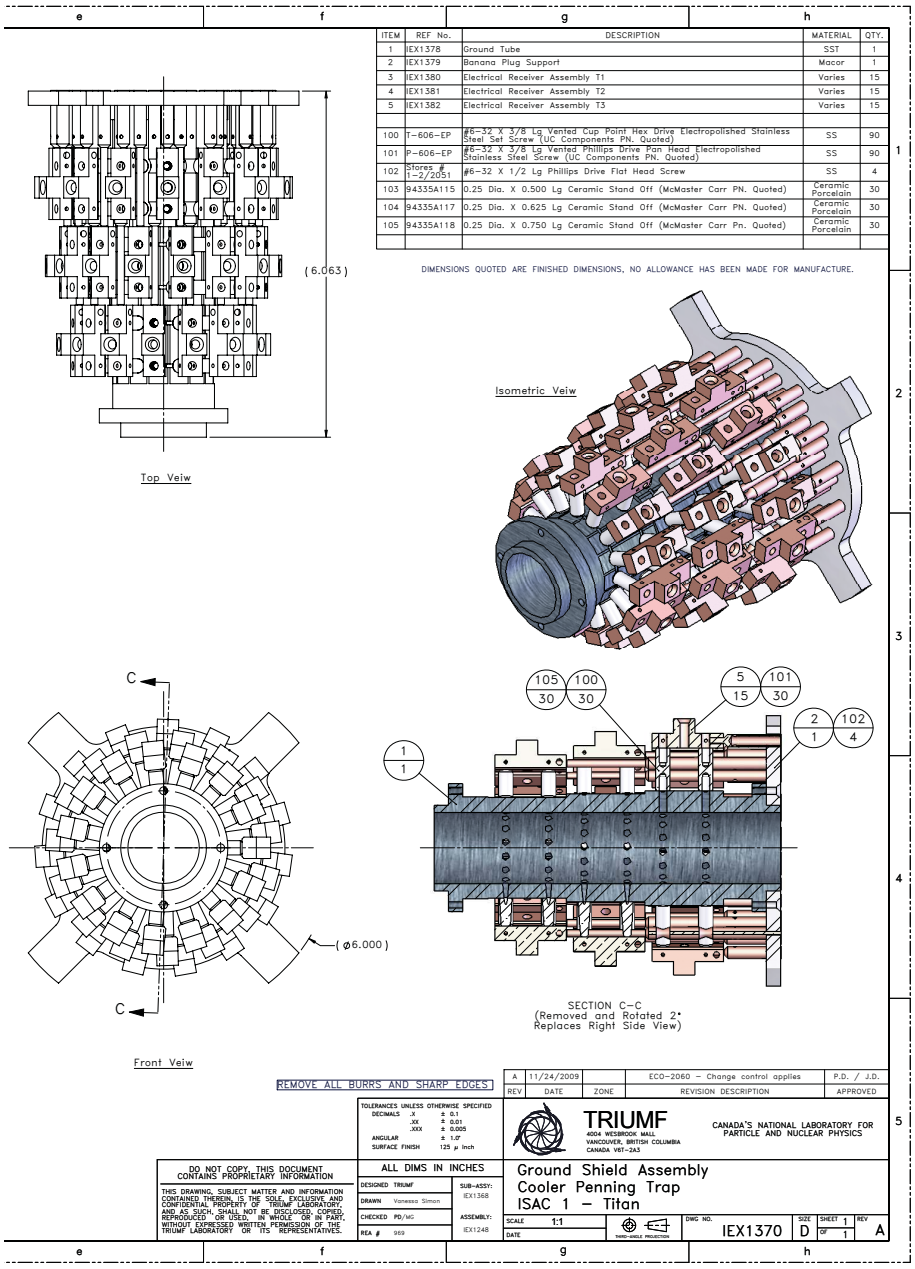

Figure C.6: The design of the inside of the feed-through section (IEX 1370) shows the inner drift tube and the counterpart to Figure C.5, where all the plugs are plugged into.

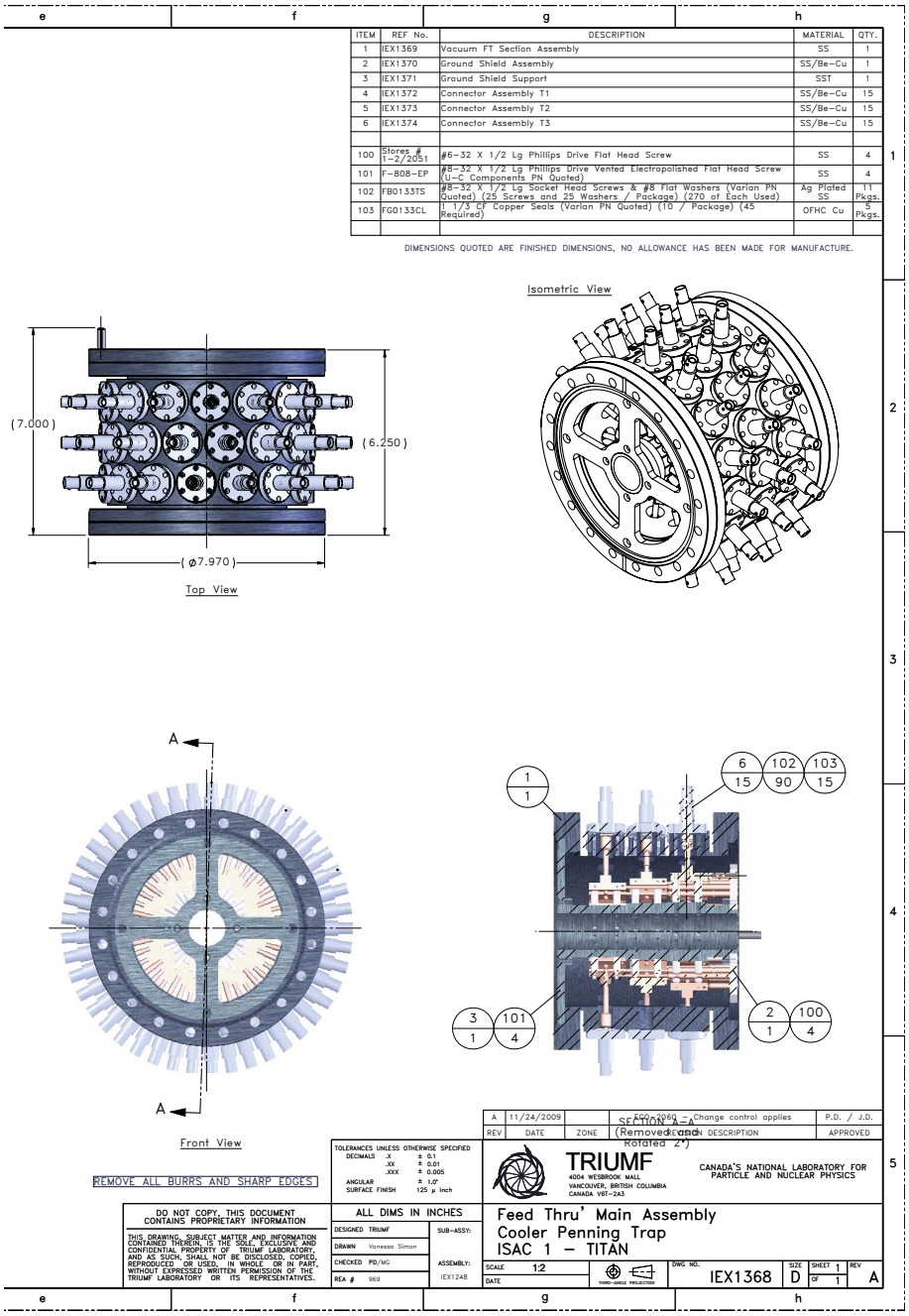

Figure C.7: The main assembly of the feed-through section (IEX 1368) consists of IEX 1392 (see Figure C.6). The voltages from up to 45 power supplies are fed into the vacuum vessel and the trap structure through this design.

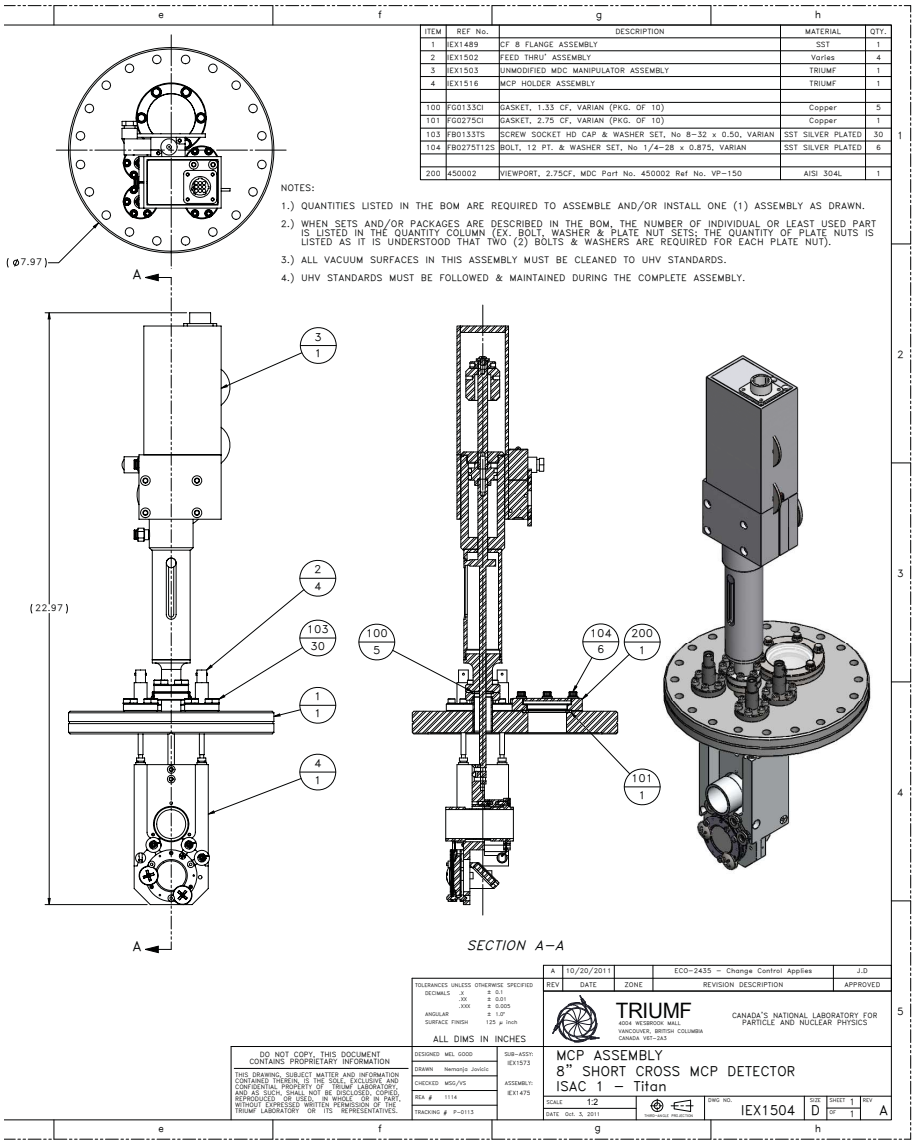

Figure C.8: The drawing IEX 1504 presents the design for the unit consisting of an MCP and a drift tube. The unit is mounted on a linear motion feedthrough using a form of antennas to not use any flexible wires that could cause a short. The design also incorporates a mirror to feed the image at the phosphor screen of the MCP to a CCD camera mounted outside of the vessel at the glass window of the opponent unit (which is either another MCP unit or a FC unit (see Figure C.9).

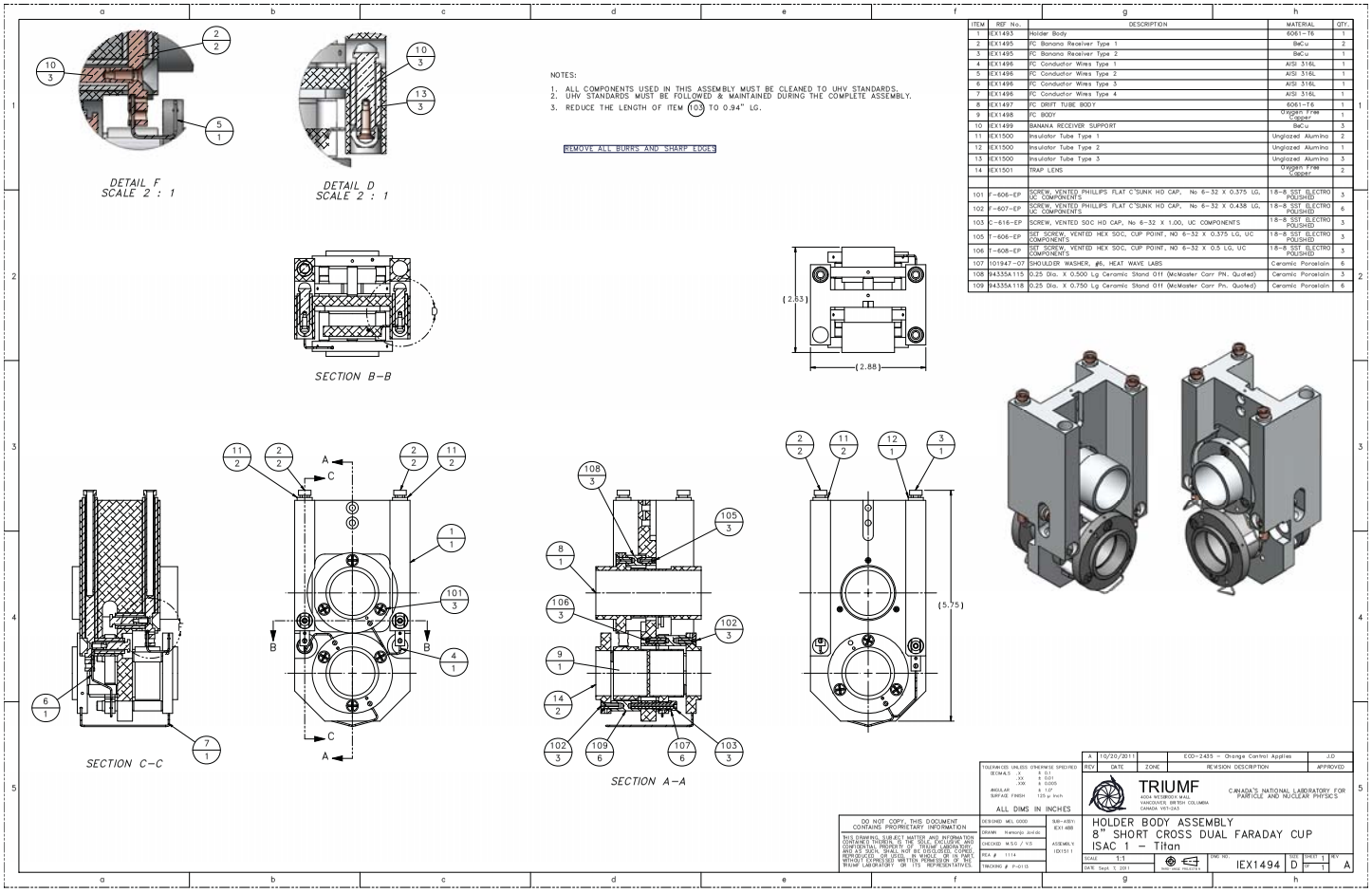

Figure C.9: Similar to the MCP unit, the Faraday-cup unit (IEX 1494) is mounted on a linear motion feed-through. It consists of a drift tube and a double-sided Faraday cup each with a repel-lens.

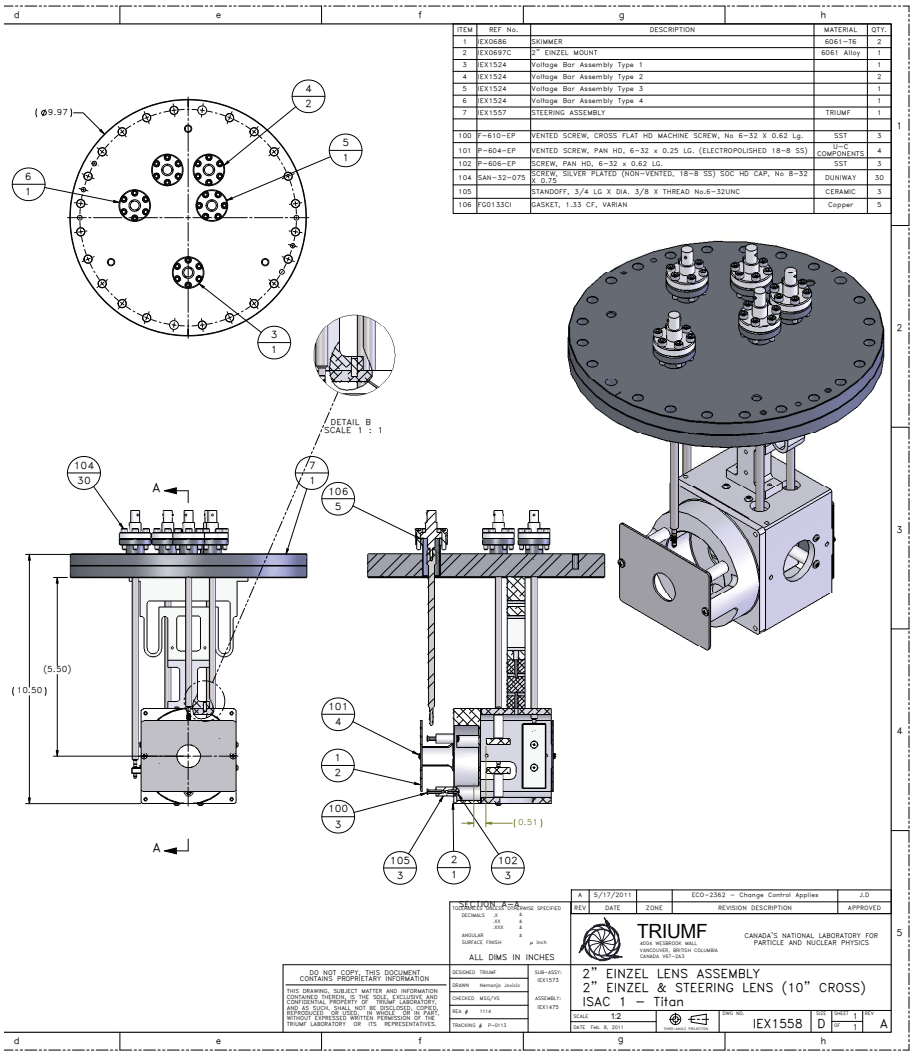

Figure C.10: In the cross next to the ion source, an Einzel-lens and steerer assembly (IEX 1558) is housed. It consists of a x- and y- steerer which builds up two parts of the three-part Einzel lens. In addition, two apertures are mounted on each side.

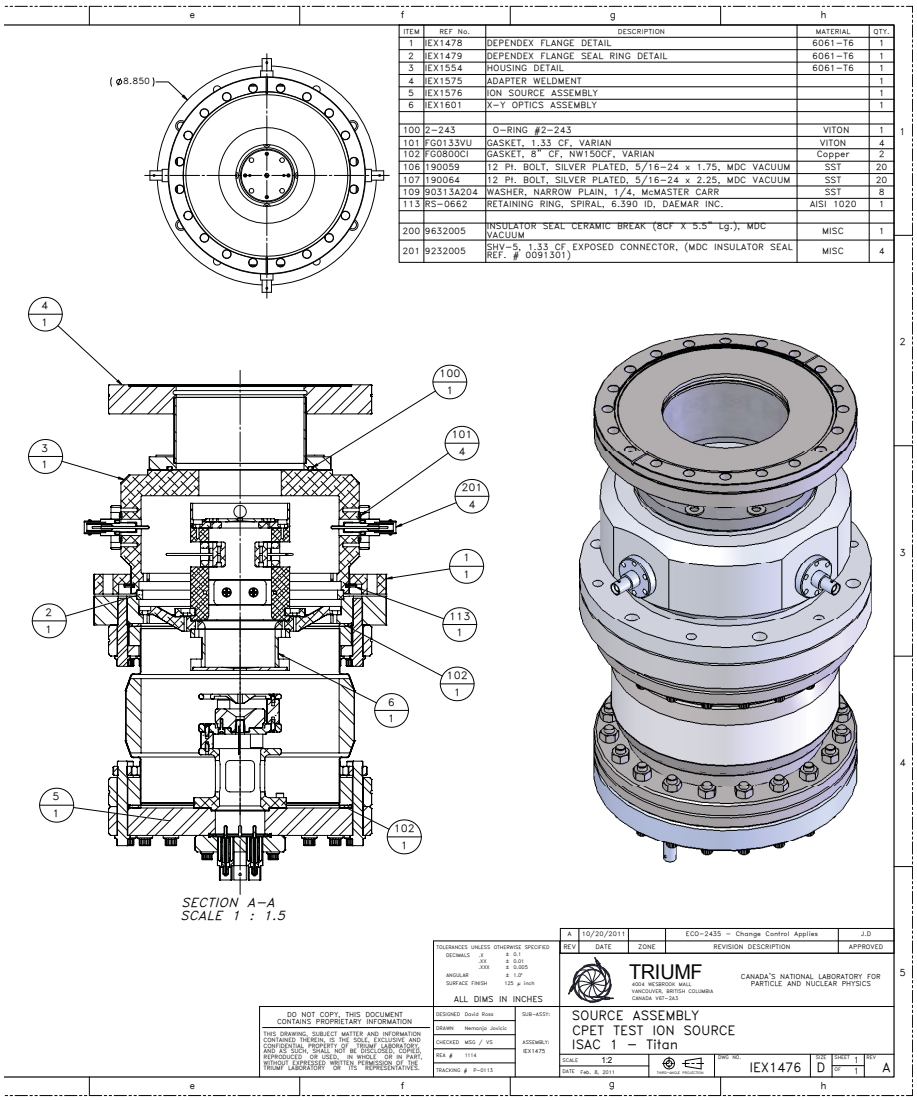

Figure C.11: The ion source assembly (IEX 1476) contains the ion source mount and a full set of extraction optics.

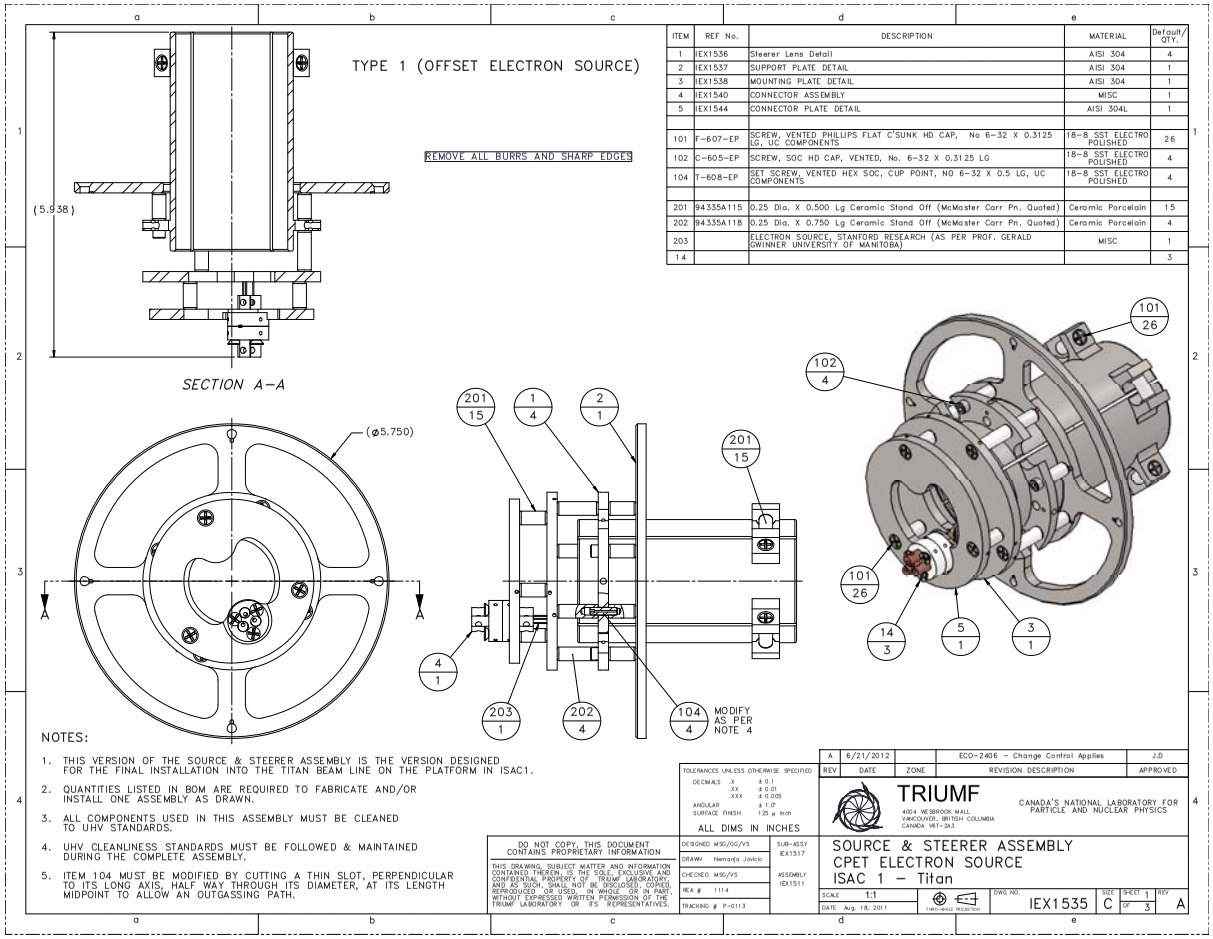

ITEM	REF No.	DESCRIPTION	MATERIAL	Default/ QTY.
1	IEX1536	Steerer Lens Detail	AISI 304	4
2	IEX1537	SUPPORT PLATE DETAIL	AISI 304	1
3	IEX1538	MOUNTING PLATE DETAIL	AISI 304	1
4	IEX1540	CONNECTOR ASSEMBLY	MISC	1
5	IEX1544	CONNECTOR PLATE DETAIL	AISI 304L	1
101	F-607-EP	SCREW, VENTED PHILLIPS FLAT C'SUNK HD CAP, No 6-32 X 0.3125 LG, UC COMPONENTS	18-8 SST ELECTRO POLISHED	26
102	C-605-EP	SCREW, SOC HD CAP, VENTED, No. 6-32 X 0.3125 LG	18-8 SST ELECTRO POLISHED	4
104	T-608-EP	SET SCREW, VENTED HEX SOC, CUP POINT, NO 6-32 X 0.5 LG, UC COMPONENTS	18-8 SST ELECTRO POLISHED	4
201	94335A115	0.25 Dia. X 0.500 Lg Ceramic Stand Off (McMaster Carr Pn. Quoted)	Ceramic Porcelain	15
202	94335A118	0.25 Dia. X 0.750 Lg Ceramic Stand Off (McMaster Carr Pn. Quoted)	Ceramic Porcelain	4
203		ELECTRON SOURCE, STANFORD RESEARCH (AS PER PROF. GERALD GWINNER UNIVERSITY OF MANITOBA)	MISC	1
14				3

REV	DATE	ZONE	REVISION DESCRIPTION	APPROVED
A	6/21/2012		ECO-2406 – Change Control Applies	J.D

TOLERANCES UNLESS OTHERWISE SPECIFIED
DECIMALS .X ± 0.1, .XX ± 0.01, .XXX ± 0.005
ANGULAR ± 1.0°
SURFACE FINISH 125 µ inch
ALL DIMS IN INCHES

DO NOT COPY, THIS DOCUMENT CONTAINS PROPRIETARY INFORMATION

DESIGNED M'SG/GG/VS | DRAWN Nemanja Jokicic | CHECKED M'SG/VS | REA # 1114 | TRACKING # P-0113

SUB-ASSY IEX1517 | ASSEMBLY IEX1511

SCALE 1:1 | DATE Aug. 18, 2011 | DWG NO. IEX1535 | SIZE C | SHEET 1 OF 3 | REV A

Figure C.12: The electron source assembly (IEX 1535) contains the electron source featuring the field-emission array at the off-axis position, an extraction optics and the four-split cylindrical steerer.

Bibliography

[1] Klaus Blaum. High-accuracy mass spectrometry with stored ions. *Physics Reports*, 425(1):1–78, March 2006.

[2] D. Lunney, J.M. Pearson, and C. Thibault. Recent trends in the determination of nuclear masses. *Reviews of Modern Physics*, 75:1021–1082, July 2003.

[3] J. Erler, N. Birge, M. Kortelainen, W. Nazarewicz, E. Olsen, A.M. Perhac, and M. Stoitsov. The limits of the nuclear landscape. *Nature (London)*, 486(7404):509–512, June 2012.

[4] H. Savajols, B. Jurado, W. Mittig, D. Baiborodin, W. Catford, M. Chartier, C.E. Demonchy, Z. Dlouhy, A. Gillibert, L. Giot, A. Khouaja, A. Lépine-Szily, S. Lukyanov, J. Mrazek, N. Orr, Y. Penionzhkevich, S. Pita, M. Rousseau, P. Roussel-Chomaz, and A.C.C. Villari. New mass measurements at the neutron drip-line. *The European Physical Journal A*, 25(S01):23–26, August 2005.

[5] U. Hager, T. Eronen, J. Hakala, A. Jokinen, V.S. Kolhinen, S. Kopecky, I. Moore, A. Nieminen, M. Oinonen, S. Rinta-Antila, J. Szerypo, and J. Äystö. First Precision Mass Measurements of Refractory Fission Fragments. *Physical Review Letters*, 96(4):042504, February 2006.

[6] S. Rahaman, U. Hager, V.-V. Elomaa, T. Eronen, J. Hakala, A. Jokinen, A. Kankainen, P. Karvonen, I.D. Moore, H. Penttilä, S. Rinta-Antila, J. Rissanen, A. Saastamoinen, T. Sonoda, and J. Äystö. Precise atomic masses of neutron-rich Br and Rb nuclei close to the r-process path. *The European Physical Journal A*, 32(1):87–96, April 2007.

[7] U. Hager, A. Jokinen, V.-V. Elomaa, T. Eronen, J. Hakala, A. Kankainen, S. Rahaman, J. Rissanen, I. D. Moore, S. Rinta-Antila, A. Saastamoinen, T. Sonoda, and J. Äystö. Precision mass measurements of neutron-rich yttrium and niobium isotopes. *Nuclear Physics A*, 793:20–39, September 2007.

[8] J. Hakala, R. Rodríguez-Guzmán, V.-V. Elomaa, T. Eronen, A. Jokinen, V.S. Kolhinen, I.D. Moore, H. Penttilä, M. Reponen, J. Rissanen, A. Saastamoinen, and J. Äystö. Precision mass measurements of neutron-rich Y, Nb, Mo, Tc, Ru, Rh, and Pd isotopes. *The European Physical Journal A*, 47(10):129, October 2011.

[9] P. Campbell, H.L. Thayer, J. Billowes, P. Dendooven, K.T. Flanagan, D.H. Forest, J.A. R. Griffith, J. Huikari, A. Jokinen, R. Moore, A. Nieminen, G. Tungate, S. Zemlyanoi, and J. Äystö. Laser Spectroscopy of Cooled Zirconium Fission Fragments. *Physical Review Letters*, 89(8):082501, August 2002.

[10] S. Naimi, G. Audi, D. Beck, K. Blaum, Ch. Böhm, Ch. Borgmann, M. Breitenfeldt, S. George, F. Herfurth, A. Herlert, M. Kowalska, S. Kreim, D. Lunney, D. Neidherr, M. Rosenbusch, S. Schwarz, L. Schweikhard, and K. Zuber. Critical-Point Boundary for the Nuclear Quantum Phase Transition Near A=100 from Mass Measurements of ^{96,97}Kr. *Physical Review Letters*, 105(3):032502, July 2010.

[11] M. Albers *et al.* Evidence for a Smooth Onset of Deformation in the Neutron-Rich Kr Isotopes. *Physical Review Letters*, 108(6):062701, February 2012.

[12] M. Epherre, G. Audi, C. Thibault, R. Klapisch, G. Huber, F. Touchard, and H. Wollnik. Direct measurements of the masses of rubidium and cesium isotopes far from stability. *Physical Review C*, 19(4):1504–1522, 1979.

[13] R. Rodríguez-Guzmán, P. Sarriguren, and L.M. Robledo. Signatures of shape transitions in odd-A neutron-rich rubidium isotopes. *Physical Review C*, 82(6):061302(R), December 2010.

[14] A. Kumar and M.R. Gunye. Nuclear structure of Sr, Zr, and Mo isotopes. *Physical Review C*, 32(6):2116–2121, 1985.

[15] R. Rodríguez-Guzmán, P. Sarriguren, and L.M. Robledo. Shape evolution in yttrium and niobium neutron-rich isotopes. *Physical Review C*, 83(4):044307, April 2011.

[16] J. Billowes, T.A. Broome, A.M. Bruce, W.N. Catford, J.L. Durell, S.J. Freeman, M. Freer, W. Gelletly, R.D. Page, H.G. Price, P. J. Woods, and D.D. Warner. SIRIUS Science Report. *Council for the Central Laboratory of the Research Council*, 1998.

[17] M. Arnould, S. Goriely, and K. Takahashi. The r-process of stellar nucleosynthesis: Astrophysics and nuclear physics achievements and mysteries. *Physics Reports*, 450:97–213, 2007.

[18] A. Arcones and G. Martínez-Pinedo. Nucleosynthesis in neutrino-driven winds: Influence of the nuclear physics input. *Journal of Physics: Conference Series*, 202:012007, January 2010.

[19] A. Arcones and G. Bertsch. Nuclear Correlations and the r Process. *Physical Review Letters*, 108(15):1–5, April 2012.

[20] J. Dilling, P. Bricault, M. Smith, H.-J. Kluge, and TITAN Collaboration. The proposed TITAN facility at ISAC for very precise mass measurements on highly charged short-lived isotopes. *Nuclear Instruments and Methods in Physics Research Section B: Beam Interactions with Materials and Atoms*, 204:492–496, May 2003.

[21] W. Heisenberg. Über den Bau der Atomkerne. II. *Zeitschrift für Physik A Hadrons and Nuclei*, 78(3-4):156–164, 1932.

[22] E. Komatsu, J. Dunkley, M.R. Nolta, C.L. Bennett, B. Gold, G. Hinshaw, N. Jarosik, D. Larson, M. Limon, L. Page, D.N. Spergel, M. Halpern, R. S. Hill, A. Kogut, S.S. Meyer, G.S. Tucker, J.L. Weiland, E. Wollack, and E.L. Wright. Five-Year Wilkinson Microwave Anisotropy Probe Observations: Cosmological Interpretation. *The Astrophysical Journal Supplement Series*, 180(2):330–376, February 2009.

[23] P.J. Woods and C.N. Davids. Nuclei Beyond the Proton Drip-Line. *Annual Review of Nuclear and Particle Science*, 47:541–590, 1997.

[24] C.F. von Weizsäcker. Zur Theorie der Kernmassen. *Zeitschrift für Physik A Hadrons and Nuclei*, 96(7-8):431–458, 1935.

[25] H.A. Bethe and R.F. Bacher. Stationary states of nuclei. *Reviews of Modern Physics*, 8(2):82, 1936.

[26] W.D. Myers and W.J. Swiatecki. Nuclear masses and deformation. *Nuclear Physics*, 81(1):1–60, 1966.

[27] M. Bender, G.F. Bertsch, and P.-H. Heenen. Collectivity-induced quenching of signatures for shell closures. *Physical Review C*, 78(5):054312, November 2008.

[28] G. Audi, A.H. Wapstra, and C. Thibault. The AME2003 atomic mass evaluation (II). Tables, graphs and references. *Nuclear Physics A*, 729:337–676, 2003.

[29] M. Goeppert Mayer and J.H.D. Jensen. *Elementary Theory of Nuclear Shell Structure*. John Wiley & Sons, Inc., New York, 1955.

[30] G. Royer. On The Mass Formula And Wigner And Curvature Energy Terms. *Romanian Reports in Physics*, 59(2):625–634, 2007.

[31] P. Möller, W.D. Myers, H. Sagawa, and S. Yoshida. New Finite-Range Droplet Mass Model and Equation-of-State Parameters. *Physical Review Letters*, 108(5):052501, January 2012.

[32] J. Decharge and D. Gogny. Hartree-Fock-Bogolyubov calculations with the D1 effective interaction on spherical nuclei. *Physical Review C*, 21(4):1568–1593, 1980.

[33] J. Dobaczewski, H. Flocard, and J. Treiner. Hartree-Fock-Bogolyubov description of nuclei near the neutron-drip. *Nuclear Physics A*, 422(1):103–139, 1984.

[34] M. Warda, A. Staszczak, and L.P.R. Ochniak. Comparison of Self-Consistent Skyrme and Gogny Calculations for Light Hg Isotopes. *International Journal of Modern Physics E*, 19(4):787–793, 2011.

[35] S. Goriely, S. Hilaire, M. Girod, and S. Péru. First Gogny-Hartree-Fock-Bogoliubov Nuclear Mass Model. *Physical Review Letters*, 102(24):2–5, June 2009.

[36] R. Rodríguez-Guzmán, P. Sarriguren, L.M. Robledo, and S. Perez-Martin. Charge radii and structural evolution in Sr, Zr, and Mo isotopes. *Physics Letters B*, 691(4):202–207, August 2010.

[37] J. Duflo and A.P. Zuker. Microscopic mass formulas. *Physical Review C: Nuclear Physics*, 52(1):R23–R27, July 1995.

[38] T. Otsuka, A. Arima, F. Iachello, and I. Talmi. Shell Model Description of Interacting Bosons. *Physics Letters B*, 76(2):139–143, 1978.

[39] B. Alex Brown. The Nuclear Shell Model Towards the Drip Lines. *Progress in Particle and Nuclear Physics*, 47(2001):517–604, 2002.

[40] A.N. Andreyev *et al.* A Triplet of Differently Shaped Spin-Zero States in the Atomic Nucleus ^{186}Pb. *Nature (London)*, 405(6785):430–433, May 2000.

[41] R.F. Casten. Quantum phase transitions and structural evolution in nuclei. *Progress in Particle and Nuclear Physics*, 62(1):183–209, 2009.

[42] G. Lhersonneau, B Pfeiffer, K.-L. Kratz, T. Enqvist, P.P. Jauhp, A. Jokinen, J. Kantele, M. Leino, J.M. Parmonen, H. Penttilä, and J. Äystö. Evolution of deformation in the neutron-rich Zr region from excited intruder state to the ground state. *Physical Review C*, 49(3):1379 – 1390, 1994.

[43] E.M. Burbidge, G.R. Burbidge, W.A. Fowler, and F. Hoyle. Synthesis of the Elements in Stars. *Reviews of Modern Physics*, 29:547–650, 1957.

[44] M. Arnould and S. Goriely. The p-process of stellar nucleosynthesis: astrophysics and nuclear physics status. *Physics Reports*, 384(1-2):1–84, September 2003.

[45] E. Anders. Abundances of the elements: Meteoritic and solar. *Geochimica et Cosmochimica Acta*, 53:197–214, 1989.

[46] M. Busso, R. Gallino, and G.J. Wasserburg. Nucleosynthesis in asymptotic giant branch stars: Relevance for galactic enrichment and solar system formation. *Annual Review of Astronomy and Astrophysics*, 37:239–309, 1999.

[47] P.A. Seeger, W.A. Fowler, and D.D. Clayton. Nucleosynthesis of Heavy Elements by Neutron Capture. *The Astrophysical Journal Supplement Series*, 11(3):121, February 1965.

[48] V. Bouquelle, N. Cerf, M. Arnould, T. Tachibana, and S. Goriely. Single and multi-event canonical r-process: astrophysics and nuclear physics considerations. *Astronomy and Astrophysics*, 305:1005–1018, 1996.

[49] Karlheinz Langanke. Nuclear input for supernova simulations and nucleosyntheis. *Nuclear Physics A*, 834(1-4):608c–614c, March 2010.

[50] G.S. Bisnovatyi-Kogan and V.M. Chechetkin. Accretion onto a rapidly moving gravitating center. *Soviet Astronomy*, 23:201–205, 1979.

[51] J.M. Lattimer and D.N. Schramm. The tidal disruption of neutron stars by black holes in close binaries. *The Astrophysical Journal*, 210:549–567, 1976.

[52] V.S. Imshennik. Explosion mechanism in supernovae collapse. *Space Science Reviews*, 74(3-4):325–334, November 1995.

[53] V.S. Imshennik and I.Yu. Litvinova. Neutrino crown of a protoneutron star and analysis of its convective instability. *Physics of Atomic Nuclei*, 69(4):636–657, April 2006.

[54] B.S. Meyer, G.J. Mathews, W.M. Howard, S.E. Woosley, and R.D. Hoffman. R-process nucleosynthesis in the high-entropy supernova bubble. *The Astrophysical Journal*, 399:656–664, 1992.

[55] E.M.D. Symbalisty and D.N. Schramm. Neutron star collisions and the r-process. *Astrophysical Letters*, 22(4):143–145, 1982.

[56] V.V. Simon, T. Brunner, U. Chowdhury, B. Eberhardt, S. Ettenauer, A.T. Gallant, E. Mané, M.C. Simon, P. Delheij, M.R. Pearson, G. Audi, G. Gwinner, D. Lunney, H. Schatz, and J. Dilling. Penning-trap mass spectrometry of highly charged, neutron-rich Rb and Sr isotopes in the vicinity of A≈100. *Physical Review C*, 85(6):064308, June 2012.

[57] Hendrik Schatz. Private communication. 2012.

[58] S. Wanajo and Y. Ishimaru. R-process calculations and Galactic chemical evolution. *Nuclear Physics A*, 777:676–699, October 2006.

[59] K. Otsuki, H. Tagoshi, T. Kajino, and S.-Y. Wanajo. General relativictic effects on neutron-driven winds from young, hot neutron stars and r-process nucleosynthesis. *The Astrophysical Journal*, (533):424–439, 2000.

[60] K. Takahashi, J. Witti, and H.-Th. Janka. Nucleosynthesis in neutrino-driven winds from protoneutron stars: The r-process. *Astronomy and Astrophysics*, 286:857–869, 1994.

[61] M. Terasawa, K. Sumiyoshi, T. Kajino, G.J. Mathews, and I. Tanihata. New nuclear reaction flow during r-process nucleosynthesis in supernovae: Critical role of light, neutron-rich nuclei. *The Astrophysical Journal*, 562:470–479, 2001.

[62] S. Wanajo, T. Kajino, G.J. Mathews, and K. Otsuki. The r-process in neutrino-driven winds from nacsent, "compact" neutron stars of core-collapse supernovae. *The Astrophysical Journal*, 554:578–586, 2001.

[63] S.E. Woosley, J.R. Wilson, G.J. Mathews, R.D. Hoffman, and B.S. Meyer. The r-process and neutrino-heated supernova ejecta. *The Astrophysical Journal*, 433:229–246, 1994.

[64] C. Freiburghaus, J.-F. Rembges, T. Rauscher, E. Kolbe, F.-K. Thielemann, K.-L. Kratz, B. Pfeiffer, and J.J. Cowan. The astrophysical r-process: a comparison of calculations following adiabatic expansion with classical calculations based on neutron densities and temperatures. *The Astrophysical Journal*, 516:381–398, 1999.

[65] A. Arcones and G. Martínez-Pinedo. Dynamical r-process studies within the neutrino-driven wind scenario and its sensitivity to the nuclear physics input. *Physical Review C*, 83(4):1–18, April 2011.

[66] P. Moller, J.R. Nix, and W.D. Myers. Nuclear ground-state masses and deformations. *Atomic Data and Nuclear Data*, 59(2):185–381, 1995.

[67] J.M. Pearson, R.C. Nayaka, and S. Goriely. Nuclear mass formula with Bogolyubov-enhanced shell-quenching: application to r-process. *Physics Letters B*, 387:455–459, 1996.

[68] Y.U.E. Penionzhkevich. Mass Measurements in Nuclear Reactions. *Hyperfine Interactions*, 132(1-4):265–273, 2001.

[69] Georg Bollen. Mass measurements of short-lived nuclides with ion traps. *Nuclear Physics A*, 693(1-2):3–18, October 2001.

[70] Wolfgang Paul. Electromagnetic traps for charged and neutral particles. *Reviews of Modern Physics*, 62(3):531–540, 1990.

[71] Hans Dehmelt. Experiments with an isolated subatomic particle at rest. *Reviews of Modern Physics*, 62(1990):525–531, 1990.

[72] I. Marzoli, P. Tombesi, G. Ciaramicoli, G. Werth, P. Bushev, S. Stahl, F. Schmidt-Kaler, M. Hellwig, C. Henkel, G. Marx, I. Jex, E. Stachowska, G. Szawiola, and A. Walaszyk. Experimental and theoretical challenges for the trapped electron quantum computer. *Journal of Physics B: Atomic, Molecular and Optical Physics*, 42(15):154010, August 2009.

[73] J.K. Thompson, S. Rainville, and D.E. Pritchard. Cyclotron frequency shifts arising from polarization forces. *Nature (London)*, 430:58–61, July 2004.

[74] W. Jones. Earnshaw's theorem and the stability of matter. *European Journal of Physics*, 1:85–88, 1980.

[75] L. Brown and G. Gabrielse. Geonium theory: Physics of a single electron or ion in a Penning trap. *Reviews of Modern Physics*, 58(1):233–311, January 1986.

[76] G. Bollen, R.B. Moore, G. Savard, and H. Stolzenberg. The accuracy of heavy-ion mass measurements using time of flight-ion cyclotron resonance in a Penning trap. *Journal of Applied Physics*, 68(9):4355–4374, 1990.

[77] Georg Bollen. Traps for rare isotopes. *The Euroschool Lectures on Physics with Exotic Beams, Lecture Notes in Physics*, 651:169–210, 2004.

[78] V.N. Gheorghe, F.G. Major, and G. Werth. *Charged Particle Traps – The Physics and Techniques of Charged Particle Field Confinement.* Springer, August 2004.

[79] M. Brodeur, V.L. Ryjkov, T. Brunner, S. Ettenauer, A.T. Gallant, V.V. Simon, M.J. Smith, A. Lapierre, R. Ringle, P. Delheij, M. Good, D. Lunney, and J. Dilling. Verifying the accuracy of the TITAN Penning-trap mass spectrometer. *International Journal of Mass Spectrometry*, 310:20–31, January 2012.

[80] Scientific Instrument Services. SIMION. Version 8.0.

[81] Martin Kretzschmar. The Ramsey method in high-precision mass spectrometry with Penning traps: Theoretical foundations. *International Journal of Mass Spectrometry*, 264(2-3):122–145, July 2007.

[82] G. Bollen, S. Becker, H. Kluge, M. König, R.B. Moore, T. Ottob, H. Raimbault-Hartmann, G. Savard, L. Schweikhard, and H. Stolzenberg. ISOLTRAP : a tandem Penning trap system for accurate on-line mass determination of short-lived isotopes. *Nuclear Instruments and Methods in Physics Research A*, 368:675–697, 1996.

[83] G. Gräff, H. Kalinowsky, and J. Traut. A direct determination of the proton electron mass ratio. *Zeitschrift für Physik A Hadrons and Nuclei*, 297:35–39, 1980.

[84] M. König, G. Bollen, H.-J. Kluge, T. Otto, and J. Szerypo. Quadrupole excitation of stored ion motion at the true cyclotron frequency. *International Journal of Mass Spectrometry and Ion Processes*, 142(1-2):95–116, March 1995.

[85] Guy Savard. A new cooling technique for heavy ions in a Penning trap. *Physics Letters A*, 158(5):247–252, September 1991.

[86] M. Mukherjee, D. Beck, K. Blaum, G. Bollen, J. Dilling, S. George, F. Herfurth, A. Herlert, A. Kellerbauer, H. J. Kluge, S. Schwarz, L. Schweikhard, and C. Yazidjian. ISOLTRAP: An on-line Penning trap for mass spectrometry on short-lived nuclides. *The European Physical Journal A*, 35(1):1–29, February 2008.

[87] S. Guan and A.G. Marshall. Stored waveform inverse Fourier transform (SWIFT) ion excitation in trapped-ion mass spectometry: theory and applications. *International Journal of Mass Spectrometry and Ion Processes*, 157/158:5–37, 1996.

[88] S. George, S. Baruah, B. Blank, K. Blaum, M. Breitenfeldt, U. Hager, F. Herfurth, A. Herlert, A. Kellerbauer, H.-J. Kluge, M. Kretzschmar, D. Lunney, R. Savreux, S. Schwarz, L. Schweikhard, and C. Yazidjian. Ramsey Method of Separated Oscillatory Fields for High-Precision Penning Trap Mass Spectrometry. *Physical Review Letters*, 98(16):162501, April 2007.

[89] S. Ettenauer, M.C. Simon, A.T. Gallant, T. Brunner, U. Chowdhury, V.V. Simon, M. Brodeur, A. Chaudhuri, E. Mané, C. Andreoiu, G. Audi, J.R. Crespo López-Urrutia, P. Delheij, G. Gwinner, A. Lapierre, D. Lunney, M. R. Pearson, R. Ringle, J. Ullrich, and J. Dilling. First Use of High Charge States for Mass Measurements of Short-Lived Nuclides in a Penning Trap. *Physical Review Letters*, 107(27):272501, December 2011.

[90] Stephan Ettenauer. *First Mass Measurements of Highly Charged, Short-lived Nuclides in a Penning Trap and the Mass of ^{74}Rb.* PhD thesis, The University of British Columbia, Vancouver, Canada, January 2012.

[91] S. Eliseev, C. Roux, K. Blaum, M. Block, C. Droese, F. Herfurth, M. Kretzschmar, M. Krivoruchenko, E. Minaya Ramirez, Yu. Novikov, L. Schweikhard, V. Shabaev, F. Šimkovic, I. Tupitsyn, K. Zuber, and N. Zubova. Octupolar-excitation Penning-trap mass spectrometry for

Q-value measurement of double-electron capture in ^{164}Er. *Physical Review Letters*, 107(15):1–5, October 2011.

[92] R. Ringle, P. Schury, T. Sun, G. Bollen, D. Davies, J. Huikari, E. Kwan, D.J. Morrissey, A. Prinke, J. Savory, S. Schwarz, and C. Sumithrarachchi. Precision mass measurements with LEBIT at MSU. *International Journal of Mass Spectrometry*, 251(2-3):300–306, April 2006.

[93] S. Schwarz, G. Bollen, D. Lawton, P. Lofy, D.J. Morrissey, J. Ottarson, R. Ringle, P. Schury, T. Sun, V. Varentsov, and L. Weissman. The low-energy-beam and ion-trap facility at NSCL/MSU. *Nuclear Instruments and Methods in Physics Research Section B: Beam Interactions with Materials and Atoms*, 204:507–511, May 2003.

[94] R. Ringle, G. Bollen, A. Prinke, J. Savory, P. Schury, S. Schwarz, and T. Sun. The LEBIT 9.4T Penning trap mass spectrometer. *Nuclear Instruments and Methods in Physics Research Section A: Accelerators, Spectrometers, Detectors and Associated Equipment*, 604(3):536–547, June 2009.

[95] A.T. Gallant, M. Brodeur, T. Brunner, U. Chowdhury, S. Ettenauer, V.V. Simon, E. Mané, M.C. Simon, C. Andreoiu, P. Delheij, G. Gwinner, M.R. Pearson, R. Ringle, and J. Dilling. Highly charged ions in Penning traps, a new tool for resolving low lying isomeric states. *Physical Review C*, 85(4):044311, 2012.

[96] J. Dilling, R. Baartman, P. Bricault, M. Brodeur, L. Blomeley, F Buchinger, J. Crawford, J.R. Crespo López-Urrutia, P. Delheij, M. Froese, G.P. Gwinner, Z. Ke, J.K.P. Lee, R.B. Moore, V. Ryjkov, G. Sikler, M. Smith, J. Ullrich, and J. Vaz. Mass measurements on highly charged radioactive ions, a new approach to high precision with TITAN. *International Journal of Mass Spectrometry*, 251(2-3):198–203, April 2006.

[97] M. Dombsky, D. Bishop, P. Bricault, D. Dale, A. Hurst, K. Jayamanna, R. Keitel, M. Olivo, P. Schmor, and G. Stanford. Commissioning and initial operation of a radioactive beam ion source at ISAC. *Review of Scientific Instruments*, 71(2):978–980, 2000.

[98] B.R. Fulton. Present and Future RIB Facilities. *Journal of Physics: Conference Series*, 312(5):052001, September 2011.

[99] G. D. Alton. Ion sources for accelerators in materials research. *Nuclear Instruments and Methods in Physics Research Section B: Beam Interactions with Materials and Atoms*, 73(2):221–288, 1993.

[100] G. D. Alton. Sources of low-charge-state positive-ion beams. *Methods in Experimental Physics*, pages 69–168, 1995.

[101] A.F. Holleman and E. Wiberg. *Lehrbuch der Anorganischen Chemie*. deGruyter, Berlin, NewYork, 101. edition, 1995.

[102] Maxime Brodeur. *First direct mass measurement of the two and four neutron halos ^{6}He and ^{8}He using the TITAN Penning trap mass spectrometer*. Phd thesis, University of British Columbia, April 2010.

[103] Marik Dombsky. Yield Database, 2012.

[104] Erich Kugler. The ISOLDE facility. *Hyperfine Interactions*, 129:23–42, 2000.

[105] T. Brunner, M.J. Smith, M. Brodeur, S. Ettenauer, A.T. Gallant, V.V. Simon, A. Chaudhuri, A. Lapierre, E. Mané, R. Ringle, M.C. Simon, J.A. Vaz, P. Delheij, M. Good, M.R. Pearson, and J. Dilling. TITAN's digital RFQ ion beam cooler and buncher, operation and performance. *Nuclear Instruments and Methods in Physics Research Section A: Accelerators, Spectrometers, Detectors and Associated Equipment*, 676:32–43, June 2012.

[106] A. Lapierre, M. Brodeur, T. Brunner, S. Ettenauer, A.T. Gallant, V.V. Simon, M. Good, M.W. Froese, J.R. Crespo López-Urrutia, P. Delheij, S. Epp, R. Ringle, S. Schwarz, J. Ullrich, and J. Dilling. The TITAN EBIT charge breeder for mass measurements on highly charged short-lived isotopesFirst online operation. *Nuclear Instruments and Methods in Physics Research Section A: Accelerators, Spectrometers, Detectors and Associated Equipment*, 624(1):54–64, December 2010.

[107] M. Brodeur, T. Brunner, C. Champagne, S. Ettenauer, M. Smith, A. Lapierre, R. Ringle, V.L. Ryjkov, G. Audi, P. Delheij, D. Lunney, and J. Dilling. New mass measurement of ^{6}Li and ppb-level systematic studies of the Penning trap mass spectrometer TITAN. *Physical Review C*, 80(4):044318, October 2009.

[108] A. Kellerbauer, T. Kim, R.B. Moore, and P. Varfalvy. Buffer gas cooling of ion beams. *Nuclear Instruments and Methods in Physics*

Research Section A: Accelerators, Spectrometers, Detectors and Associated Equipment, 469(2):276–285, August 2001.

[109] F. Herfurth, J. Dilling, A. Kellerbauer, G. Bollen, S. Henry, H.-J. Kluge, E. Lamour, D. Lunney, R.B. Moore, C. Scheidenberger, S. Schwarz, G. Sikler, and J. Szerypo. A linear radiofrequency ion trap for accumulation, bunching, and emittance improvement of radioactive ion beams. *Nuclear Instruments and Methods in Physics Research Section A: Accelerators, Spectrometers, Detectors and Associated Equipment*, 469(2):254–275, August 2001.

[110] A. Nieminen, P. Campbell, J. Billowes, D. Forest, J. Griffith, J. Huikari, A. Jokinen, I. Moore, R. Moore, G. Tungate, and J. Äystö. On-Line Ion Cooling and Bunching for Collinear Laser Spectroscopy. *Physical Review Letters*, 88(9):2–5, February 2002.

[111] E. Mané, J. Billowes, K. Blaum, P. Campbell, B. Cheal, P. Delahaye, K.T. Flanagan, D.H. Forest, H. Franberg, C. Geppert, T. Giles, A. Jokinen, M. Kowalska, R. Neugart, G. Neyens, W. Nörtershäuser, I. Podadera, G. Tungate, P. Vingerhoets, and D.T. Yordanov. An ion cooler-buncher for high-sensitivity collinear laser spectroscopy at ISOLDE. *The European Physical Journal A*, 42(3):503–507, June 2009.

[112] E. Mané, A. Voss, J. Behr, J. Billowes, T. Brunner, F. Buchinger, J. Crawford, J. Dilling, S. Ettenauer, C. Levy, O. Shelbaya, and M. Pearson. First Experimental Determination of the Charge Radius of ^{74}Rb and Its Application in Tests of the Unitarity of the Cabibbo-Kobayashi-Maskawa Matrix. *Physical Review Letters*, 107(21):2–5, November 2011.

[113] M. Smith, L. Blomeley, P. Delheij, and J. Dilling. First tests of the TITAN digital RFQ beam cooler and buncher. *Hyperfine Interactions*, 173(1-3):171–180, June 2007.

[114] G. Sikler, J.R. Crespo López-Urrutia, J. Dilling, S. Epp, C.J. Osborne, and J. Ullrich. A high-current EBIT for charge-breeding of radionuclides for the TITAN spectrometer. *The European Physical Journal A*, 25(S1):63–64, May 2005.

[115] Michael W. Froese. *The TITAN Electron Beam Ion Trap: Assembly, Characterization, and First Tests*. PhD thesis, 2006.

[116] T. Brunner, A.R. Mueller, K. OSullivan, M.C. Simon, M. Kossick, S. Ettenauer, A.T. Gallant, V.V. Simon, E. Mané, D. Bishop, M. Good,

G. Gratta, and J. Dilling. A large Bradbury Nielsen ion gate with flexible wire spacing based on photo-etched stainless steel grids and its characterization applying symmetric and asymmetric potentials. *International Journal of Mass Spectrometry*, 309:97–103, September 2011.

[117] R. Ringle, G. Bollen, A. Prinke, J. Savory, P. Schury, S. Schwarz, and T. Sun. A "Lorentz" steerer for ion injection into a Penning trap. *International Journal of Mass Spectrometry*, 263(1):38–44, May 2007.

[118] K. Langanke and G. Martinez-Pinedo. Nuclear weak-interaction processes in stars. *Reviews of Modern Physics*, 75(3):819–862, June 2003.

[119] P. Hosmer, H. Schatz, A. Aprahamian, O. Arndt, R.R.C. Clement, A. Estrade, K. Farouqi, K.-L. Kratz, S.N. Liddick, A.F. Lisetskiy, P.F. Mantica, P. Möller, W.F. Mueller, F. Montes, A.C. Morton, M. Ouellette, E. Pellegrini, J. Pereira, B. Pfeiffer, P. Reeder, P. Santi, M. Steiner, A. Stolz, B.E. Tomlin, W.B. Walters, and A. Wöhr. Half-lives and branchings for β-delayed neutron emission for neutron-rich CoCu isotopes in the r-process. *Physical Review C*, 82(2):025806, August 2010.

[120] J.M. Pomeroy and H. Grube. Highly charged ion (HCI) modified tunnel junctions. *AIP Conference Proceedings Series*, 1099:520–523, 2009.

[121] A. Valassi. Combining correlated measurements of several different physical quantities. *Nuclear Instruments and Methods in Physics Research Section A: Accelerators, Spectrometers, Detectors and Associated Equipment*, 500(1-3):391–405, March 2003.

[122] B.J. Mount, M. Redshaw, and E.G. Myers. Atomic masses of ^{6}Li,^{23}Na,^{39,41}K,^{85,87}Rb, and ^{133}Cs. *Physical Review A*, 82(4):042513, October 2010.

[123] G.C. Rodrigues, P. Indelicato, J.P. Santos, P. Patté, and F. Parente. Systematic calculation of total atomic energies of ground state configurations. *Atomic Data and Nuclear Data Tables*, 86(2):117–233, March 2004.

[124] Paul Indelicato. Uncertainties on electron binding energies. *Private communication*, 2011.

[125] A. Kellerbauer, K. Blaum, G. Bollen, F. Herfurth, H.-J. Kluge, M. Kuckein, E. Sauvan, C. Scheidenberger, and L. Schweikhard. From direct to absolute mass measurements: A study of the accuracy of

ISOLTRAP. *The European Physical Journal D - Atomic, Molecular and Optical Physics*, 22(1):53–64, January 2003.

[126] M. Brodeur, T. Brunner, C. Champagne, S. Ettenauer, M.J. Smith, A. Lapierre, R. Ringle, V.L. Ryjkov, S. Bacca, P. Delheij, G.W.F. Drake, D. Lunney, A. Schwenk, and J. Dilling. First Direct Mass Measurement of the Two-Neutron Halo Nucleus ^{6}He and Improved Mass for the Four-Neutron Halo ^{8}He. *Physical Review Letters*, 108(5):052504, January 2012.

[127] R.S. Van Dyck, F.L. Moore, D.L. Farnham, and P.B. Schwinberg. Number dependency in the compensated Penning trap. *Physical Review A*, 40(11):6308–6313, December 1989.

[128] J.V. Porto. Series solution for the image charge fields in arbitrary cylindrically symmetric Penning traps. *Physical Review A*, 64(2):1–7, June 2001.

[129] H. Raimbault-Hartmann, G. Audi, D. Beck, G. Bollen, M. De Saint Simon, H.-J. Kluge, M. König, R.B. Moore, S. Schwarz, G. Savard, and J. Szerypo. High-accuracy mass determination of neutron-rich rubidium and strontium isotopes. *Nuclear Physics A*, 706(1-2):3–14, July 2002.

[130] R. Decker, K.D. Wünsch, H. Wollnik, E. Koglin, G. Siegert, and G. Jung. Präzise Qβ-Wert-Messungen mit einem Intrinsic-Germanium Detektor an leichten, neutronenreichen Spaltprodukten. *Zeitschrift für Physik A Hadrons and Nuclei*, 294(1):35–49, 1980.

[131] F. Blönnigen, G. Bewersdorf, C. Geisse, W. Lippert, B. Pfeiffer, U. Stöhlker, and H Wollnik. In *Proceedings of the 7th International Conference Atomic Masses and Fundamental Constants AMCO-7*, page 134, Darmstadt, 1984.

[132] M. Graefenstedt, U. Keyser, F. Münnich, and F. Schreiber. In *Proceedings of the 5th International Conference Nuclei far fram Stability NUFAST-5*, page 30, Rosseau, 1987. AIP Conference Proceedings 164.

[133] M. Przewloka, A. Przewloka, P. Wächter, and H. Wollnik. Measurements of β-endpoint-energies using a magnetic electron separator. *Zeitschrift für Physik A Hadrons and Nuclei*, 342(1):23–26, 1992.

[134] G. Audi and M. Wang. Atomic Mass Evaluation 2011. *Private communication*, 2011.

[135] G. Audi, A. Coc, M. Epherre, G. Le Scornet, C. Thibault, and F. Touchard. Mass-Spectrometric Measurements of Exotic Rb, Cs and Fr Isotopes. *Nuclear Physics*, 449:491–518, 1986.

[136] National Nuclear Data Center. National Nuclear Data Center, 2012.

[137] M. Groß, P. Jürgens, S. Kluge, M. Mehrtens, S. Müller, F. Münnich, and J. Wulff. No Title. In *Proceedings of the 9th International Conference Atomic Masses and Fundamental Constants AMCO-9*, page 77, Bernkastel, 1992.

[138] R. Iafigliola, H. Dautet, S.W. Xu, J.K.P. Lee, R. Chrien, R. Gill, and M. Shmid. In *Proceedings of the 7th International Conference Atomic Masses and Fundamental Constants AMCO-7*, page 141, Darmstadt, 1984.

[139] P. Delahaye, G. Audi, K. Blaum, F. Carrel, S. George, F. Herfurth, A. Herlert, A. Kellerbauer, H.-J. Kluge, D. Lunney, L. Schweikhard, and C. Yazidjian. High-accuracy mass measurements of neutron-rich Kr isotopes. *Physical Review C*, 74(3):034331, September 2006.

[140] C. Thibault, F. Touchard, S. Büttgenbach, R. Klapisch, M. de Saint Simon, H.T. Duong, P. Jacquinot, S. Liberman, P. Pillet, J. Pinard, and J.L. Vialle. Hyperfine structure and isotope shift of the D_2 line of $^{76-98}$Rb and some of their isomers. *Physical Review A*, 23(6):2720–2729, 1981.

[141] F. Buchinger, E.B. Ramsay, E. Arnold, W. Neu, R. Neugart, K. Wendt, R.E. Silverans, P. Lievens, L. Vermeeren, D. Berdichevsky, R. Fleming, D.W. Sprung, and G. Ulm. Erratum: Systematics of nuclear ground state properties in $^{78-100}$Sr by laser spectroscopy. *Physical Review C*, 42(6):2754, December 1990.

[142] C. Travaglio, R. Gallino, E. Arnone, J. Cowan, F. Jordan, and C. Sneden. Galactic Evolution of Sr , Y , and Zr : A Multiplicity of Nucleosynthetic Processes. *The Astrophysical Journal*, 601:864–884, 2004.

[143] R.E. Marrs. Self-cooling of highly charged ions during extraction from electron beam ion sources and traps. *Nuclear Instruments and Methods in Physics Research Section B: Beam Interactions with Materials and Atoms*, 149(1-2):182–194, January 1999.

[144] N. Oshima, M. Niigaki, M. Inoue, T. M. Kojima, A. Mohri, Y. Kanai, Y. Nakai, K. Komaki, and Y. Yamazaki. Project to produce cold highly

charged ions using positron and electron cooling techniques. *Journal of Physics: Conference Series*, 2:127–133, January 2004.

[145] S. Ettenauer, M.C. Simon, V.V. Simon, and A.T. Gallant. Injection of a 'full' EBIT pulse into the MPET. *Private communication.*

[146] G. Savard, R.C. Barber, C. Boudreau, F. Buchinger, J. Caggiano, J. Clark, J.E. Crawford, H. Fukutani, S. Gulick, J.C. Hardy, A. Heinz, J.K.P. Lee, R.B. Moore, K.S. Sharma, J. Schwartz, D. Seweryniak, G.D. Sprouse, and J. Vaz. The Canadian Penning Trap Spectrometer at Argonne. *Hyperfine Interactions*, 132:223–230, 2001.

[147] H.G. Dehmelt and F.L. Walls. "Bolometric" Technique for the rf Spectroscopy of Stored Ions. *Physical Review Letters*, 21(3):127–131, 1968.

[148] D.J. Wineland and H.G. Dehmelt. Principles of the stored ion calorimeter. *Journal of Applied Physics*, 46(2):919–930, 1975.

[149] W.M. Itano, J.C. Bergquist, J.J. Bollinger, and D.J. Wineland. Cooling Methods in Ion Traps. *Physica Scripta*, T59:106–120, 1995.

[150] S.L. Rolston and G. Gabrielse. Cooling Antiprotons in an Ion Trap. *Hyperfine Interactions*, 44:233–246, 1988.

[151] H. Häffner, T. Beier, S. Djekić, N. Hermanspahn, H.-J. Kluge, W. Quint, S. Stahl, J. Verdú, T. Valenzuela, and G. Werth. Double Penning trap technique for precise g factor determinations in highly charged ions. *The European Physical Journal D*, 22(2):163–182, February 2003.

[152] W. Petrich, M.H. Anderson, J.R. Ensher, and E.A. Cornell. Stable, Tightly Confining Magnetic Trap for Evaporative Cooling of Neutral Atoms. *Physical Review Letters*, 74(17):3352–3355, 1995.

[153] M. Hobein, A. Solders, M. Suhonen, Y. Liu, and R. Schuch. Evaporative Cooling and Coherent Axial Oscillations of Highly Charged Ions in a Penning Trap. *Physical Review Letters*, 106:013002, January 2011.

[154] F. Ames, G. Bollen, P. Delahaye, O. Forstner, G. Huber, O. Kester, K. Reisinger, and P. Schmidt. Cooling of radioactive ions with the Penning trap REXTRAP. *Nuclear Instruments and Methods in Physics Research Section A: Accelerators, Spectrometers, Detectors and Associated Equipment*, 538(1-3):17–32, February 2005.

[155] R.G. Greaves and C.M. Surko. Inward transport and compression of a positron plasma by a rotating electric field. *Physical Review Letters*, 85(9):1883–1886, August 2000.

[156] N. Oshima, T.M. Kojima, M. Niigaki, A. Mohri, K. Komaki, Y. Iwai, and Y. Yamazaki. Development of a cold HCI source for ultra-slow collisions. *Nuclear Instruments and Methods in Physics Research Section B: Beam Interactions with Materials and Atoms*, 205:178–182, May 2003.

[157] M. Steck, K. Beckert, H. Eickhoff, B. Franzke, F. Nolden, H. Reich, B. Schlitt, and T. Winkler. Anomalous Temperature Reduction of Electron-Cooled Heavy Ion Beams in the Storage Ring ESR. *Physical review letters*, 77(18):3803–3806, October 1996.

[158] G. Gabrielse, X. Fei, L.A. Orozco, R.L. Tjoelker, J. Haas, H. Kalinowsky, T.A. Trainor, and W. Kells. Cooling and slowing of trapped antiprotons below 100 meV. *Physical Review Letters*, 63(13):1360–1363, September 1989.

[159] G. Gabrielse, N.S. Bowden, P. Oxley, A. Speck, C.H. Storry, J.N. Tan, M. Wessels, D. Grzonka, W. Oelert, G. Schepers, T. Sefzick, J. Walz, H. Pittner, T.W. Hänsch, and E.A. Hessels. Background-Free Observation of Cold Antihydrogen with Field-Ionization Analysis of Its States. *Physical Review Letters*, 89(21):2–5, October 2002.

[160] M. Amoretti *et al.* The ATHENA antihydrogen apparatus. *Nuclear Instruments and Methods in Physics Research Section A: Accelerators, Spectrometers, Detectors and Associated Equipment*, 518(3):679–711, February 2004.

[161] M. Amoretti *et al.* Production and detection of cold antihydrogen atoms. *Nature (London)*, 419(6906):456–459, October 2002.

[162] T. Beier, L. Dahl, H.-J. Kluge, C. Kozhuharov, and W. Quint. Trapping ions of hydrogen-like uranium: The HITRAP project at GSI. *Nuclear Instruments and Methods in Physics Research Section B: Beam Interactions with Materials and Atoms*, 235(1-4):473–478, July 2005.

[163] H.-J. Kluge, T. Beier, K. Blaum, L. Dahl, S. Eliseev, F. Herfurth, B. Hofmann, O. Kester, S. Koszudowski, C. Kozhuharov, G. Maero, W. Nörtershäuser, J. Pfister, W. Quint, U. Ratzinger, A. Schempp, R. Schuch, Th. Stöhlker, R.C. Thompson, M. Vogel, G. Vorobjev,

D.F.A. Winters, and G. Werth. HITRAP: A Facility at GSI for Highly Charged Ions. *Advances in Quantum Chemistry*, 53:83–98, 2008.

[164] Günter Zwicknagel. Electron Cooling of Highly Charged Ions in Penning Traps. *AIP Conference Proceedings*, 862:281–291, 2006.

[165] Zunjian Ke. *A cooler ion trap for the TITAN on-line trapping facility at TRIUMF*. PhD thesis, University of Manitoba, Winnipeg, Canada, 2008.

[166] Z. Ke, W. Shi, G. Gwinner, K. Sharma, S. Toews, J. Dilling, and V.L. Ryjkov. A cooler ion trap for the TITAN on-line trapping facility at TRIUMF. *Hyperfine Interactions*, 173(1-3):103–111, June 2006.

[167] V.V. Simon, U. Chowdhury, P. Delheij, J. Dilling, B. Eberhardt, and G. Gwinner. A cooler Penning trap for the TITAN on-line trapping facility. *Journal of Physics: Conference Series*, 312(5):052024, September 2011.

[168] V.V. Simon, P. Delheij, J. Dilling, Z. Ke, W. Shi, and G. Gwinner. Cooling of short-lived, radioactive, highly charged ions with the TITAN cooler Penning trap. *Hyperfine Interactions*, 199(1-3):151–159, May 2011.

[169] X. Fei and W.M. Snow. Cylindrical Penning traps with dynamic orthogonalized anharmonicity compensation for precision experiments. *Nuclear Instruments and Methods in Physics Research Section A: Accelerators, Spectrometers, Detectors and Associated Equipment*, 425(3):431–440, 1999.

[170] Giancarlo Maero. *Cooling of highly charged ions in a Penning trap for HITRAP*. PhD thesis, University of Heidelberg, 2008.

[171] G. Testera. The role of the patch effect electric fields in the Penning trap method of measuring the gravitational force on antiprotons. *Hyperfine Interactions*, 109(1-4):333–343, 1997.

[172] Benjamin Eberhardt. The TITAN cooler Penning trap for short-lived highly charged ions: investigations for nested trap applications and fast electrode switching. *Diplomarbeit, Johannes Gutenberg Universität, Mainz, Germany*, 2011.

[173] C.A. Spindt and C. Holland. Field-Emitter Arrays for Research. *Vacuum Microelectronics Program, SRI International*, 2009.

[174] Colutron Research Corporation. Colutron Ion Source, 2011.

[175] M. Menzinger and L. Wahlin. High Intensity, Low Energy Spread Ion Source for Chemical Accelerators. *Review of Scientific Instruments*, 40(1):102–105, 1969.

[176] Cryomagnetics Inc. http://www.cryomagnetics.com/, 2012.

[177] Cryomagnetics Inc. Operating Instruction Manual for Superconducting Magnet System. Technical report, 2008.

[178] A. Müller and E. Salzborn. Scaling of cross sections for multiple electron transfer to highly charged ions colliding with atoms and molecules. *Physics Letters A*, 62:391, 1977.

[179] C. Benvenuti, P. Chiggiato, P. Costa Pinto, A. Escudeiro Santana, T. Hedley, A. Mongelluzzo, V. Ruzinov, and I. Wevers. Vacuum properties of TiZrV non-evaporable getter films. *Vacuum*, 60(1-2):57–65, 2001.

[180] Methodisch-Diagnostisches Zentrum Werkstoffprüfung e. V. X-ray photoelectron spectroscopy (XPS) report. Technical report, Methodisch-Diagnostisches Zentrum Werkstoffprüfung e. V., Magdeburg, Germany, 2010.

[181] M. Hahn and R. Kersevan. Status of NEG Coating at ESRF. In *Particle Accelerator Conference*, number December 2004, pages 422–424, Knoxville, USA, 2005.

[182] T. Mohamed, H. Imao, N. Oshima, A. Mohri, and Y. Yamazaki. Fast electron accumulation and its mechanism in a harmonic trap under ultrahigh vacuum conditions. *Physics of Plasmas*, 18(3):032507, 2011.

[183] V. V. Simon, M. Brodeur, and J. Dilling. S1373: Precise mass measurements of Sr and Rb isotopes in the vicinity of the r-process path. *TRIUMF Sub-Atomic Physics EEC New Research Proposal*, 2012.

[184] V.L. Ryjkov, L. Blomeley, M. Brodeur, P. Grothkopp, M. Smith, P. Bricault, F. Buchinger, J. Crawford, G. Gwinner, J. Lee, J. Vaz, G. Werth, J. Dilling, and TITAN collaboration. TITAN project status report and a proposal for a new cooling method of highly charged ions. *The European Physical Journal A*, 25(S1):53–56, July 2005.

[185] TRIUMF. TRIUMF's Archive, Design Office. *Internal Documentation Technical Drawings*, 2012.

[186] TRIUMF. TRIUMF's Archive, EDEV. *Internal Electronics Developements*, 2012.

Acknowledgments

In general, for Penning-trap mass spectrometry one ion is trapped at a time. Nevertheless, the preparation to achieve such an measurement requires many more than one unit of man-power.

First of all, I would like to thank my every-day supervisor Jens Dilling. He drew me into joining the TITAN group and I am very grateful for his continuous support and trust in me and in my work. His endless motivation, advice, and the transfered responsibilities allowed me to blossom and widen my horizon. I am truly thankful to Jens for the opportunities to present TITAN on worldwide conferences and to encourage me in contacting leading scientists in the various fields of my work.

I am very grateful to my first supervisor Klaus Blaum, who has taken me on as his doctoral student. Despite the large geographical distance he provided me with support and guidance whenever needed. Our communications and discussions took place all around the clock, and it allowed me to formulate a scientific case in the evening and await the reply first thing in the morning. The scientific exchange was very beneficial and allowed me to broaden my knowledge. Thank you as well for your support and encouragement to apply for scholarships.

The project around the Cooler Penning Trap could not have been pursued without Gerald Gwinner, the project leader, and the funding that he received for our project. Thank you for all your support, the Skype calls, meetings, and the fruitful discussions.

Thank you to José Crespo for gratefully agreeing to be the second referee as well as Uwe Oelfke and Tilman Plehn for completing the examination committee.

Thank you to all TITAN collaborators and especially my colleagues (in alphabetical order) Jeff Bale, Maxime Brodeur, Thomas Brunner, Ankur Chaudhuri, Usman Chowdhury, Paul Delheij, Stephan Ettenauer, Aaron Gallant, Alexander Grossheim, Ania Kwiatkowski, Annika Lennarz, Tegan

Macdonald, Ernesto Mané, Matt Pearson, Ryan Ringle, Brad Schultz, and Martin Simon for providing a friendly and stimulating work atmosphere. All the many beamtimes that we experienced together, which included a combination of interesting, funny, and stressful situations, will be vivid for a long time. Our ambitious, little CPET group, consisting of Brad Schultz (thanks for all your reading, comments, and support) and Usman Chowdhury, was completed by two undergraduate students, Benjamin Eberhardt and Fuluny Jang, whom I enjoyed supervising. The technical work would not have been possible without the great work and help from Mel Good, the TITAN technologist and many friendly helpers in TRIUMF's technical staff.

I am very thankful to Hendrik Schatz, my astrophysics guru, in running the r-process model network calculations. The thesis benefited greatly from his enthusiasm and all our nuclear astrophysics discussions.

On the nuclear structure side, I am very thankful to David Lunney, who draw me into the dialogs of mass models and their description of the mass surface and its cartography. I would like to express my gratitude to Georges Audi and David Lunney for their hospitality during my visit to Orsay for the mass evaluation of the presented results.

Thank you to Klaus Blaum, Jens Dilling, Alexander Grossheim, Gerald Gwinner, Ania Kwiatkowski, Annika Lennarz, Brad Schultz, and Martin Simon for their thorough reading as well as their input and comments to (parts of) this thesis.

I am grateful for the scholarships from the Studienstiftung des deutschen Volkes (Promotionsstipendium) and the German Academic Exchange Service (DAAD, Doktorandenstipendium) for their financial and travel support.

I had an incredible time with TITAN and in Vancouver and appreciate all my colleagues, and all my friends here and back home in Germany for supporting me during my studies.

Bei meinen Eltern möchte ich mich für die finanzielle und ideelle Unterstützung während des Studiums bedanken. Auf den starken familiären Zusammenhalt und ihre Begeisterung für meine Entscheidungen kann ich mich immer verlassen. Mein Bruder war immer für mich da und auch für Späße zu haben. Bei meinem Freund Michael bedanke ich mich sehr für seine Geduld and loving support, wenn am Institut mal wieder Einiges anstand und die Zeit knapp bemessen war. Ihm wie auch meiner Familie danke ich für das Zusprechen von Mut, wenn mal wieder etwas nicht so wollte, wie es sollte.